5-2014

Impact of Beaver Ponds on Stream Temperature and on Solar Radiation Penetration in Water

Camilla J. Snow
Utah State University

Recommended Citation

Snow, Camilla J., "Impact of Beaver Ponds on Stream Temperature and on Solar Radiation Penetration in Water" (2014). *All Graduate Theses and Dissertations*. 3858.
https://digitalcommons.usu.edu/etd/3858

IMPACT OF BEAVER PONDS ON STREAM TEMPERATURE AND ON SOLAR RADIATION PENETRATION IN WATER

by

Camilla J. Snow

A thesis submitted in partial fulfillment of the
requirements for the degree

of

MASTER OF SCIENCE

in

Civil and Environmental Engineering

Approved:

Dr. Bethany T. Neilson Environmental Engineering Major Professor	Dr. Randal S. Martin Environmental Engineering Committee Member
Dr. Bruce Bugbee Environmental Physiology Committee Member	Dr. Mark McLellan Vice President for Research and Dean of the School of Graduate Studies

UTAH STATE UNIVERSITY
Logan, Utah

2014

ABSTRACT

Effect of Beaver Ponds on Stream Temperature and on Solar Radiation Penetration in Water

by

Camilla J. Snow, Master of Science

Utah State University, 2014

Major Professor: Bethany T. Neilson
Department: Civil and Environmental Engineering

The physical alterations to a stream caused by beaver dams create a thermally heterogeneous environment that promotes diverse aquatic communities and provides thermal refugia. The spatial distribution of temperature varies widely and the underlying energy balance is poorly understood. Here we develop a process-based temperature model for a beaver pond in Northern Utah. The calibrated model identified the dominant heat fluxes for each zone and captured the spatial and temporal variability in water temperatures. This model provides insight to the key processes and characteristics driving the thermal heterogeneity within beaver ponds.

Shortwave radiation was found to be one of these key processes, because it is often the most influential heat flux within stream energy budgets. There is a need to develop methods for determining the fate of broad-spectrum shortwave radiation in the water column to ensure an accurate representation in temperature models. Because water has non-uniform spectral absorption, it is necessary to use black-body pyranometers with a flat spectral response. To use black body pyranometers with hemispherical glass domes designed for use in air, there is a need to calibrate them for use in water. Studies were conducted to determine immersion corrections and the cosine response of such pyranometers underwater. The immersion corrections were found to differ between electric light sources, suggesting that these corrections are dependent on the spectrum of the light. The cosine response of the sensor underwater was also found to be inaccurate, suggesting that similarly inaccurate readings would result for *in situ* measurements when sunlight is reaching the sensor at various angles. We propose a need for further investigation into methods that can be used to correct pyranometers in order to measure the fate of shortwave radiation in the natural water bodies. Combined, this research provides methods and suggests additional research opportunities for more accurately quantifying and predicting stream temperatures in areas impacted by beaver colonization.

(134 pages)

PUBLIC ABSTRACT

Effect of Beaver Ponds on Stream Temperature and on Solar Radiation Penetration in Water

Camilla J. Snow

Beaver dams alter streams characteristics in a way that promotes the diversity of aquatic species and provides a wide distribution of temperatures within beaver ponds. In order to quantify the spatial distribution of these temperatures, a process-based temperature model was developed for a beaver pond in Northern Utah. This model provided insight into the processes and characteristics that are driving these temperatures. Solar radiation is one of these processes that is often the primary driver of stream temperature. There is a need to develop methods to measure the fate of solar radiation within the water to better represent solar radiation within stream temperature models. Black-body pyranometers are instruments that measure solar radiation in air, but require corrections for use underwater. Studies were conducted investigating methods for correcting these instruments. Based on the results of these studies it is suggested that these corrections are dependent on the spectrum of the light source and that the instrument needs further corrections when the light source is measured from different angles; therefore there is a need for further investigation into pyranometer corrections in order to measure the fate of solar radiation in natural water bodies. Combined, this research provides methods and suggests additional research opportunities for more accurately quantifying and predicting stream temperatures for waters impacted by beaver.

ACKNOWLEDGMENTS

I would like to thank my advisor, Dr. Bethany Neilson, for all of her guidance, help, understanding, feedback, patience, etc. while I have worked with her over the past six years. I truly had the best advisor in the world and I honestly believe that my academic success is due in large part to her starting me as an undergraduate freshman and working with me all the way through graduate school. I would also like to thank my committee members, Dr. Randy Martin and Dr. Bruce Bugbee, for all of their insightful feedback. I feel I truly learned so much from each of them in their contribution to my thesis research as well as in the courses I was able to take from each of them. Furthermore, I would like to thank Dr. Milada Majerova for her help in my beaver pond research. I was very lucky that our work on beaver ponds coincided and that I was able to learn much from her in the field as well as in the office.

I would like to give special thanks to Noah Schmadel for his guidance, support, and uplifting attitude throughout my entire collegiate career. I can attribute nearly all I know about fieldwork and a lot of what I have learned about environmental engineering to his teaching and example. Thank you also to Florie Consolati, Tyler King, Trinity Stout, Karthik Kumarasamy, Madeline Merck, and Andrew Hobson for all of their support as well as assistance with data collection and modeling. I would like to further thank the following sources of financial support that made attending graduate school possible for me, which include the Utah Water Research Laboratory, the American Association of University Women, the Seely-Hinckley Scholarship Fund, the NSPE-PEC George B. Hightower, P.E. Fellowship Fund, and the American Water Works Association.

A special and sincere thank you to my wonderful husband, Jason, who sacrificed so much of his own collegiate career so that I could advance in mine and also to our wonderful son, Austin, whose first two years have brought me so much joy during the entirety of my graduate school career. Finally, I would like to thank my mom who raised me and worked so hard to get me to and through college and for all of my many other wonderful family members who have helped us tremendously, particularly when we were in times of need. They are the ultimate reason I am where I am today.

Camilla J. Snow

CONTENTS

Page

CHAPTER

LIST OF TABLES

LIST OF FIGURES

CHAPTER 1

INTRODUCTION

Introducing beaver to streams may be a sustainable option for stream restoration [*Burchsted et al.*, 2010]. Beaver cost less than human-engineered methods [*Barrett*, 1999] and have been shown to benefit stream ecosystems [*Shields et al.*, 1995; *Barrett*, 1999; *Albert & Trimble*, 2000; *Pollock et al.*, 2004; *Burchsted et al.*, 2010; *Ciechanowski et al*., 2011; *Billman et al.*, 2013]. Beaver activity has also been shown to change many of the physical characteristics within and surrounding streams [*Gard*, 1961; *Naiman et al.*, 1986; *Naiman et al*., 1988; *Shields et al.*, 1995; *Snodgrass & Meffe*, 1998; *Pollock et al.*, 2007; *Burchsted et al.*, 2010; *Ciechanowski et al.*, 2011; *Briggs et al.*, 2012]. These physical alterations change which heat sources and sinks are dominant and therefore impact the temperature of the stream [*Beschta et al.*, 1987; *Sinokrot & Stefan*, 1993] and beaver ponds. Furthermore, *Fuller and Peckarsky* [2011] suggest that there is a correlation between beaver pond morphology and temperature changes.

Modifications of heat sources and sinks in a system can be quantified using an energy budget [*Brown*, 1969] which estimates the heat gained and lost within a system in order to determine the total energy stored and the associated effect on temperature. There are many stream temperature models [e.g., *Brown*, 1969; *Sinokrot & Stefan*, 1993; *Chapra*, 1997; *Webb & Zhang*, 1997; *Johnson*, 2004; *Loheide & Gorelick*, 2006; *Neilson et al.*, 2010a & b; *Merck & Neilson*, 2012], but none encompass the heat fluxes that are unique to beaver ponds given the altered physical characteristics and the associated impacts on heat transfer mechanisms. Based on prior research in atypical surface waters [e.g., *Merck & Neilson*, 2012], it is expected that site-specific considerations are necessary to capture the dominant heat transfer processes and predict diverse temperatures within beaver ponds.

Influences of solar or shortwave radiation – having wavelengths between 140 and 4000 nanometers [*Meier et al.*, 2003] – is of particular importance when modeling beaver pond temperatures, because beaver ponds typically have an open canopy [*Burchsted et al.*, 2010] and shortwave radiation has been shown to be the primary driver of temperature in streams with limited shading [*Brown*, 1969; *Sinokrot & Stefan*, 1993; *Johnson*, 2004]. Some stream temperature models account for shortwave radiation penetration within the water column; however, the attenuation of shortwave radiation in the water column is often based on assumed, estimated, or calibrated values [*Meier et al.*, 2003; *Webb & Zhang*, 2004; *Westhoff et al.*, 2007; *Merck & Neilson*, 2012]. While attenuation of certain wavelengths, such as ultra-violet or photosynthetically active radiation, are commonly found through in-situ measurements [*Laurion et al.*, 2000; *Frost et al.*, 2005; *Diamond et al.*, 2005; *Belmont et al.*, 2009], the attenuation of broad-spectrum shortwave radiation is rarely obtained through measurements [*Neilson et al.*, 2010c]. However, in the context of tracking energy entering or leaving a waterbody, it is important to account for the total energy entering the system and being absorbed within different portions of the water column and bed sediments. Further, the fate of shortwave radiation within the water column is dependent on water quality [*Kirk*, 1988; *Merck & Neilson*, 2012], which emphasizes the need to have accurate in-situ methods for measuring the attenuation of shortwave radiation within the water column.

In order to address the aforementioned shortcomings within the literature, this thesis pursues the following objectives: 1) to develop a process-based temperature model which can represent the thermal regime within a beaver pond to provide insight into the impacts that beaver can have on stream temperature, and 2) to investigate methods for measuring shortwave radiation within surface waters to verify that we are representing the fate of shortwave radiation within stream temperature models accurately.

CHAPTER 2

EFFECT OF BEAVER PONDS ON STREAM TEMPERATURE[1]

Abstract

Restoration of the beaver population (*Castor Canadensis*) to streams and rivers is desirable because they are a sustainable and lower cost method of improving stream habitat when compared to human-engineered restoration efforts. Prior studies have shown that beaver colonization results in impoundments of water which increase channel width and surface area, increase sediment deposition, and slow flow velocities. While these changes can create a thermally heterogeneous environment promoting diverse aquatic communities and providing thermal refugia, there is a need to understand the spatial distribution of temperatures and to identify characteristics that produce this variability. To address these needs we developed a process-based temperature model for a beaver pond within Curtis Creek, UT. Using water temperature data distributed spatially within the pond, we delineated model segments into areas with similar temperature responses. This resulted in a main channel area and three surface transient storage (STS) zones– one of which was further segmented into two layers where thermal stratification was observed. Onsite discharge, water temperature, sediment temperature, channel geometry, and meteorological data provided information for model inputs and calibration, which includes adjusting parameters to provide a best fit between model predictions and

---

[1] Co-authored by Dr. Bethany Neilson

observed data. The model formulation accounts for advection (water inflows and outflows), heat fluxes at the air-water interface, lateral exchange between zones, vertical exchange between stratified layers, attenuation of shortwave radiation within the water column, and streambed conduction. The model captured each zone’s instream temperatures well and provided information regarding the dominant heat fluxes for each zone. Model scenarios were also developed to investigate the changes in temperatures over the life span of a beaver pond. We found that significant changes in temperature occurred only for an STS zone having a large volume of water and limited exchange with the main channel. These results can lead to insight regarding key processes and characteristics driving the thermal heterogeneity within beaver ponds over both space and time. Ultimately, this type of modeling approach can aid in future decisions regarding restoring beaver to certain stream systems and the associated temperature and ecological implications.

Introduction

Restoration of the beaver population (*Castor canadensis*) to streams and rivers is desirable because they are a sustainable [*Burchsted et al.*, 2010] and a lower cost method of improving stream habitat than human-engineered restoration efforts [*Barrett*, 1999]. Benefits for stream systems as a result of beaver activity include riparian restoration [*Shields et al.*, 1995; *Barrett*, 1999; *Albert & Trimble*, 2000] and management [*McKinstry et al.*, 2001], incised stream channel restoration [*Pollock et al*., 2007], enhanced fish habitat [*Pollock et al.*, 2004; *Billman et al.*, 2013], increased stream macroinvertebrate population diversity and riparian herb diversity [*Burchsted et al.*, 2010], habitat for waterfowl [*McKinstry et al*., 2001] and new foraging sites for insectivorous bats [*Ciechanowski et al*., 2011].

Beaver alter physical characteristics or geomorphology of streams by building dams which create impoundments or ponds [*Naiman et al.*, 1986; *Shields et al.*, 1995; *Burchsted et al.*, 2010; *Ciechanowski et al.*, 2011]. The impoundments shape the fluvial corridor of the stream by generating erosion, forming new channels, and creating multiple-thread reaches downstream of the beaver dam [*Burchsted et al.*, 2010]. Additionally, beaver ponds tend to have moderately shallow to deep water depth and an open plant canopy overhead [*Burchsted et al.*, 2010], likely in part due to the reduction of surrounding riparian vegetation resulting from beaver activity [*Naiman et al*., 1988]. Beaver ponds have low water velocities [*Ciechanowski et al.*, 2011] and, thus, deposition and accumulation of fine-grained and organic sediments [*Burchsted et al.*, 2010] that decrease the stream slope [*Pollock et al.*, 2007] and cause the formation of complex bed forms [*Briggs et al.*, 2012]. Stream width and surface area are increased [*Gard*, 1961; *Shields et al.,* 1995], as are hydraulic residence times due to the ponded waters [*Jin et al.*, 2009]. These ponds also enhance surface transient storage, which has a direct effect on the solute residence times within the system [*Jin et al.*, 2009]. Beaver dam abandonment causes further changes to stream morphology including a large reduction in pond surface area and decrease in mean channel widths and water depth [*Snodgrass & Meffe*, 1998]. Further, re-growth of some types of riparian vegetation will occur, including the coyote willow (*Salix exigua*) [*Stevens et al.*, 2003], which is common in riparian areas in

Northern Utah. Local changes in geomorphology and riparian vegetation, such as these, are important influences for habitat-scale thermal regimes [*Arscott et al.*, 2001].

Beaver activity has been observed to result in increased stream thermal heterogeneity within beaver ponds [*Majerova et al.*, manuscript in preparation, 2014]. Thermal heterogeneity contributes to biological complexity contributing to differences in community composition and rates of production for lower trophic levels [*Danehy et al.*, 2005] and affects stability and persistence of aquatic species [*Ebersole et al.*, 2003]. It provides ectothermic organisms an opportunity to thermoregulate [*Torgersen et al.*, 1999; *Ebersole et al.*, 2003] and allows for physiological efficiency of food conversion and energy conservation change [*Danehy et al.*, 2005]. Thermal heterogeneity is especially important when it comes to cold-water fish species as it provides refuges during periods of temperature stress such as the chinook salmon (Oncorhynchus tshawytscha) and steelhead trout (Oncorhynchus mykiss) [*Torgersen et al.*, 1999; *Ebersole et al.*, 2003].

Because changes in thermal heterogeneity can occur long before changes to the “average” main channel temperature are realized [*Ebersole et al.*, 2003], there is a need to understand the primary drivers of thermal heterogeneity spatially, particularly within beaver ponds. Furthermore, there is also a need to identify habitats that provide thermal refuges for fish along with factors influencing the distribution and characteristics of the thermal heterogeneity for the conservation and management of thermally marginal streams [*Ebersole et al.*, 2003]. A process-based temperature model can be used to address these needs by predicting the thermal heterogeneity within a beaver pond, allowing for a spatial understanding of temperature responses, and aiding in identifying pond characteristics that contribute to creating thermal heterogeneity.

The physical alterations to a stream as a result of beaver may change the dominant heat sources and sinks [*Beschta et al.*, 1987; *Sinokrot & Stefan*, 1993]. The changes in heat contributions due to physical alterations can be quantified by developing an energy budget [*Brown*, 1969]. Energy budgets estimate the gains and losses of energy or heat to and from a system in order to determine how much energy is stored within the system and the resulting changes in temperature.

While there are many process-based stream temperature models that have already been developed [e.g. *Brown*, 1969; *Sinokrot & Stefan*, 1993; *Chapra*, 1997; *Webb & Zhang*, 1997; *Johnson*, 2004; *Loheide & Gorelick*, 2006; *Neilson et al.*, 2010a & b; *Merck & Neilson*, 2012], none of the models encompass the heat fluxes unique to beaver ponds given the altered physical characteristics and the associated impacts on and importance of various heat transfer mechanisms. This includes the heat exchanges associated with stagnant areas or dead zones within the pond and solar radiation penetration to bed sediments.

To capture the influence of some of these heat transfer mechanisms, it is necessary to draw from the solute transport literature that has developed the concept of transient storage which is comprised of hyporheic storage (subsurface transient storage) and stagnant water or water moving slower than the main-channel flow (surface transient storage) [*Bencala & Walters*, 1983]. These types of storage are enhanced in beaver ponds [*Jin et al.*, 2009].

Some models have incorporated the influences of transient storage by accounting for heat transfer into and out of separate surface and subsurface transient storage zones [*Meier et al.*, 2003; *Neilson et al.*, 2010a & b]. However, in beaver ponds, backwater effects and the associated surface transient storage will also change shortwave radiation influences within the water column and reaching the bed sediments. Since shortwave solar radiation is often the most significant heat flux influencing temperature in streams with limited shading [*Brown*, 1969; *Sinokrot & Stefan*, 1993; *Johnson*, 2004] and beaver ponds tend to have an open overhead plant canopy [*Burchsted et al.*, 2010], it is of particular interest to understand the fate of shortwave solar radiation and the amount absorbed by the water column versus the bed sediments. Thermal stratification can also occur within beaver ponds [*Gard*, 1961; *Velinsky et al.*, 2006]; therefore, understanding when stratification occurs and what causes it may also be key to understanding solar radiation penetration because solar radiation can attenuate differently for each stratified layer due to possible differences in water quality [*Kirk*, 1988; *Merck & Neilson*, 2012].

As beaver ponds appear to possess characteristics similar to both lakes and streams, they will require site-specific considerations in model development [e.g., *Merck & Neilson*, 2012], particularly since downstream temperature effects of beaver ponds appear to be directly related to stream morphology [*Fuller & Peckarsky*, 2011]. In this paper, a process-based model will be developed and used to investigate the influence of beaver on the pond thermal regime by capturing the processes occurring within the system, determining the dominance of heat fluxes influencing specific portions of a beaver pond, and predicting the changes in temperature as the pond changes over its lifespan. This type of modeling approach will provide foundational information regarding the mechanisms influencing thermal heterogeneity within beaver ponds and therefore contribute insight regarding using beaver as a stream restoration tool for the purposes of diversifying thermal refugia.

Model Formulation

Based on the modeling approaches of *Neilson et al.* [2010a] and *Merck and Neilson* [2012] and our understanding of beaver dams, the energy budget for beaver ponds will need to account for advection (water inflows and outflows), surface heat exchange, solar radiation penetration, vertical exchange between potentially stratified layers, surface transient storage influences, and streambed conduction. The assumptions for the beaver pond temperature model are taken from both the *Merck and Neilson* [2012] and the TZTS model [*Neilson et al.*, 2010a]. These assumptions include having completely mixed and constant volume zones, isotropic thermal properties of the streambed sediments, advection in the top layer of the main channel only due to volumetric inflow and outflow, steady and non-uniform hydraulics, no mixing due to wind, simplified estimation of conduction within the streambed, and one-dimensional first-order heat transfer between the different zones. A beaver pond can generally be segmented into main channel, and surface transient storage zones where streambed sediment zones are also present beneath each surface water zone. Where stratification is present, the surface water zones are further divided vertically into individual stratified layers. Figure 1 shows a generalized schematic consisting of heat fluxes that may be represented within a beaver pond.

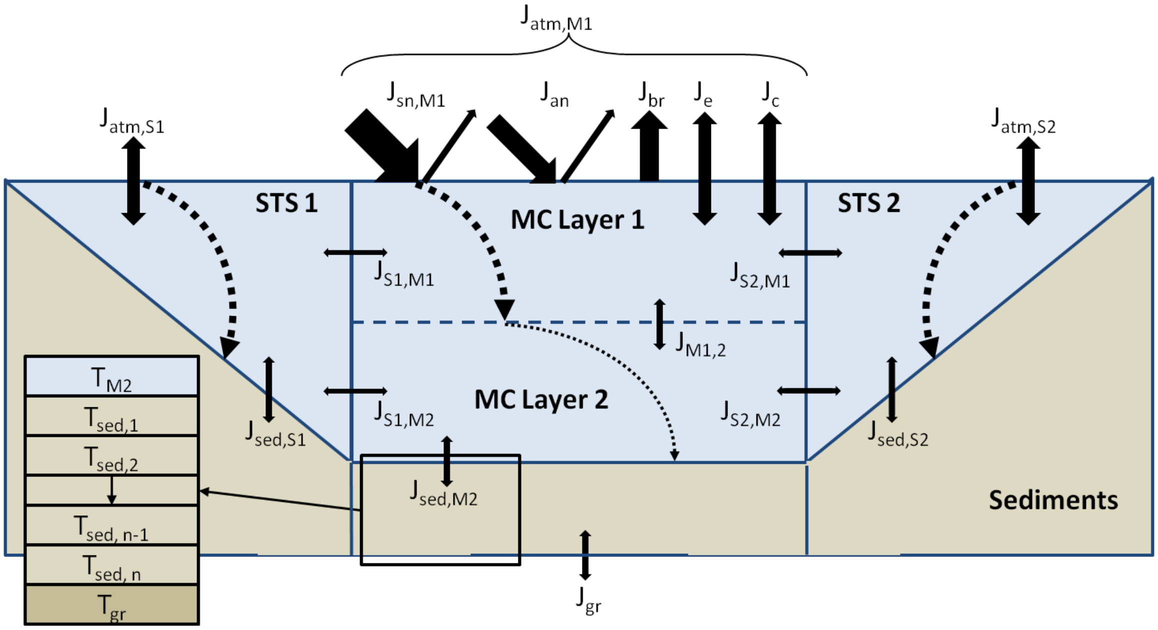

Figure 1: Example schematic of beaver pond temperature model. The beaver pond is divided into different zones (MC Layer 1 and 2, STS 1 and 2, and Sediments) with associated heat fluxes (*J*). The dotted curved line in each zone represents the fate of the solar radiation heat flux ($J_{sn,i}$). MC = Main Channel (layers 1 = M1 and 2 = M2), STS = Surface Transient Storage (zones 1 = S1 and 2 = S2), and sed = Sediments. Subscript *n* identifies individual sediment layers and *T* the temperature of each layer.

Within the example beaver pond shown in Figure 1, there is a main channel zone that is divided into two-layers to account for potential stratification within the water column. Two individual surface transient storage (STS) zones are shown to illustrate model development for a situation with multiple surface transient storage zones. Finally, there are streambed sediment zones beneath each of the main channel and STS zones providing information about conduction between the surface waters and sediments.

Based on the assumptions, energy budget Equations 1 – 4 have been developed in this work for main channel layers 1 (M1) and 2 (M2) and surface transient storage zones 1 (S1) and 2 (S2).

Equation 1

$$\frac{dT_{M1}}{dt} = \frac{Q_{in}T_{in}}{V_{M1}} - \frac{Q_{out}T_{M1}}{V_{M1}} + \frac{J_{atm,M1}A_{s,M1}}{\rho_{M1}c_pV_{M1}} + \frac{v_{M1,2}A_{s,M2}(T_{M2}-T_{M1})}{V_{M1}} + \frac{\alpha_{M1,S1}A_{cs,M1,S1}(T_{S1}-T_{M1})}{V_{M1}B_{S1}} + \frac{\alpha_{M1,S2}A_{cs,M1,S2}(T_{S2}-T_{M1})}{V_{M1}B_{S2}}$$

Equation 2

$$\frac{dT_{M2}}{dt} = \frac{J_{sn,M2}A_{s,M2}}{\rho_{M2}c_pV_{M2}} + \frac{v_{M1,2}A_{s,M2}(T_{M1}-T_{M2})}{V_{M2}} + \frac{\alpha_{M2,S1}A_{cs,M2,S1}(T_{S1}-T_{M2})}{V_{M2}B_{S1}} + \frac{\alpha_{M2,S2}A_{cs,M2,S2}(T_{S2}-T_{M2})}{V_{M2}B_{S2}} + \frac{K_{sed}A_{s,sed,M2}(T_{sed}-T_{M2})}{\rho_{M2}c_pV_{M2}z_{sed}} + \frac{\left(\left(r_{sed}J_{sn,sed,M2}\right) + \left[J_{sn,sed,M2} * 0.53 * (1-\eta)\right]\right)A_{s,M2}}{\rho_{M2}c_pV_{M2}}$$

Equation 3

$$\frac{dT_{S1}}{dt} = \frac{J_{atm,S1}A_{s,S1}}{\rho_{S1}c_pV_{S1}} + \frac{\alpha_{M1,S1}A_{cs,M1,S1}(T_{M1}-T_{S1})}{V_{S1}B_{S1}} + \frac{\alpha_{M2,S1}A_{cs,M2,S1}(T_{M2}-T_{S1})}{V_{S1}B_{S1}} + \frac{K_{sed}A_{s,sed,S1}(T_{sed}-T_{S1})}{\rho_{S1}c_pV_{S1}z_{sed}} + \frac{\left(\left(r_{sed}J_{sn,sed,S1}\right) + \left[J_{sn,sed,S1} * 0.53 * (1-\eta)\right]\right)A_{s,S1}}{\rho_{S1}c_pV_{S1}}$$

Equation 4

$$\frac{dT_{S2}}{dt} = \frac{J_{atm,S2}A_{s,S2}}{\rho_{S2}c_pV_{S2}} + \frac{\alpha_{M1,S2}A_{cs,M2,S2}(T_{M1}-T_{S2})}{V_{S2}B_{S2}} + \frac{\alpha_{M2,S2}A_{cs,M2,S2}(T_{M2}-T_{S2})}{V_{S2}B_{S2}} + \frac{K_{sed}A_{s,sed,S2}(T_{sed}-T_{S2})}{\rho_{S2}c_pV_{S2}z_{sed}} + \frac{\left(\left(r_{sed}J_{sn,sed,S2}\right) + \left[J_{sn,sed,S2} * 0.53 * (1-\eta)\right]\right)A_{s,S2}}{\rho_{S2}c_pV_{S2}}$$

Equations 5 – 7 for the sediments beneath the beaver pond use a finite-divided-differences scheme as described in *Merck and Neilson* [2012] in which the sediments are divided into layers (n = 1 to n) and boundary temperatures are used to determine heat transfer between the streambed sediments and deeper ground sediments. Each of Equations 1 – 7 provides the basis for the temperature model.

Equation 5

$$\frac{dT_{sed,i,n=1}}{dt} = \frac{J_{sn,sed,i}A_{s,sed,i}}{\rho_{sed}c_{p,sed}V_{sed}} + \frac{K_{sed}(2T_i - 5T_{sed,i,1} + 4T_{sed,i,2} - T_{sed,i,3})}{\rho_{sed}c_{p,sed}\Delta z_{sed}^2}$$

Equation 6

$$\frac{dT_{sed,i,n=2\ to\ n-1}}{dt} = \frac{K_{sed}(T_{sed,i,n-1} - 2T_{sed,i,n} + T_{sed,i,n+1})}{\rho_{sed}c_{p,sed}\Delta z_{sed}^2}$$

Equation 7

$$\frac{dT_{sed,i,n=n}}{dt} = \frac{K_{sed}(2T_{gr} - 5T_{sed,i,n} + 4T_{sed,i,n-1} - T_{sed,i,n-2})}{\rho_{sed}c_{p,sed}\Delta z_{sed}^2}$$

where Q_{in} = volumetric flow rate into main channel layer 1 (m^3 day^{-1}); Q_{out} = volumetric flow rate out of main channel layer 1 (m^3 day^{-1}); T_i = Temperature of the zone i (^oC); V_i = volume of the zone i (m^3); $A_{s,i}$ = surface area of the zone i (m^2); $A_{s,sed,i}$ = surface area of the sediments under zone i (m^2); ρ_i = water density of the zone i (g m^{-3}); c_p = specific heat capacity of the water (cal g^{-1} $^oC^{-1}$); ρ_{sed} = density of the sediments (g m^{-3}); $c_{p,sed}$ = specific heat capacity of the sediments (cal g^{-1} $^oC^{-1}$); $v_{i,j}$ = vertical heat transfer coefficient between stratified layers i and j (m day^{-1}); $\alpha_{i,j}$ = heat transfer coefficient between zones i and j (m^2 day^{-1}); z_i = depth of zone i (m); $A_{cs,i,j}$ = cross sectional area between zone i and j (m^2); B_i = average width of zone i (m); K_{sed} = thermal conductivity of the sediment (cal m^{-1} ^{o}C^{-1} day^{-1}); r_{sed} = reflectivity of the sediment; and η = porosity of the sediment. Subscripts i and j identify the main channel layers 1 = M1 and 2 = M2, surface transient storage zones 1 = S1 and 2 = S2, streambed sediments zone = sed, deep ground sediments = gr, and subscript n identifies layers within the sediments. $J_{atm,i}$ = the net surface heat exchange for zone i (cal cm^{-2} d^{-1}); $J_{sn,i}$ = shortwave solar radiation received into zone i (cal cm^{-2} d^{-1}); and $J_{sn,sed,i}$ = shortwave solar radiation reaching the streambed sediments beneath zone i (cal cm^{-2} d^{-1}). A reference list of assumptions and all variables are reiterated in Appendix A.

Net surface heat exchange for zone i ($J_{atm,i}$) can be further defined as it is comprised of shortwave solar radiation received into zone i ($J_{sn,i}$), atmospheric longwave radiation (J_{an}), longwave back radiation emitted from water (J_{br}), conduction and convection (J_c), and evaporation and condensation (J_e) (Equation 8) [*Merck & Neilson*, 2012].

$$J_{atm,i} = J_{sn,i} + J_{an} - (J_{br,i} + J_{e,i} + J_{c,i}) \quad \text{Equation 8}$$

Each heat flux is in units of calories per centimeter squared per day (cal cm^{-2} d^{-1}; for conversion to W m^{-2} see Appendix B). The solar radiation flux is measured while the other surface heat fluxes are calculated using equations found in Appendix C. In order to more accurately estimate the amount of solar radiation received by the volume of water, solar radiation attenuation with water depth is determined using Equation 9 [*Williamson et al.*, 1996; *Jin et al.*, 2000; *Neilson et al.*, 2010c; *Merck & Neilson*, 2012].

$$J_{sn,i}(z_i) = J_{sn,i}e^{-\lambda_i z_i} \quad \text{Equation 9}$$

where $J_{sn,i}(z_i)$ = the solar radiation reaching z_i (W m^{-2}), z_i = the depth of the water layer in zone i (m), and λ_i = a broad-spectrum shortwave radiation attenuation coefficient of the water layer in zone i (m^{-1}) which can be obtained via underwater measurements. Additionally reflection of solar radiation off of the streambed sediments was assumed to be 10% based on values found in *Neilson* [2006].

Methods

This basic description of the modeling approach can be adapted and applied to any beaver pond. This adaptation and application of the model will be demonstrated in the context of a beaver pond located on Curtis Creek in Blacksmith Fork Canyon, Utah.

Site Description

Curtis Creek is a 1.25 kilometer first-order perennial mountain stream located on Hardware Ranch about 15 miles east of Hyrum, Utah. It is part of a 59.5 square kilometer watershed and is a tributary to the Blacksmith Fork River and is influenced by groundwater inflows [*Schmadel et al.*, 2010; *Schmadel et al.*, 2013]. Between the summers of 2008 and 2009, beaver moved into the area and built dams along the stream. One beaver dam located near the top of a 737 meter reach of Curtis Creek has been selected for model application (Figure 2). In 2011, this beaver dam partially breached and has since been abandoned. Following abandonment, the beaver pond water surface area has decreased; however, riparian vegetation has not yet re-grown to its full extent. Understanding this current, abandoned state of the beaver pond provides the opportunity to retroactively evaluate the impact of the changes in the pond's physical characteristics throughout the pre-abandonment period on thermal heterogeneity and into the future as riparian vegetation is re-established.

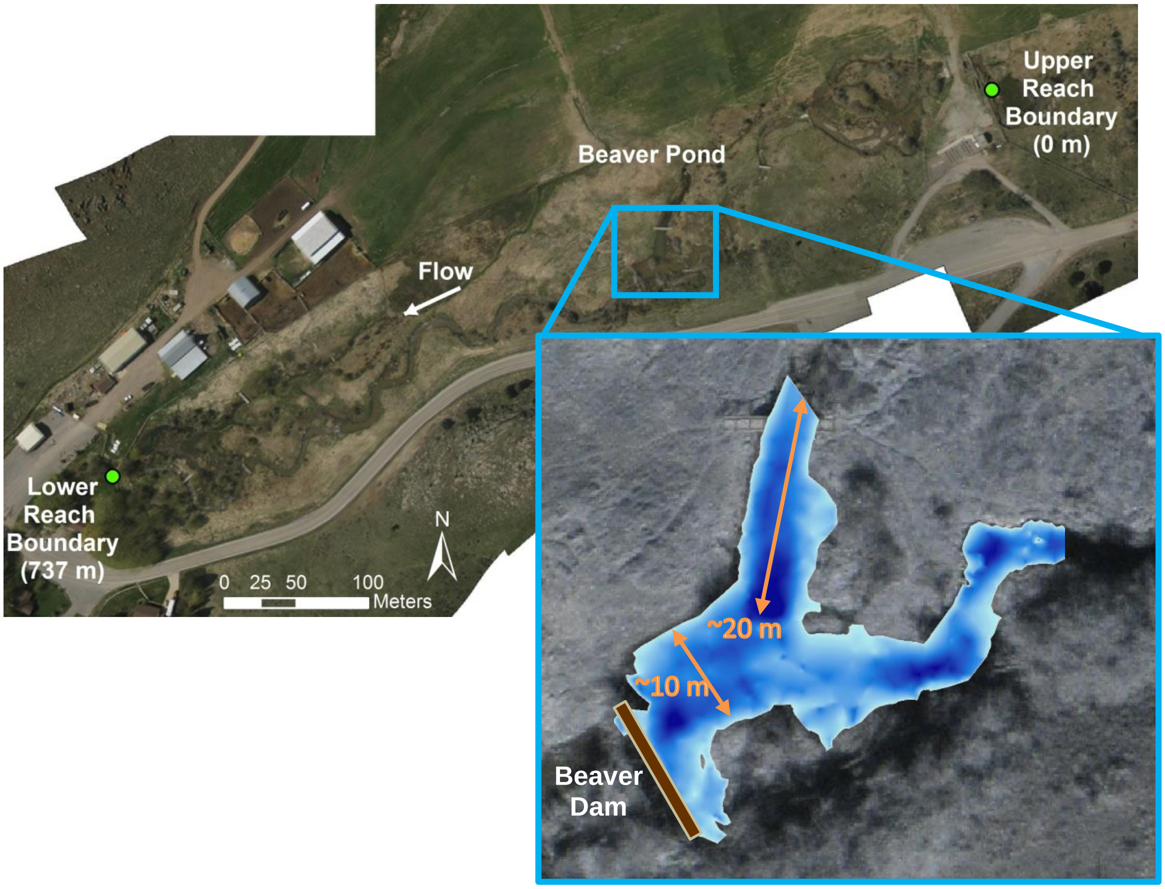

Figure 2: Aerial view from of the 737 meter reach at Curtis Creek (near Hyrum, UT) including beaver dam site location used for model data inputs and application (Image taken May 2, 2012)

Data Collection

Prior research in this area has been conducted [*Schmadel et al.*, 2010; *Schmadel et al.*, 2013; *Majerova et al.*, manuscript in preparation, 2014] and this study will build off of existing infrastructure and data types available including discharge and atmospheric measurements. Continuous stage data upstream of the beaver pond have been collected September 6, 2013 18:00 – September 26, 2013 13:55 MST at 5-minute increments using pressure transducers (Model SPXD 600 and 610; KWK Technologies, Spokane, Washington) with vented cables connected to data loggers (Model CR 206; Campbell Scientific, Logan, UT) (at the upper and lower reach boundaries shown in Figure 2). From these data, discharge was calculated using rating curves based on the stage-discharge relationship (Equation 12) as described in *Schmadel et al.* [2010].

$$Q = aZ^b \qquad \text{Equation 10}$$

Q = is the predicted stream discharge (L s^{-1}), a and b = regression parameters (16.08 and 4.17, respectively), and Z = stage measured by the pressure transducer (m).

Continuous water temperature data were collected September 6, 2013 18:00 – September 26, 2013 13:55 MST at 5-minute increments using HOBO Pro v2 temperature sensors (Onset Computer Corporation, Cape Cod, MA). Sixty-four sensors were placed in the water throughout the pond and a sensor located upstream of the beaver pond was chosen to provide the temperature accompanying the volumetric flow coming into the beaver pond as the upper boundary condition to the model. The remaining temperature sensors were intended to aid in the delineation of the main channel and STS zone boundaries (Figure 3). Because water depth varies throughout the pond, sensors were also placed in vertical arrays (placed at different depths within the water column at the same location) to determine if stratification was occurring.

To better understand the channel geometry, a survey of the beaver pond was conducted using differential rtkGPS (Model Trimble® R8, Global Navigation Satellite System, Dayton, Ohio) in which point locations along the water surface edge and bottom of the pond were recorded. From these data, a 5 cm resolution digital elevation model was developed and used to calculate the water surface area, water volume, mixing lengths, and average water depth for each zone. Further, the interfacial area between each zone was determined using spatial analysis tools within ArcGIS 10.1.

Meteorological data were taken from an onsite weather station to provide inputs to determine the net heat exchange at the water surface. Continuous air temperature, relative humidity, and wind speed data were measured from September 6, 2013 18:00 – September 26, 2013 14:00 MST at one-hour increments. Continuous solar radiation data were also collected for September 6, 2013 18:00 – September 26, 2013 13:55 MST at five-minute increments using two pyranometers (Model LP02; Hukseflux Thermal Sensors, Delft, Netherlands) connected to a data logger (Model CR 1000; Campbell Scientific, Logan, UT) placed in a location that receives little to no shading. One pyranometer was installed face-up to measure incoming shortwave radiation while the other was installed face-down to measure shortwave radiation being reflected off of the water surface. The incoming minus reflected shortwave radiation was used as the net incoming shortwave radiation penetrating the water surface.

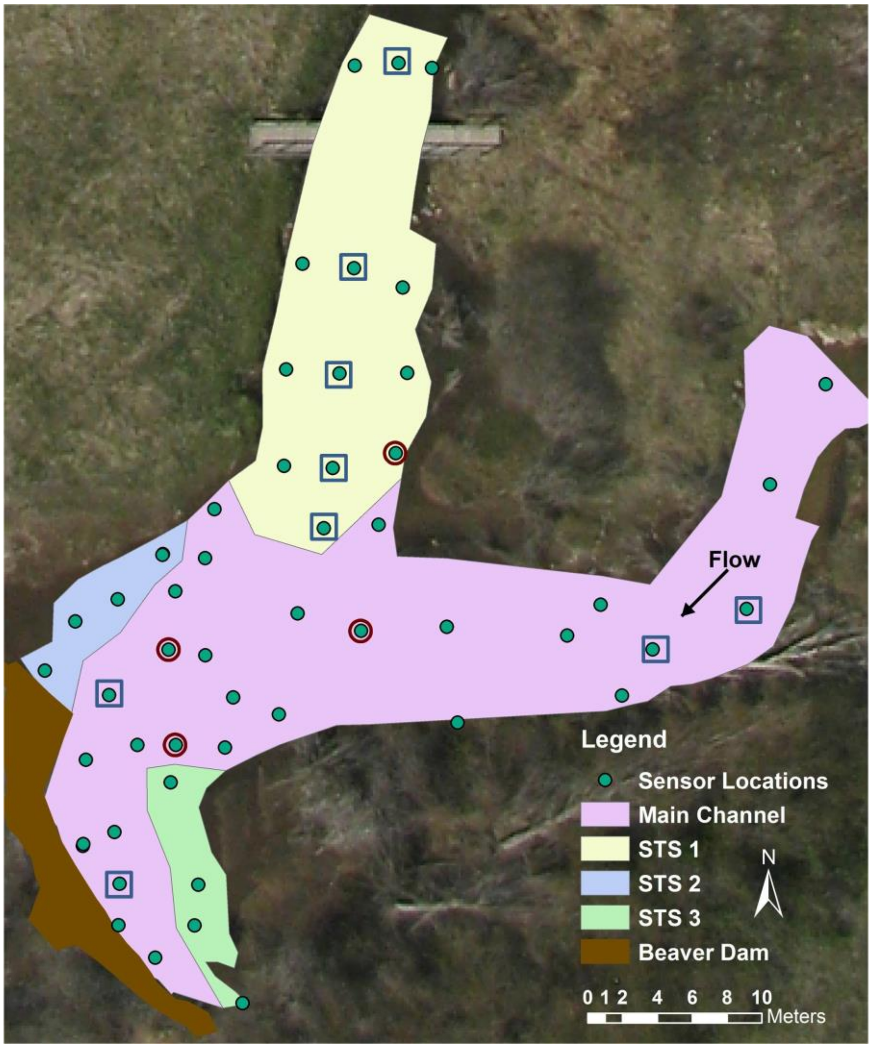

Figure 3: Calibration segmentation of Curtis Creek beaver pond into zones based on observed water temperature data collected September 6 – 26, 2013 at the sensor locations shown (data in Appendix E). Locations where water temperature data were collected at different depths are shown with a square and locations where sediment temperature data were collected are circled.

Site-Specific Model Formulation

The water temperature data collected were used to segment the beaver pond into zones containing similar temperatures (Figure 3). This segmentation resulted in four surface water zones: one main channel zone and three STS zones. STS zone 1 was further segmented into two layers due to stratification (Figures E.1-5 in Appendix E). Four streambed sediment zones were also segmented to match its corresponding surface water zone. The overall energy balance equations (Equations 11-15) for the main channel (M1), stratified STS zone 1 layer 1 and 2 (S11 and S12), and STS zones 2 and 3 (S2 and S3) as derived and extended from Equations 1-4 are as follows:

Equation 11

$$\begin{aligned}\frac{dT_{M1}}{dt} = \frac{Q_{in}T_{in}}{V_{M1}} - \frac{Q_{out}T_{M1}}{V_{M1}} + \frac{J_{atm,M1}A_{s,M1}}{\rho_{M1}c_pV_{M1}} + \frac{\alpha_{S11,M1}A_{cs,S11,M1}}{\mathrm{B}_{S11}V_{M1}}(T_{S11} - T_{M1}) \\ + \frac{\alpha_{S12,M1}A_{cs,S12,M1}}{\mathrm{B}_{S12}V_{M1}}(T_{S12} - T_{M1}) + \frac{\alpha_{M1,S2}A_{cs,M1,S2}}{\mathrm{B}_{S2}V_{M1}}(T_{S2} - T_{M1}) \\ + \frac{\alpha_{M1,S3}A_{cs,M1,S3}}{\mathrm{B}_{S3}V_{M1}}(T_{S3} - T_{M1}) + \frac{K_{sed}A_{sed,M1}\left(T_{sed,M1} - T_{M1}\right)}{z_{sed}\rho_{M1}c_pV_{M1}} \\ + \frac{\left(\left(r_{sed}J_{sn,sed,M1}\right) + \left[J_{sn,sed,M1} * 0.53 * (1-\eta)\right]\right)A_{s,M1}}{\rho_{M1}c_pV_{M1}}\end{aligned}$$

Equation 12

$$\frac{dT_{S11}}{dt} = \frac{J_{atm,S11}A_{s,S11}}{\rho_{S11}c_pV_{S11}} + \frac{\alpha_{S11,M1}A_{cs,S11,M1}}{\mathrm{B}_{M1}V_{S11}}(T_{M1} - T_{S11}) + \frac{v_{S11,12}A_{s,S12}(T_{S12} - T_{S11})}{V_{S11}}$$

Equation 13

$$\begin{aligned}\frac{dT_{S12}}{dt} = \frac{J_{sn,S12}A_{s,S12}}{\rho_{S12}c_pV_{S12}} + \frac{v_{S11,12}A_{s,S12}(T_{S11} - T_{S12})}{V_{S12}} + \frac{\alpha_{S12,M1}A_{cs,S12,M1}}{\mathrm{B}_{M1}V_{S12}}(T_{M1} - T_{S12}) \\ + \frac{K_{sed}A_{sed,S12}\left(T_{sed,S12} - T_{S12}\right)}{\rho_{S12}c_pV_{S12}z_{sed}} \\ + \frac{\left(\left(r_{sed}J_{sn,sed,S12}\right) + \left[J_{sn,sed,S12} * 0.53 * (1-\eta)\right]\right)A_{s,S12}}{\rho_{S12}c_pV_{S12}}\end{aligned}$$

Equation 14

$$\frac{dT_{S2}}{dt} = \frac{J_{atm,S2}A_{s,S2}}{\rho_{S2}c_pV_{S2}} + \frac{\alpha_{S2,M1}A_{cs,S2,M1}}{\mathrm{B}_{M1}V_{S2}}(T_{M1} - T_{S2}) + \frac{K_{sed}A_{sed,S2}\left(T_{sed,S2} - T_{S2}\right)}{\rho_{S2}c_pV_{S2}z_{sed}} + \frac{\left(\left(r_{sed}J_{sn,sed,S2}\right) + \left[J_{sn,sed,S2} * 0.53 * (1-\eta)\right]\right)A_{s,S2}}{\rho_{S2}c_pV_{S2}}$$

Equation 15

$$\frac{dT_{S3}}{dt} = \frac{J_{atm,S3}A_{s,S3}}{\rho_{S3}c_pV_{S3}} + \frac{\alpha_{M1,S3}A_{cs,M1,S3}}{\mathrm{B}_{\mathrm{M1}}V_{S3}}(T_{M1} - T_{S3}) + \frac{K_{sed}A_{sed,S3}\left(T_{sed,S3} - T_{S3}\right)}{\rho_{S3}c_pV_{S3}z_{sed}} + \frac{\left(\left(r_{sed}J_{sn,sed,S3}\right) + \left[J_{sn,sed,S3} * 0.53 * (1-\eta)\right]\right)A_{s,S3}}{\rho_{S3}c_pV_{S3}}$$

The overall energy balance equations for the streambed sediments are the same as found Equations 5 – 7 and derivations for the surface water and sediment energy balance equations for this application can be found in Appendix A. The temperature predictions for the zones within the beaver pond are estimated using Euler’s method as a numerical approximation for the energy balance equations (Equations 1 – 7) and the model code is written in Microsoft’s Visual Basic for Applications (VBA).

Due the magnitude of the data collection, the only parameters to be calibrated within the model include exchange coefficients between the zones and the stratified layers. These exchange coefficients include lateral exchange between the main channel and STS zone 1 layer 1 ($\alpha_{M1,S11}$), main channel and STS zone 1 layer 2 ($\alpha_{M1,S12}$), main channel and STS zone 2 ($\alpha_{M1,S2}$), main channel and STS zone 3 ($\alpha_{M1,S3}$), and vertical exchange between STS zone 1 layers 1 and 2 ($v_{S11,12}$). The model was calibrated manually starting with the parameters that only interact with one other zone. Since STS zones 2 and 3 only interact with the main channel, their lateral exchange coefficients were first calibrated using values ranging from 10^4 to 10^9 cm^2 day^{-1}. Next STS zone 1 layers 1 and 2 lateral exchange coefficients relating to the main channel were calibrated using values ranging from 10^4 to 10^9 cm^2 day^{-1} while the vertical exchange coefficient between the layers was calibrated simultaneously using values from 0 to 200 cm day^{-1}. The combination of exchange coefficients producing the smallest root mean squared error value (RMSE) in each respective zone were chosen as the calibrated exchange coefficients. The RMSE for each zone was calculated using Equation 16 [*Caissie et al.*, 2001]:

Equation 16

$$RMSE_i = \sqrt{\frac{\sum\left(T_{pred,i} - T_{obs,i}\right)^2}{n_i}}$$

where $T_{pred,i}$ = predicted temperature for zone i (°C); $T_{obs,i}$ = averaged observed temperature within zone i (°C); n_i = number of observation time steps for zone i.

To determine the applicability of the model under different conditions, it was corroborated using a data set from a different time period. Again, water temperature data collected were used to segment the beaver pond into zones containing similar temperatures which also resulted in four similar surface water zones: one main channel zone and three STS zones with one STS zone segmented into two layers due to stratification. Four streambed sediment zones were also segmented to match the corresponding surface water zones. This meant that we tested the general model representation and transferability of the calibrated exchange coefficients to a slightly different model segmentation with similar size STS zones.

For the corroboration, data were collected May 30, 22:00 – June 6, 2012 15:00 UTC using methods similar to the model calibration. Continuous stage discharge data were collected at 5-minute increments and discharge calculated using a stage-discharge relationship, continuous water temperature data were collected at 10-minute increments using 75 sensors placed throughout the beaver pond including one sensor upstream to provide a boundary condition, and meteorological data were taken from the Little Bear River WATERS Test Bed Utah State University Experimental Farm weather station near Wellsville, UT (approximately 22 miles from Curtis Creek) [*Utah Water Research Laboratory*, unpublished data, 2009] where incoming solar radiation was considered net solar radiation entering the water surface. The boundary condition for the deep ground sediment temperature was based on measurements taken around the same time period in 2011 using temperature sensors (Model HOBO Pro v2; Onset Computer Corporation, Cape Cod, MA) approximately 55 centimeters deep and assumed constant at 7.5 °C while the soil thermal properties were assumed the same as those measured during the 2013 calibration time period. Additionally, the bathymetry information from the calibration period was applied in the corroboration because there was minimal deposition and scour during this period due to stable flow conditions and minimal spring runoff in 2012. However, differences in water surface elevations were collected specific to the corroboration time period which is key in establishing the appropriate volumes and surface areas for this different time period. The segmentation of the beaver pond into zones for the corroboration is shown in Figure 4.

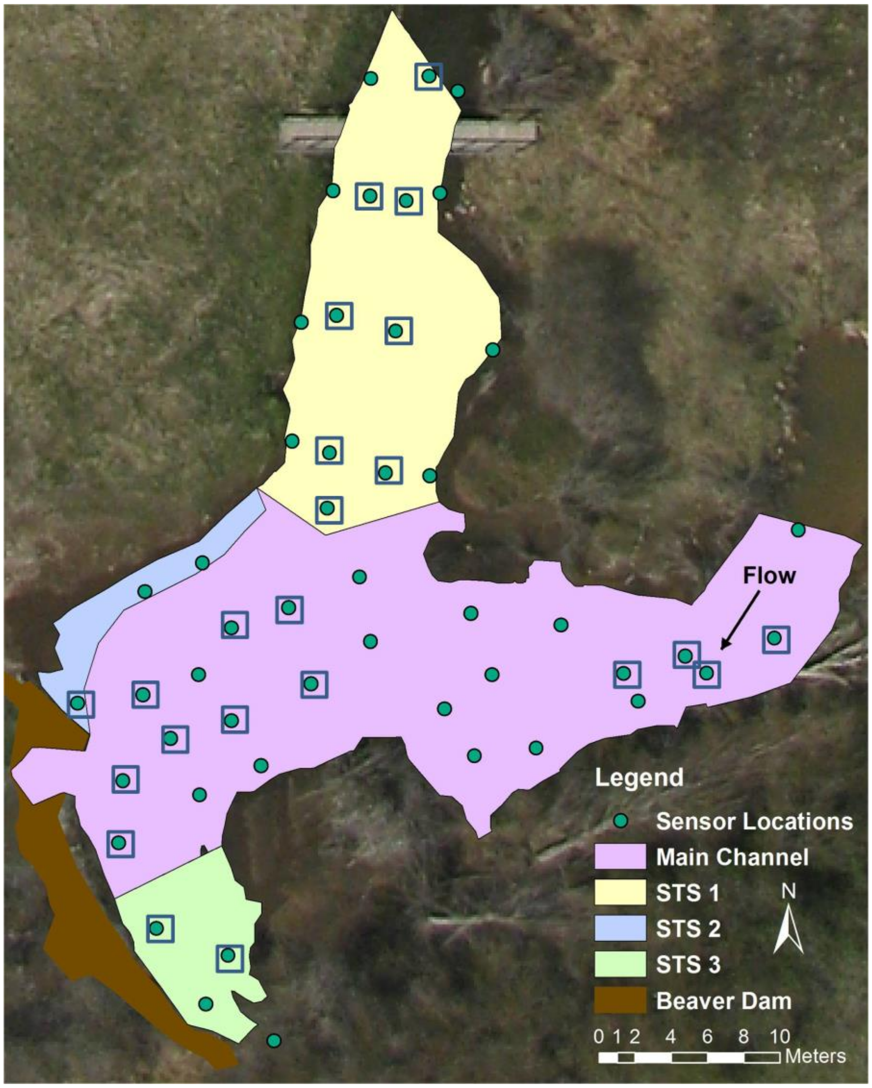

Figure 4: Corroboration segmentation of Curtis Creek beaver pond into zones based on observed water temperature data collected May 30 – June 6, 2012 at the sensor locations shown. Locations where water temperature data were collected at different depths are shown with a square.

Scenario Application

Following corroboration, scenarios were developed using the calibrated model to demonstrate the utility of the model in the context of understanding the influences of beaver dam life cycles. Since the calibration data set was collected after relatively recent abandonment of the beaver dam, it is important to note that the pond had significant sediment deposition, reduced surface area compared to initial impoundment formation, a layer of aquatic vegetation in STS zone 1, and little shading due to riparian vegetation. Three scenarios were developed and compared against the current state of the beaver pond to illustrate potential changes in temperature responses throughout the beaver pond (Table 1). These scenarios describe the different geomorphologic changes incurred within a beaver pond during different portions of the beaver dam lifespan.

Scenario 1 involves the initial impoundment formation after a beaver dam is first built in which the STS zone surface areas were increased while the average depths are reduced due to the water overflowing the banks of the original stream channel (Figure 5). This scenario was based on the pond initially experiencing a higher dam head when it was first built and lacking the current sedimentation and aquatic vegetation found within the base case scenario.

Scenario 2 includes the effect of sediment deposition primarily influencing the main channel and STS zones 2 and 3. The zone volume and average depth were doubled and aquatic vegetation removed from the Base Case scenario in order to describe the period of time prior to the present sediment deposition (Figure 6).

Table 1: A description of the current conditions of the beaver pond (base case scenario) as compared to each of the three model scenarios. The scenarios represent a change from the base case condition and include initial impoundment formation, sediment deposition, aquatic vegetation growth, and riparian vegetation re-growth. The numeric values quantifying the physical alterations for each of the scenarios were chosen based on qualitative observations made throughout the lifespan of the beaver dam. For Scenarios 1 and 2, STS zone 1 layer 2 adopted the same extinction coefficient as layer 1.

	Main Channel	**STS zone 1**	**STS zone 2**	**STS zone 3**
Base Case: Abandoned Beaver Dam	Sedimentation Present	Aquatic vegetation present: no solar radiation penetration to Layer 2	Sedimentation Present	Sedimentation Present
	Volume, Surface Area, Average Depth = 100%	Volume, Surface Area, Average Depth = 100%	Volume, Surface Area, Average Depth = 100%	Volume, Surface Area, Average Depth = 100%
Scenario 1: Initial Impoundment Formation (high beaver dam head)	200% average volume increase from sediment removal	200% surface area increase from overflowing stream banks	200% surface area increase from overflowing stream banks	200% surface area increase from overflowing stream banks
	200% average depth increase from sediment removal	50% average depth decrease from overflowing stream banks	200% average depth increase from sediment removal	200% average depth increase from sediment removal
		Aquatic vegetation from base case removed - Solar radiation allowed to penetrate through layer 2	25% average depth decrease from overflowing stream banks	25% average depth decrease from overflowing stream banks
Scenario 2: Sediment Deposition (low beaver dam head)	200% depth increase from sediment removal	Aquatic vegetation from base case removed - Solar radiation allowed to penetrate through layer 2	200% depth increase from sediment removal	200% depth increase from sediment removal
Scenario 3: Riparian Vegetation Re-Growth Post-Abandonment	Solar Radiation Reduced by 50% shading	Solar Radiation Reduced by 50% shading	Solar Radiation Reduced by 50% shading	Solar Radiation Reduced by 50% shading

Finally, Scenario 3 describes how the pond temperatures may change once the coyote willow (*Salix exigua*) fully returns resulting in shading of the pond waters. To demonstrate this scenario the magnitude of the incoming solar radiation data used in the Base Case scenario was decreased in half to describe half of the pond being shaded by riparian vegetation after its re-growth (Figure 7).

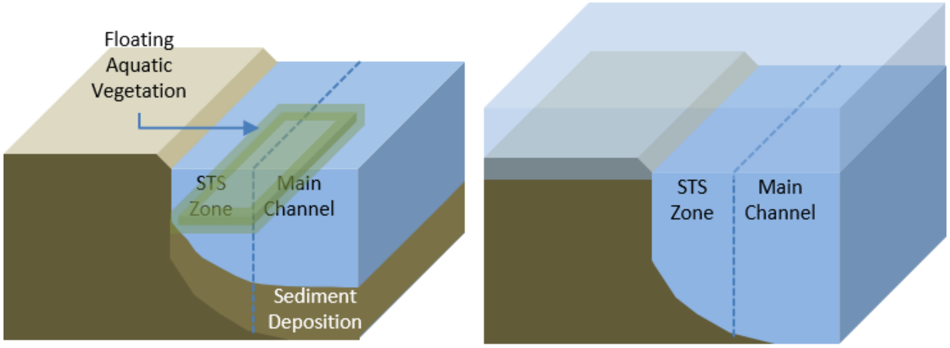

Figure 5: Depiction of the stream channel for Base Case (left) and Scenario 1 after the initial impoundment formation (right) which increased water surface area and volume while decreasing average water depth in the STS zone due to inundation of the floodplain

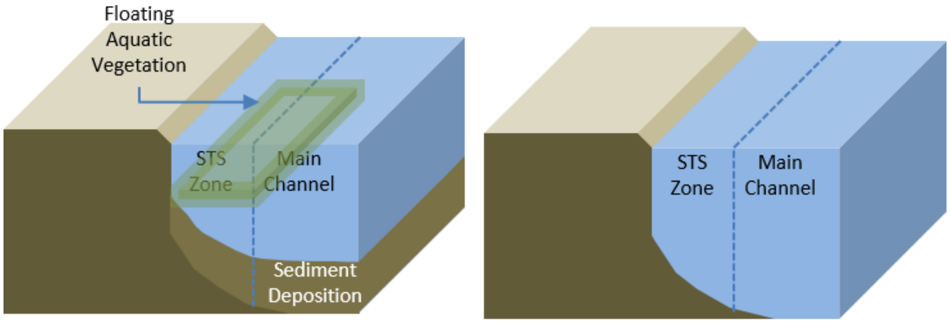

Figure 6: Depiction of the beaver pond for the sedimented Base Case scenario which resulted in smaller zone volume and average water depth (left) and Scenario 2 that represents the beaver dam prior to sediment deposition (right)

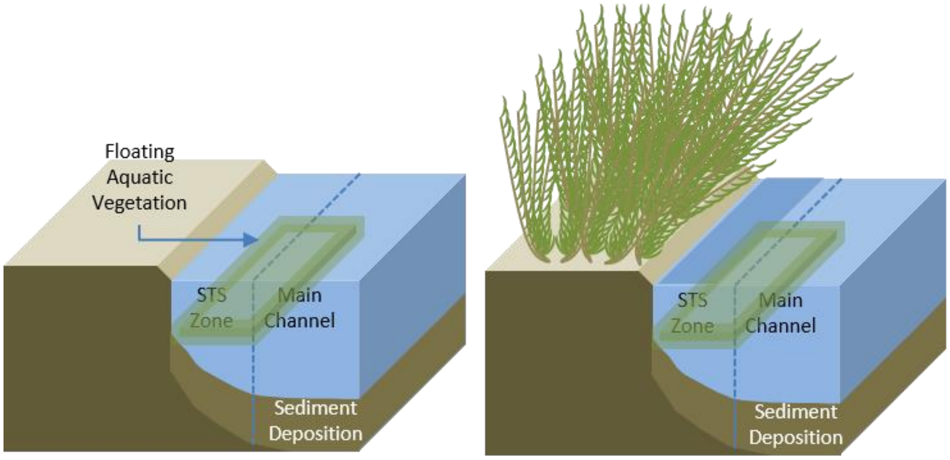

Figure 7: Depiction of the beaver pond Base Case scenario prior to riparian vegetation re-growth following beaver dam abandonment (left) and Scenario 3 after riparian vegetation re-growth following beaver dam abandonment which increased shading and therefore decreased the amount of incoming solar radiation reaching the pond waters (right)

Results

Results from the data collected for the model calibration including discharge, inflow water temperature, air temperature, solar radiation, wind speed, relative humidity, deep ground sediment temperature, and channel geometry data are shown in Appendix F. Likewise the results from the data collected for the model corroboration including discharge, inflow water temperature, air temperature, solar radiation, wind speed, relative humidity, and channel geometry data are shown in Appendix G.

Table 2 shows the values of the calibrated exchange coefficient parameters describing the exchange between the main channel and the various STS zones in addition to the exchange experienced between STS zone 1 layers 1 and 2.

Table 2: Calibrated exchange coefficients describing lateral exchange and stratified layer vertical exchange used within model predictions

STS Zone 1 Layer 1 with Main Channel (cm^2 day^{-1})	$\alpha_{M1,S11}$	2.8 x 10^7
STS Zone 1 Layer 2 with Main Channel (cm^2 day^{-1})	$\alpha_{M1,S12}$	2.0 x 10^7
STS Zone 2 with Main Channel (cm^2 day^{-1})	$\alpha_{M1,S2}$	4.1 x 10^8
STS Zone 3 with Main Channel (cm^2 day^{-1})	$\alpha_{M1,S3}$	4.1 x 10^8
STS Zone 1 Layers 1 and 2 (cm day^{-1})	$v_{S11,12}$	30

Exchange coefficients between the main channel and STS zone 1 layers 1 and 2 were calibrated to 2.8 x 10^7 and 2.0 x 10^7 cm^2 day^{-1}, respectively while the exchange coefficients between the main channel and STS zones 2 and 3 were each calibrated to 4.1 x 10^8 cm^2 day^{-1}, approximately an order of magnitude higher than the exchange coefficients for STS zone 1 layers 1 and 2. The values are comparable within one order of magnitude of exchange coefficients found in *Neilson et al.* [2010a & b].

The calibrated temperature plots for each zone (Figure 8) show that the model is predicting the temperatures within each of the zones reasonably well. RMSE values for each zone are shown in Table 3. The residuals or differences in temperature (ΔT) of calibrated model predictions subtracted from the observed data (Figure 9) show that the temperature predictions vary from the observed data by minimum and maximum differences of -0.11 to 0.27 °C for the main channel, -2.29 to 2.00 °C for STS zone 1 layer 1, -0.60 to 1.49 °C for STS zone 1 layer 2, -0.09 to 0.92 for STS zone 2, and -0.34 to 1.53 °C for STS zone 3, respectively.

Table 3: Calibration RMSE values for each zone within the beaver pond comparing model predictions to observed data

Zone	**RMSE**
Main Channel	0.07
STS zone 1 layer 1	1.14
STS zone 1 layer 2	0.58
STS zone 2	0.35
STS zone 3	0.44

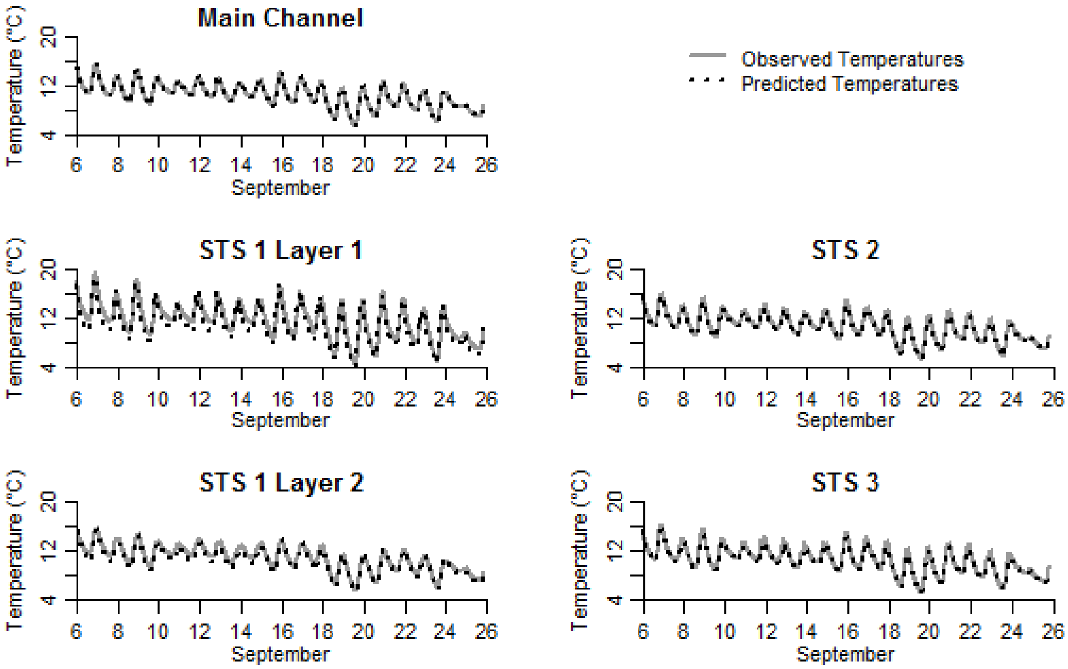

Figure 8: Calibrated water temperature predictions compared against observed data from September 6 – 26, 2013 for the main channel, surface transient storage (STS) zones 1 layers 1 and 2, STS zone 2, and STS zone 3

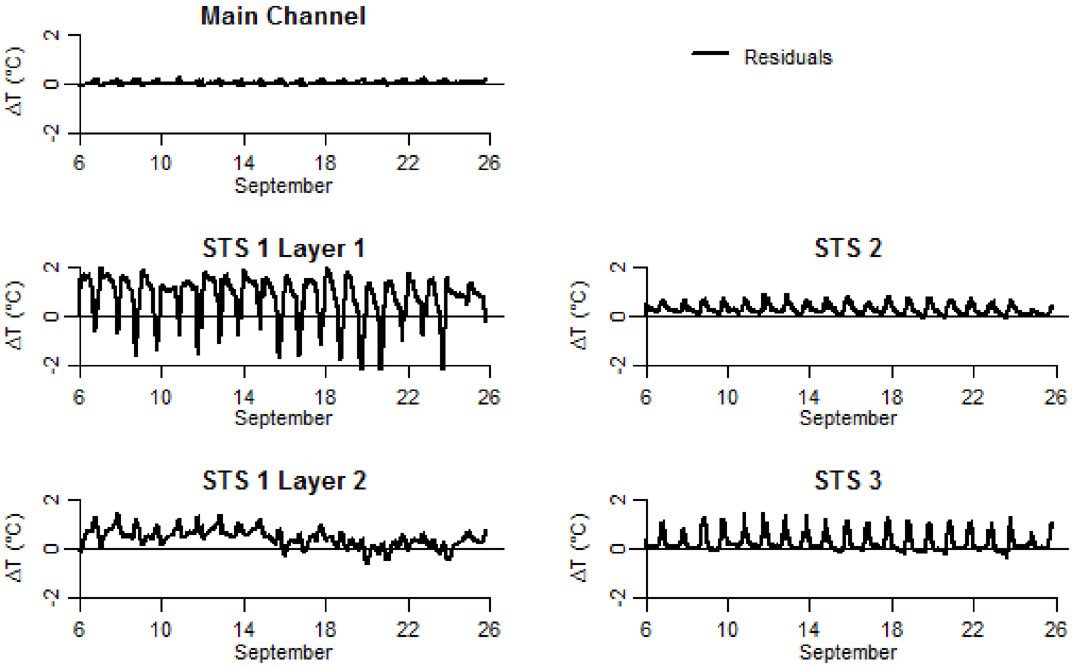

Figure 9: Residuals (ΔT) from calibrated water temperature observations and predictions from September 6 – 26, 2013 for the main channel, surface transient storage (STS) zones 1 layers 1 and 2, STS zone 2, and STS zone 3

When investigating the individual heat fluxes influencing the temperature of each zone (Figure 10), all of the zones except STS zone 1 layer 2 are dominated by the air-water interface including atmospheric longwave radiation, shortwave radiation, water longwave radiation, conduction/convection, and evaporation/condensation. STS zone 1 layer 1 is particularly dominated by incoming shortwave radiation. Since STS zone 1 layer 2 does not come in contact with the atmosphere it is instead dominated by lateral exchange with the main channel and vertical exchange with STS zone 1 layer 1. It is of interest to note that while streambed conduction is present for each of the zones it is not a significant influence of heat for any of the zones.

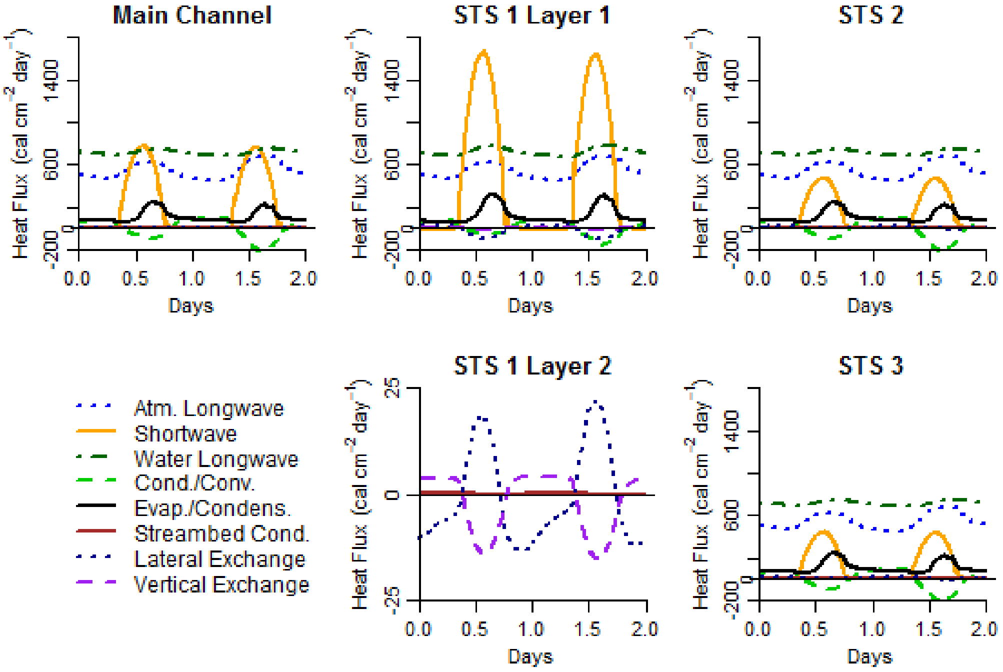

Figure 10: Calibration heat flux magnitude predictions over a two-day period of time (September 19-20, 2013) for the main channel, surface transient storage (STS) zones 1 layers 1 and 2, STS zone 2, and STS zone 3. Legend: Atm. Longwave = atmospheric longwave radiation, Shortwave = shortwave radiation, Water Longwave = water longwave radiation, Cond./Conv. = conduction/convection, Evap./Condens. = evaporation/condensation, Streambed Cond. = streambed conduction

From the predictions of sediment temperature plotted alongside observed sediment temperature data (Figure 11) and the associated residuals (observed minus predicted sediment temperature) (Figure 12), it is apparent that for the main channel, STS zone 2, and STS zone 3 that the model is generally over-predicting the temperature for the layers closest to the sediment-water interface (i.e., 5 cm, 10 cm, and 25 cm) varying up to 4 °C from the observed data for the main channel and up to 5 °C for STS zones 2 and 3; however, the predictions for sediment temperatures at depths of 50 cm and 75 cm are much more closely aligned with the observed sediment temperature data varying about 1 °C from the observed data. On the other hand, the model is predicting the temperature for the sediments below zone STS 1 very well generally varying less than 0.5 °C from the observed data. The RMSE values for each sediment layer in each zone can be found in Appendix D.

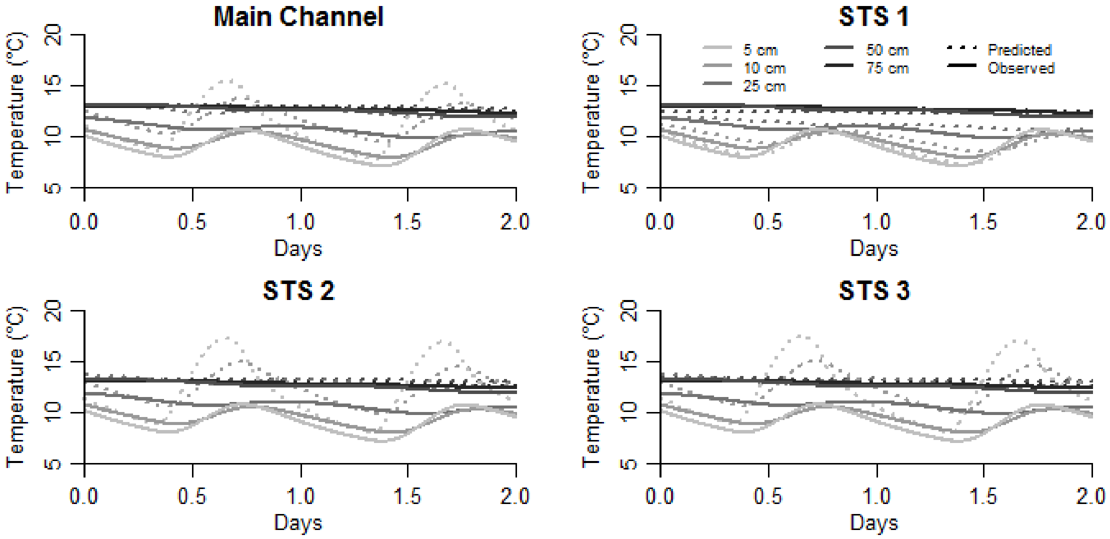

Figure 11: Calibrated sediment temperature predictions compared against observed data from September 6 – 26, 2013 at depths of 5 cm, 10 cm, 25 cm, 50 cm, and 75 cm for the main channel zone and surface transient storage (STS) zones 1 – 3

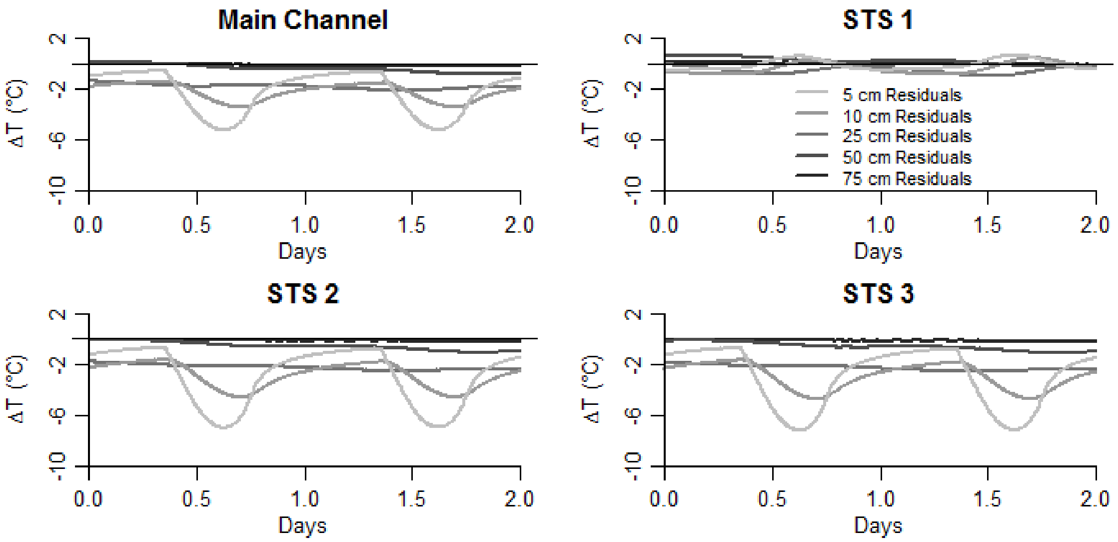

Figure 12: Residuals (ΔT) from calibrated sediment temperature observations and predictions over a two-day period for the main channel and surface transient storage (STS) zones 1, 2, and 3

For the corroboration period, the predicted temperatures track observed temperatures in the main channel and STS zone 3 very well (Figure 13, Table 4).

Table 4: Corroboration RMSE values for each zone within the beaver pond comparing model predictions to observed data

Zone	**RMSE**
Main Channel	0.13
STS zone 1 layer 1	3.51
STS zone 1 layer 2	2.42
STS zone 2	1.23
STS zone 3	0.19

The associated residuals (subtracting the model predictions from the observed data, Figure 14) show the main channel ranges from -0.11 to 0.37 °C and the STS zone 3 ranges from -0.07 to 0.47 °C. In STS zone 2, the model is under-predicting the temperatures where the residuals range from 0.00 to 2.34 °C. For STS zone 1 layers 1 and

2, the model is significantly under-predicting the temperatures where the residuals range from 0.00 to 6.85 °C and 0.00 to 4.31 °C, respectively.

When evaluating the dominant heat fluxes influencing of each zone (Figure 15) all of the zones except STS zone 1 layer 2 are dominated by the heat fluxes at the air-water interface including atmospheric longwave radiation, shortwave radiation, water longwave radiation, conduction/-convection, and evaporation/condensation which is similar to the calibration predictions. Again, STS zone 1 layer 1 is particularly dominated by incoming shortwave radiation and STS zone 1 layer 2 is dominated by exchange primarily lateral exchange with the main channel in this case.

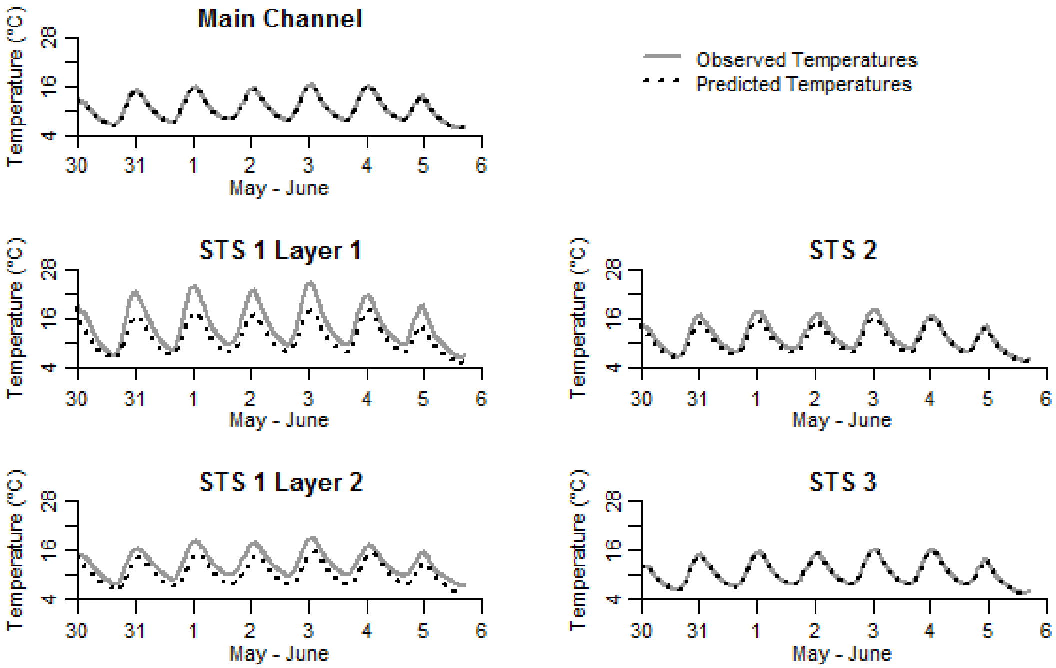

Figure 13: Corroborated water temperature predictions compared against observed data from May 30 – June 6, 2012 for the main channel, surface transient storage (STS) zones 1 layers 1 and 2, STS zone 2, and STS zone 3

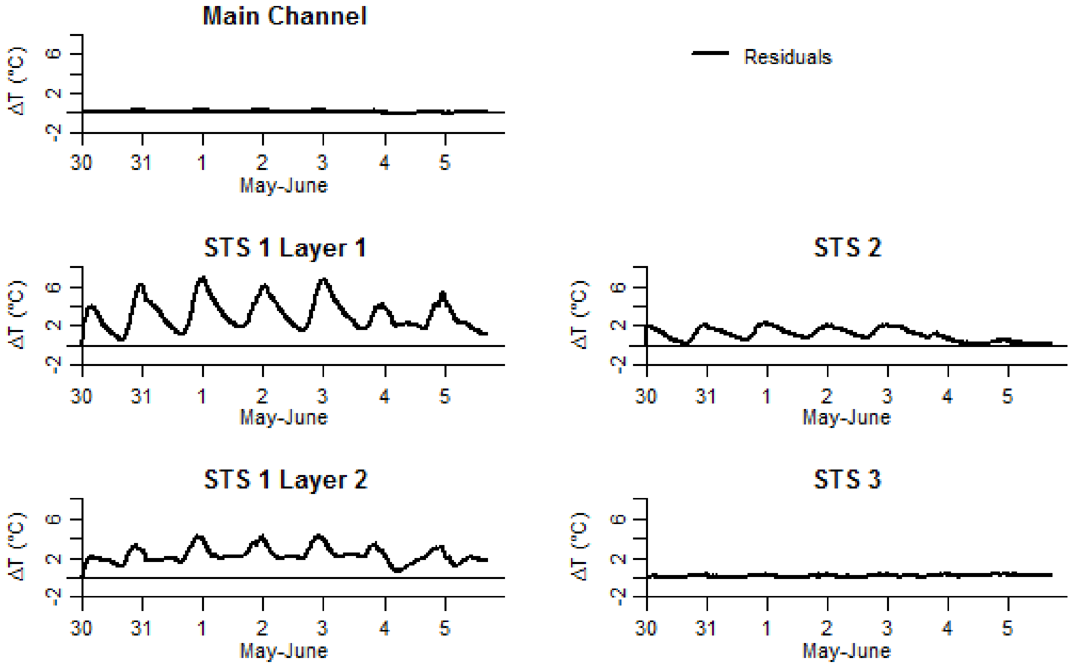

Figure 14: Residuals (ΔT) from corroborated water temperature observations and predictions from May 30 – June 6, 2012 for the main channel, surface transient storage (STS) zones 1 layers 1 and 2, STS zone 2, and STS zone 3.

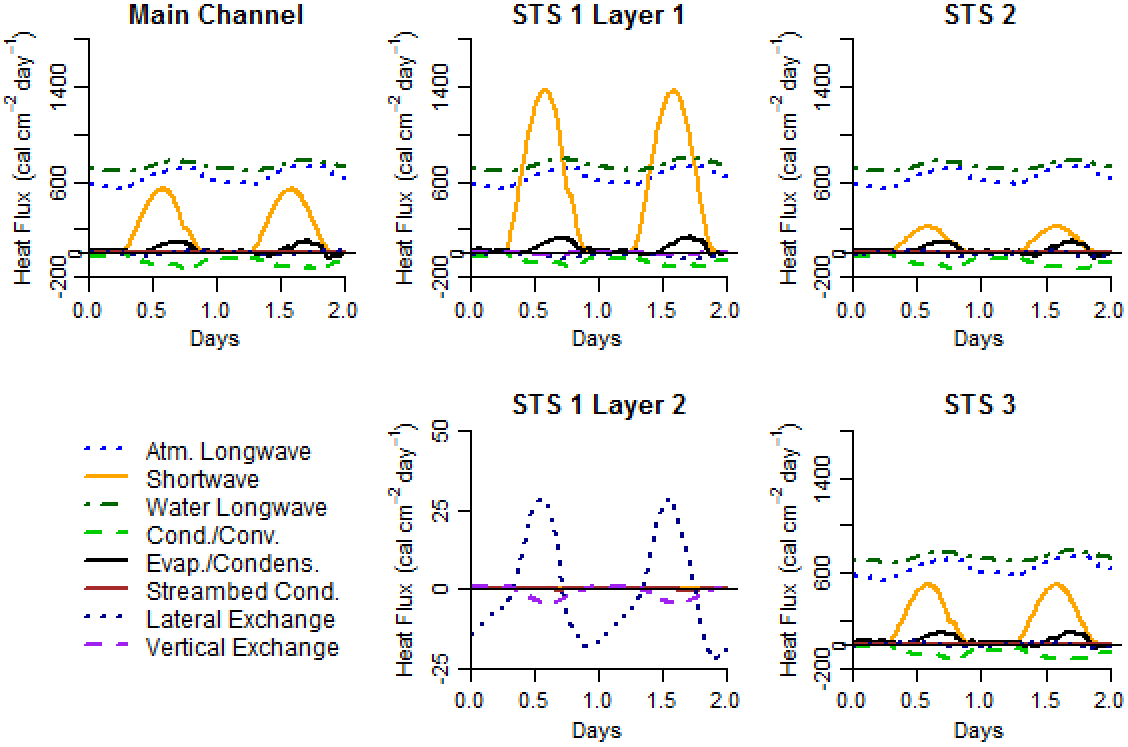

Figure 15: Corroborated heat flux magnitude predictions over a two-day period of time (May 31-June 1, 2012) for the main channel, surface transient storage (STS) zones 1 layers 1 and 2, STS zone 2, and STS zone 3. Legend: Atm. Longwave = atmospheric longwave radiation, Shortwave = shortwave radiation, Water Longwave = water longwave radiation, Cond./Conv. = conduction/convection, Evap./Condens. = evaporation/condensation, Streambed Cond. = streambed conduction

In Figure 16, water temperature predictions from the model calibration period (Base Case) are compared against Scenario 1. Figure 17 consists of the residuals in which temperature predictions from Scenario 1 are subtracted from the Base Case temperature predictions.

Based on these results it appears the increasing STS zone surface area and decreasing average water depth results in almost insignificant changes (within measurement error) for the main channel and STS zones 2 and 3. While STS zone 1 layer 2 experienced residuals reaching up to 0.4 °C the most notable changes were found in STS zone 1 layer 1. Here the scenario temperature predictions were approximately 4 °C cooler than the Base Case predictions.

In Figure 18, water temperature predictions from the model calibration are compared against Scenario 2 while Figure 19 shows the corresponding residuals. Similar to Scenario 1, for Scenario 2 the main channel and STS zones 2 and 3 the temperature differences generally ranged from -0.2 to 0.2 °C which is within measurement error of the temperature sensors used, whereas the temperatures within STS zone 1 ranged between 0 to 4 °C for layer 1 and between 0 to 0.4 °C for layer 2. Figure 20 shows the calibrated water temperature predictions compared with Scenario 3 and Figure 21 shows the residuals.

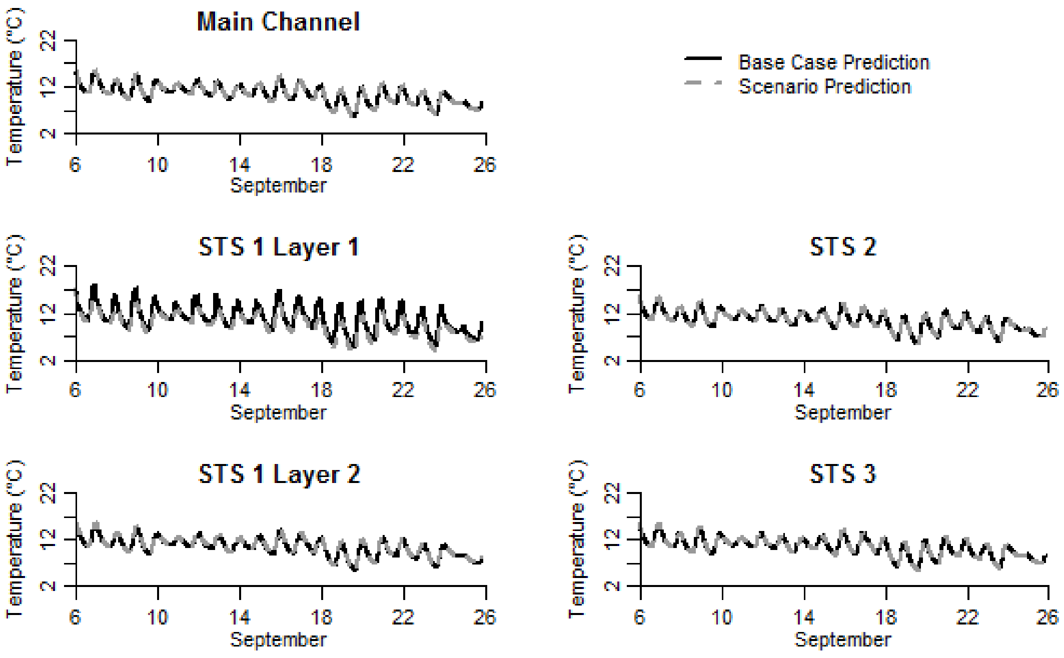

Figure 16: Scenario 1 temperature predictions compared against Base Case water temperature predictions from September 6 – 26, 2013 for the main channel, surface transient storage (STS) zones 1 layers 1 and 2, STS zone 2, and STS zone 3

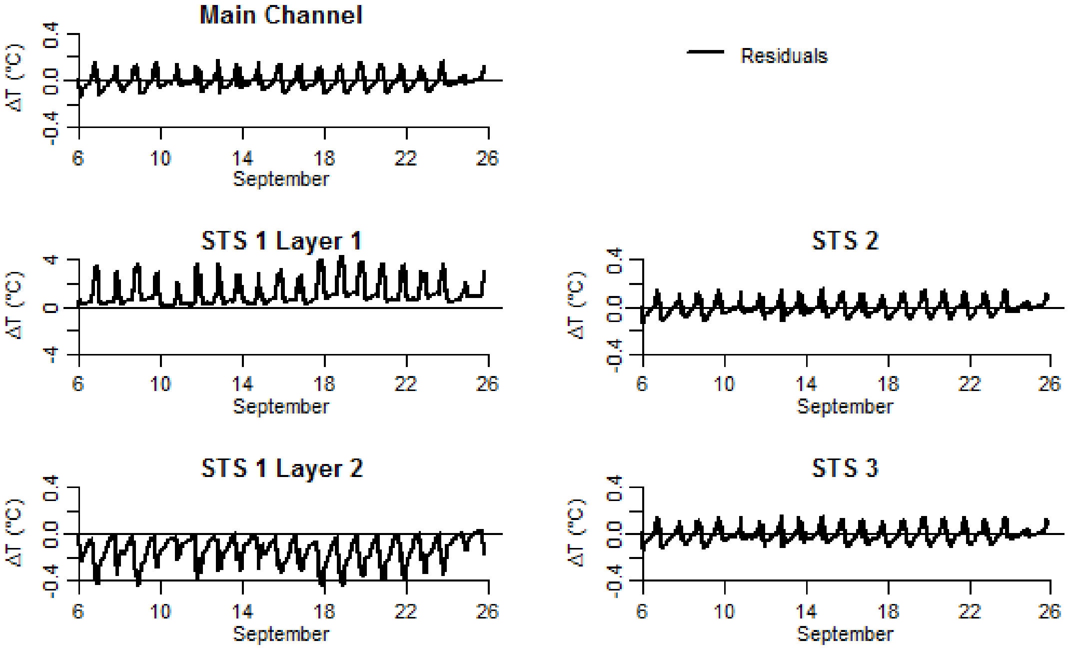

Figure 17: Residuals (ΔT) from Base Case vs. Scenario 1 water temperature predictions from September 6 – 26, 2013 for the main channel, surface transient storage (STS) zones

1 layers 1 and 2, STS zone 2, and STS zone 3. Note that the axes for STS 1 Layer 1 are an order of magnitude higher than the remaining zones.

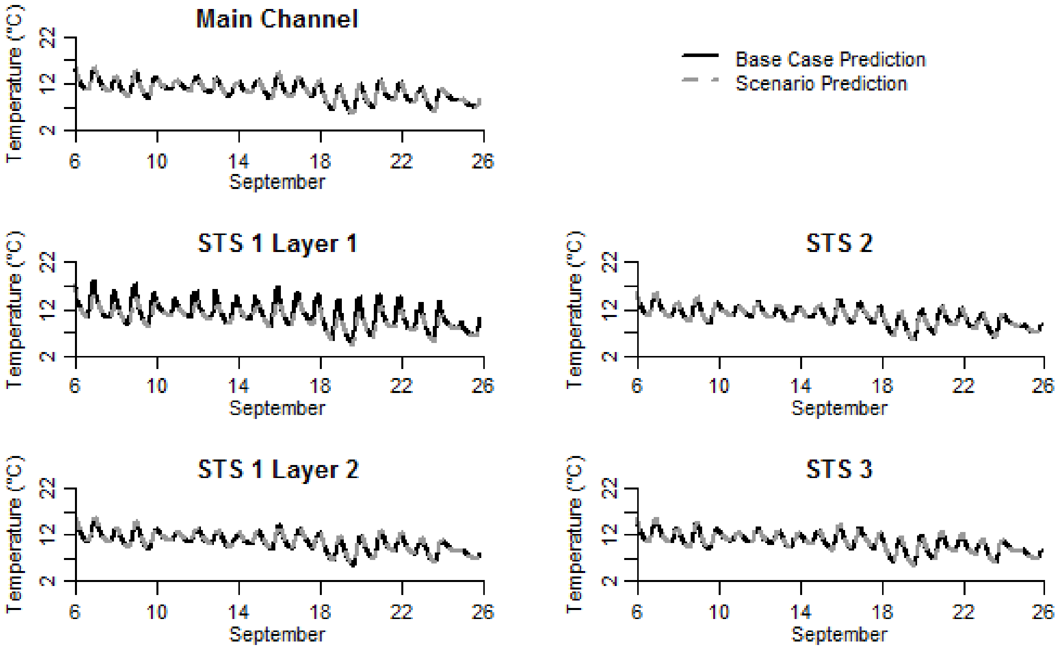

Figure 18: Scenario 2 temperature predictions compared against Base Case water temperature predictions from September 6 – 26, 2013 for the main channel, surface transient storage (STS) zones 1 layers 1 and 2, STS zone 2, and STS zone 3

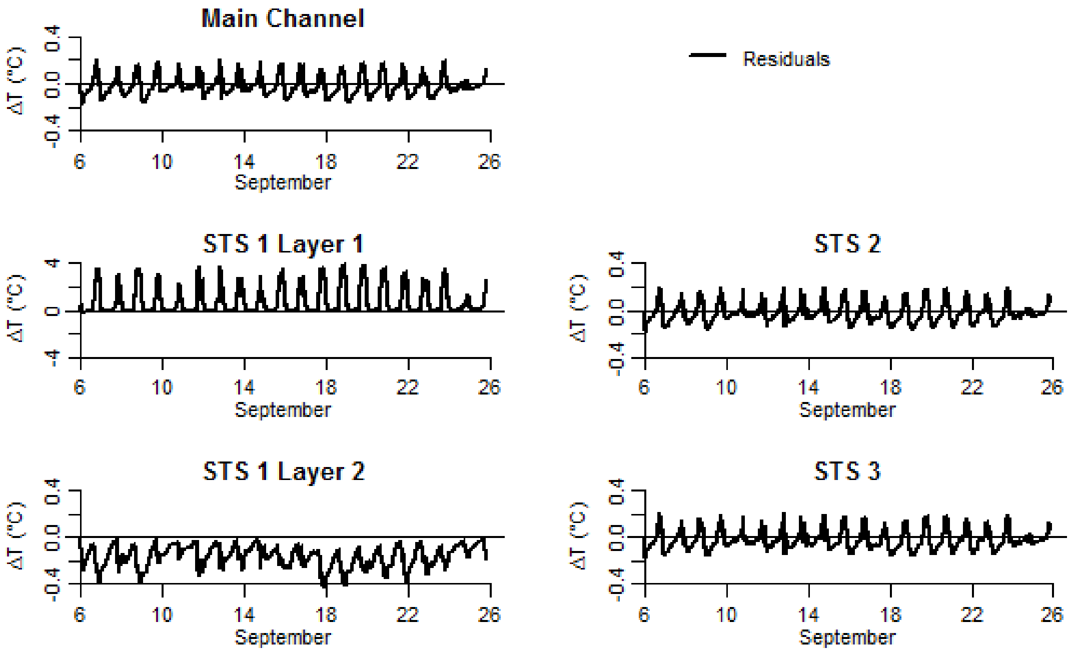

Figure 19: Residuals (ΔT) from Base Case vs. Scenario 2 water temperature predictions from September 6 – 26, 2013 for the main channel, surface transient storage (STS) zones 1 layers 1 and 2, STS zone 2, and STS zone 3. Note that the axes for STS 1 Layer 1 are an order of magnitude higher than the remaining zones.

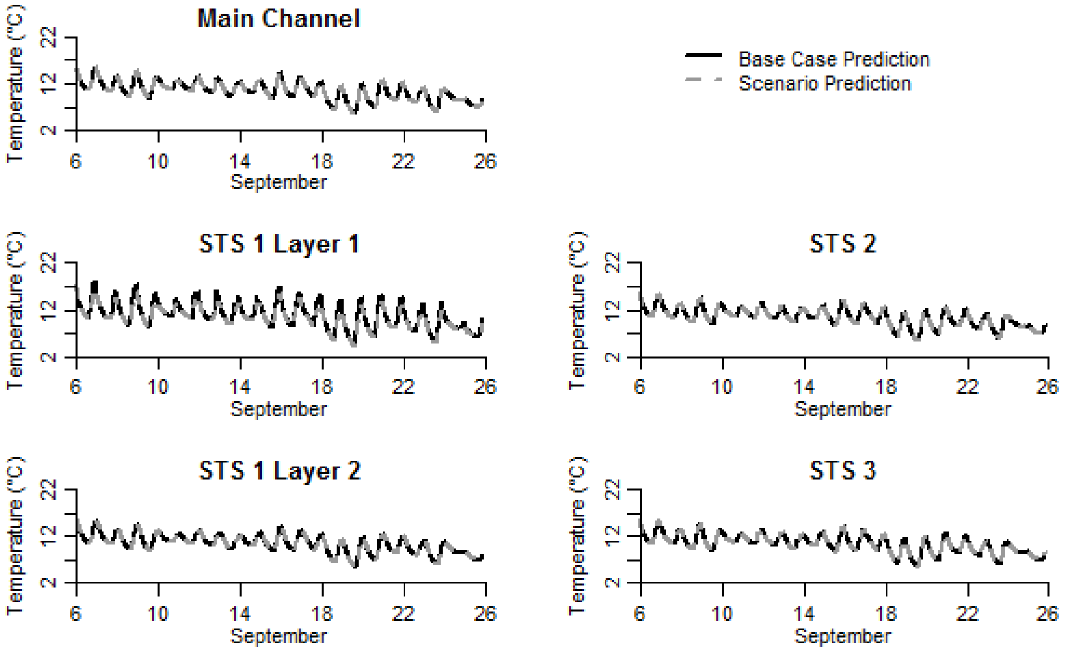

Figure 20: Scenario 3 temperature predictions compared against Base Case water temperature predictions from September 6 – 26, 2013 for the main channel, surface transient storage (STS) zones 1 layers 1 and 2, STS zone 2, and STS zone 3

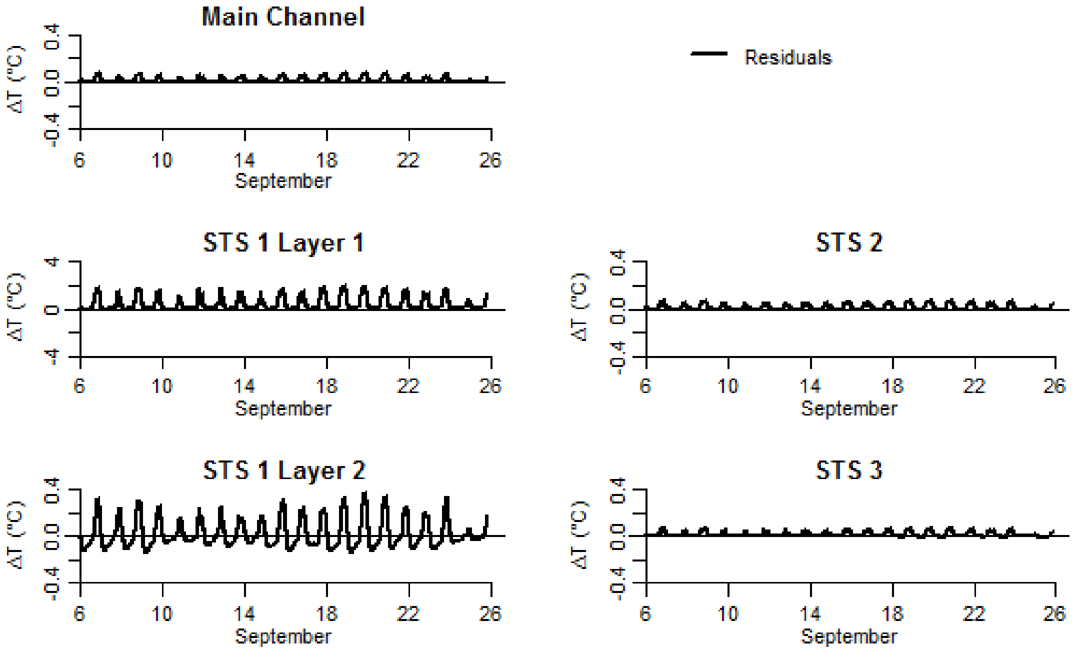

Figure 21: Residuals (ΔT) from Base Case vs. Scenario 3 water temperature predictions from September 6 – 26, 2013 for the main channel, surface transient storage (STS) zones 1 layers 1 and 2, STS zone 2, and STS zone 3. Note that the axes for STS 1 Layer 1 are an order of magnitude higher than the remaining zones.

In Scenario 3 the differences in temperature are within measurement error for the main channel and STS zones 2 and 3. STS zone 1 layer 1 experienced temperatures up to 2 °C cooler and STS zone 1 layer two experienced temperatures up to 0.4 °C cooler than the Base Case predictions.

Discussion

Based on the model calibration, we were able to simulate the thermal heterogeneity within the beaver pond with each zone’s predictions having RMSE values less than 1.2 (Table 3, main channel: 0.07, STS zone 1 layer 1: 1.14, STS zone 1 layer 2:

0.58, STS zone 2: 0.35, STS zone 3: 0.44). The ability to predict the temperatures of these generalized zones addresses our need to understand thermal heterogeneity at a coarse spatial scale. It can also be a useful tool in predicting the changes that can occur within the pond before changes to the “average” main channel temperature are detected [*Ebersole et al.*, 2003]. Further, it can an aid in identifying habitats that provide thermal refuges for fish [*Ebersole et al.*, 2003] and other aquatic organisms. We also found that we are able to predict the streambed sediment temperatures below all zones well for deeper sediments (RMSE values ranging 0.33 to 0.51 for 50 cm and 0.09 to 0.12 for 75 cm below the sediment-water interface as shown in Table E.1). The sediment temperature predictions appear to represent the observed data well for the sediment layers closest to the sediment-water interface below STS zone 1 based on the RMSE and visual inspection (RMSE of 0.42 at 5cm, 0.56 at 10 cm, and 0.57 at 25 cm below the sediment-water interface as shown in Table E.1) which has no solar radiation reaching the sediments due to the aquatic vegetation growth in that zone. On the other hand, the predictions for sediment temperatures beneath the main channel and STS zones 2 and 3 closest to the sediment-water interface were less accurate (RMSE values ranging 2.01 to 2.76 at 5 cm, 1.77 to 2.36 at 10 cm, and 1.42 to 1.85 at 25 cm below the sediment-water interface as found in Table E.1). These discrepancies are likely due to the simplified representation of the solar radiation sediment-water interactions at the respective interface. The potential complex convective (forced or natural) influences at this sediment water interface have not been accounted for within our current model equations. Further, the complex hydrodynamics within and around these zones influence measured STS zone behavior and violate our completely mixed assumption within this model.

While the model calibration resulted in good temperature predictions, the model corroboration provided mixed results where simulated temperatures were reasonable in some zones (Table 4, main channel RMSE: 0.13, STS zone 3 RMSE: 0.19), but poor in others (STS zones 1 and 2), which may in part be due to the fact that the meteorological data inputs were obtained from a weather station located approximately 22 miles away from the site (Figures H.1-4 in Appendix H). STS zone 1 had significantly under-predicted temperatures for both stratified layers (RMSE for layer 1: 3.51, layer 2: 2.42, Table 4). We believe that this is due in part to a difference in the amount of aquatic vegetation present in STS zone 1 between 2012 (corroboration) and 2013 (calibration) which was not accounted for within the model. Based on spot measurements made during the field campaigns, we found that the depth of the stratified layer in STS zone 1 was directly related to the height of the aquatic vegetation where the water above the vegetation layer was much warmer than that within and below the vegetation. Because we did not have measurements of the height of aquatic vegetation in 2012, the stratified layer depths were assumed the same as those measured in 2013. This coupled with off-site meteorological data that resulted in consistently lower solar radiation inputs (see Figure G.1) was not an accurate representation of the system and resulted in erroneous predictions. The model corroboration also under-predicted the temperatures found in STS zone 2 (RMSE of 1.23, Table 4). When segmenting the STS zones based on the data collected in 2012 (corroboration) it was found that a section of the pond between the main channel and STS zone 2 had temperatures slightly higher than the main channel and slightly lower than STS zone 2 which was not observed in 2013 (calibration). In order to correlate the main channel and STS zones between the calibration and corroboration this “transitional” section or zone was incorporated into the main channel zone for 2012 (corroboration). If this “transitional” zone was segmented apart from the main channel into its own STS zone it would have reduced the exchange between the main channel and STS zone 2 therefore limiting the influence of the cooler main channel temperatures on STS zone 2. *Gard* [1961], *Margolis et al.* [2001], and *Burchsted et al.* [2010] each found that the stream temperature effects resulting from beaver activity varied by season. This and these modeling results suggest that the thermal heterogeneity within the beaver pond will vary seasonally and the simplified approach applied here that assumes static and coarse model segmentation will likely be inadequate to accurately quantify the seasonal and flow-related variability in pond thermal heterogeneity. Depending on the required accuracy, a 2 or 3-D modeling approach would be necessary to capture some of these time and flow variable responses.

Considering the contribution of each of the heat fluxes influencing the temperature responses within beaver ponds can aid in identifying the characteristics influencing the thermal heterogeneity [*Brown*, 1969]. Each of the main channel and STS zones within the Curtis Creek beaver pond were dominated by the heat fluxes at the air-water interface and influences of streambed conduction and exchange between the zones were almost negligible, except in STS zone 1 layer 2 which had no contact with the atmosphere and was dominated by exchange between zones. Based on the contributions of each of the heat fluxes, the diurnal variations apparent in each of the temperature predictions are likely due to the influence of solar radiation. The magnitude of solar radiation influencing STS zone 1 layer 1 was found to be significantly greater in magnitude during the day than any of the other zones. The maximum magnitude of the solar radiation in STS zone 1 layer 1 is 2.1 times greater than in the main channel, 3.5 times greater than in STS zone 2, and 3.8 times greater than in STS zone 3. This is likely because all of the incoming solar radiation reaching STS zone 1 was absorbed in layer 1 in addition to it having less exchange with the main channel (Table 2, 2.8 x 10^7 cm^2 day^{-1}) and a larger surface area (124 m^2) than the other STS zones (Table 2, exchange for STS zone 2 and 3: 4.1 x 10^8 cm^2 day^{-1} and surface area for STS zone 2: 19.0 m^2 and STS zone 3: 20.1 m^2). This information regarding the dominance of each heat flux and how each is related to the characteristics promoting thermal heterogeneity within the beaver pond may prove to be useful in the management of streams, particularly thermally marginal streams [*Ebersole et al.*, 2003].

As beaver activity results in many physical changes to streams [*Naiman et al.*, 1986; *Shields et al.*, 1995; *Burchsted et al.*, 2010; *Ciechanowski et al.*, 2011], utilizing the model to run scenarios helps to quantify the effects that these alterations have on the thermally heterogeneous environment over time. All three scenarios applied to the model in this study resulted in insignificant temperature changes which were less than the sensor measurement accuracy (<0.2 °C) for the main channel and STS zones 2 and 3. STS zone 1 layer 2, on the other hand, had temperatures varying approximately 0.4 °C from the Base Case predictions and STS zone 1 layer 1 experienced temperature predictions that varied between 2 °C and 4 °C from the Base Case. This is a result of the characteristics specific to STS zone 1 which include having a large volume and surface area and little exchange with the main channel meaning slower-moving or more stagnant waters.

Since surface transient storage is enhanced in beaver ponds and transient storage directly affects the residence time of a solute (e.g., nutrients) within a system [*Jin et al.*, 2009], it would be of further interest to investigate the implications regarding the effect that beaver ponds have on solute transport. Solutes detained in transient storage zones have more time to undergo geochemical and biochemical processes as well as have more contact time with biogeochemically reactive sediments [*Jin et al.*, 2009]. Based on the scenario applications introduced in this study, STS zones having large volumes and surface areas as well as limited exchange with the main channel (e.g., STS zone 1) are the most influenced by alterations to the beaver pond and provide the greatest thermal diversity. This suggests that in order to have significant changes in thermal heterogeneity over time, large stagnant areas that are somewhat hydraulically disconnected from the main channel must be present. It is also likely that such areas would also have the greatest impact on solute fate and transport due to long residence times and generally higher temperatures and reaction rates.

The fact that insignificant changes to much of the beaver pond were predicted for the scenarios tested is not surprising given the short residence times of most zones and the small spatial scales covered by one beaver pond. *Majerova et al.* [manuscript in preparation, 2014] found that when measuring the temperature responses at the beaver dam scale within Curtis Creek, differences in temperatures above and below beaver ponds fell within the measurement accuracy of the sensors (± 0.2 °C). However, at the larger reach scales where multiple beaver ponds were present, the temperature differences increase by 38% which may be related to the increased residence time of the reach (89 minutes at the reach scale versus 36 minutes for the beaver pond) [*Majerova et al.*, manuscript in preparation, 2014]. This suggests that the bulk of the water moving through a beaver dam is minimally influenced by heat exchanges, consistent with our predictions. Further work should investigate the influence of many beaver dams and configurations on reach scale temperatures responses to determine the quantity and configurations of the beaver dams that may result in significant downstream temperature changes.

Conclusion

A process-based temperature model was developed to address the unique characteristics of beaver ponds with the capability of being adapted to any beaver pond site application. Data were collected for a site-specific application at a beaver pond located in Northern Utah which provided information regarding the spatial distribution and characteristics of different thermally heterogeneous zones and allowed for model scenarios to be tested.

The calibrated model generally produced temperature predictions that represented observed water temperatures; however, the sediment temperature predictions were not always representative of the observed data. Further investigation into representing processes associated with radiation penetration influences at the sediment-water interface is needed. Within the model corroboration, some of the thermally heterogeneous zones were simulated well; however, others were significantly under-predicted therefore introducing the need for a better understanding how the characteristics of thermal heterogeneity change during the different times of year and different life stages of the beaver dam.

Three scenarios were applied to the calibrated model to represent the physical changes to a stream over the lifespan of the beaver pond including initial impoundment formation, sediment deposition, aquatic vegetation growth, and riparian vegetation re-growth following beaver dam abandonment. Each scenario appeared to have little effect on the main channel and the two smaller STS zone temperatures; however, all scenarios had a significant effect on the temperatures within the STS zone containing a large amount of stagnant water and limited hydraulic connectivity to the main channel. These results suggest that in order to have a significant impact on the thermal heterogeneity within a beaver pond there must be larger STS zones with limited exchange with the flowing main channel water. Similarly, we expect that STS zones having large volumes of water and limited exchange with the main channel could have a significant effect on the fate and transport of solutes. Using this simplified model of these complex systems, we can begin to understand the spatial distribution of thermal heterogeneity by predicting the temperatures of different thermally heterogeneous zones and identifying the key factors influencing temperatures within beaver ponds. This information is instrumental to understanding the effect that beaver reintroduction will have on the thermal regime of a stream.

CHAPTER 3

DETERMINING THE FATE OF SOLAR RADIATION IN THE WATER COLUMN[2]

Abstract

Shortwave radiation is the primary driver of stream temperature for streams with limited shading, because it is often the most influential heat flux within stream energy budgets. Having an understanding of the fate of shortwave radiation in the water column is of particular importance when predicting the temperature of shallow, thermally stratified waters, where the attenuation of shortwave radiation is dependent on the water quality of each stratified layer. There is a need for methods to determine the fate of absolute broad-spectrum shortwave radiation in the water column to verify that we are representing its attenuation accurately when predicting stream temperature. Pyranometers designed for use in air having hemispherical glass domes and producing a flat spectral response have been used to measure the fate of broad-spectrum shortwave radiation in water, but have been shown to produce large errors due to immersion. Laboratory experiments were conducted using an LP02 pyranometer (Hukseflux, Delft, Netherlands) to determine immersion corrections and verify the cosine response of the sensor underwater. Since it was difficult to obtain a controlled light source that imitated the spectral response of the sun, two lamps each with a different spectral response were used. Despite the sensor's flat spectral response it was found that the immersion corrections

---

[2] Co-authored by Dr. Bethany Neilson, Dr. Bruce Bugbee, and Dr. Randy Martin

varied for each lamp in which the tungsten-halogen required an immersion coefficient that was approximately double that of the high-pressure sodium lamp (3.15 ± 0.42 and 1.53 ± 0.20, respectively) to correct the underwater measurements, therefore suggesting that immersion corrections are dependent on the spectral response of the light source. Additionally, the cosine response of the sensor underwater was found to be inaccurate suggesting that the LP02 pyranometer would produce large errors for *in situ* measurements when solar radiation is reaching the sensor at different angles throughout the day. These results indicate a need for further investigation into methods that can be used to correct pyranometers in order to measure the fate of broad-spectrum shortwave radiation in a natural water body.

Introduction

Solar or shortwave radiation (between 140 and 4000 nanometers in wavelength [*Meier et al.*, 2003]) is the most significant heat flux influencing the temperature in streams with limited shading [*Brown*, 1969; *Sinokrot & Stefan*, 1993; *Johnson*, 2004]. Understanding the fate of shortwave radiation in the water column is particularly important when predicting the temperature of thermally stratified waters where shortwave radiation can attenuate differently for different thermally stratified layers depending on the water quality of each layer [*Kirk*, 1988; *Merck & Neilson*, 2012]. Broad-spectrum shortwave radiation attenuation coefficients are a means to quantify the amount of solar radiation reaching different depths within the water column [*Fang & Stefan*, 1999; *Jin et al.*, 2000; *Merck et al.*, 2012a], but in-situ estimates are necessary to understand the influences of solar radiation within water columns and sediments of natural systems [e.g., *Neilson et al.*, 2010c; *Merck et al.*, 2012a].

There is minimal literature detailing methods necessary to determine attenuation coefficients for broad-spectrum shortwave radiation. *Neilson et al.* [2010c] measured broad-spectrum shortwave radiation at different depths within the water column using a pyranometer with a hemispherical glass dome with a flat spectral response to obtain spectrally averaged attenuation coefficients. While they were able to obtain attenuation coefficients, the relative fate of the solar radiation was predicted within the water column rather than using absolute readings. Such methods have been used due to complications with absolute measurements of shortwave radiation within the water column where pyranometers with hemispherical glass domes, designed for use in air produce large errors in readings when immersed in water [*Westlake*, 1965; *Kaiser*, 1976] and requires them to be calibrated for use underwater [*Roemer & Hoagland*, 1976; *Zibordi*, 2007].

Immersion Correction

The differences between air and water measurements are characterized by the difference in the index of refraction of air versus the index of refraction of water [*Roemer & Hoagland*, 1976; *Kaiser*, 1976; *Zibordi & Darecki*, 2006]. The index of refraction causes a change in the reflectance and transmittance of the irradiance reaching the detector, which affects the instrument measurement response [*Zibordi*, 2007] (Figure 22).

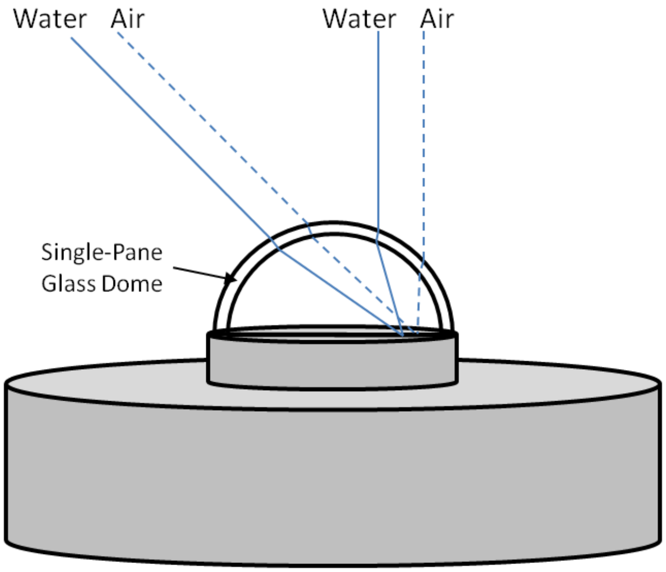

Figure 22: Figure based on *Kaiser* [1976] showing light ray paths traveling through water and through air after which it passes through the single-pane glass dome of the pyranometer into the air inside the dome until it reaches the sensor detector. The indices of refraction for air, water, and the glass dome are 1.00, 1.34, and 1.50, respectively [*Kaiser*, 1976].

It has been found that a submerged sensor has incident radiation backscattered into the water meaning a larger portion of the incoming radiation is diverted away from the sensor [*Roemer & Hoagland*, 1976; *Enshayan*, 1989]. While immersing the sensor in water results in a decrease in signal response, it should be noted that immersion errors may also result in an increase in response. The small refractive index differences between glass and water result in reduced reflection from the glass dome causing the sensor to have higher readings than when measuring radiation in air [*Enshayan*, 1989]. These differences caused by immersion, also known as the immersion effect, must be corrected for to account for the sensor's sensitivity changes and to measure absolute solar radiation under water [*Roemer & Hoagland*, 1976; *Kaiser*, 1976; *Zibordi & Darecki*, 2006].

Immersion coefficients, which are multiplication coefficients, are used to account for the immersion effect [*Zibordi et al.*, 2004; *Zibordi*, 2007]. The immersion coefficient must be applied to data recorded by sensors underwater at water depths greater than one diameter of the sensor collector [*Roemer & Hoagland*, 1976] and since they are specific for each model of sensor, it is important to correct each individual model of sensor [*Roemer & Hoagland*, 1976; *Zibordi et al.*, 2004]. Values for immersion coefficients have generally been found to be greater than one [*Zibordi et al.*, 2004] to correct for an overall reduction in irradiance measured by the instrument in water. These coefficients are determined experimentally in laboratories by taking measurements of shortwave radiation using the pyranometer at different water depths [*Mueller et al.*, 2003].

Cosine Response Verification

In addition to correcting for the immersion effect, it must also be verified that a pyranometer's cosine response does not have significant errors when used underwater. As described in many instrumentation textbooks, the cosine response is the radiation incident on a flat horizontal surface originating from a point source with a defined zenith position that has an intensity value proportional to the cosine of the zenith angle of incidence (Figure 23). To measure incoming radiation incident on the sensor plane for all angles relative to the normal, the pyranometer should follow a cosine function which ensures that the instrument correctly measures the radiation reaching the sensor without respect to the direction from which the light comes [*Mueller et al.*, 2003].

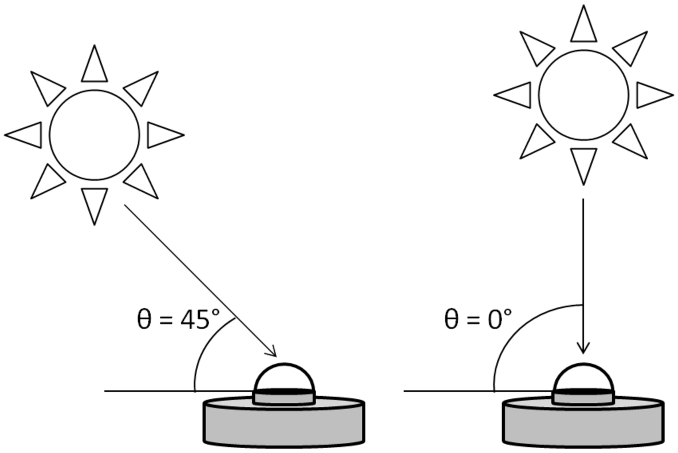

Figure 23: Visual description of the cosine law based on position of the sun with respect to a pyranometer

Zibordi [2007] states that the cosine error of a sensor is described by its normalized angular response, which is the response divided by the cosine of the angle of incidence and by the response at normal incidence. The angle of solar radiation varies with time of day, weather, and shading [*Westlake*, 1965] and the cosine error is largest at high angles and depends on wavelength, sun zenith, and atmospheric optical conditions [*Zibordi*, 2007]. Within the context of water, surface reflection, refraction, and scattering also cause the angle of incoming solar radiation to vary with underwater depth [*Westlake*, 1965; *Roemer & Hoagland*, 1976] making it critical to verify whether the pyranometer has the correct cosine response for application within the water column.

To this end, this paper 1) evaluates the use of pyranometers with a hemispherical glass dome having a flat spectral response for obtaining broad spectrum shortwave radiation attenuation coefficients; 2) determines whether immersion correction methods can be applied to pyranometers with a hemispherical glass dome to obtain absolute shortwave radiation measurements underwater; 3) determines whether imitation light sources are adequate for determining immersion corrections in a laboratory setting; and 4) determines the need to refine cosine response corrections for use of hemispherical glass pyranometers under water.

Methods

In order to obtain the immersion corrections for and verify the cosine response of a pyranometer having a hemispherical glass dome and flat spectral response, an LP02 pyranometer (Hukseflux Thermal Sensors, Delft, Netherlands) was attached to a CR1000 data logger (Campbell Scientific, Logan, Utah) and programmed to sample and record broad spectrum shortwave radiation at one-second intervals.

Immersion Correction Approach

The laboratory experiment and set-up to determine immersion corrections are adapted from the methods from *Mueller et al.* [2003]. The LP02 pyranometer was placed in a large bucket of water with the sensor level and facing upward and a circular baffle was placed over the sensor to reduce stray light (Figure 24). All equipment used in the set-up this experiment, excepting the sensor and light source, were painted a matte black to minimize the amount of reflection that could negatively affect the readings.

Since it was difficult to identify a light source emitting broad-spectrum shortwave radiation that could be used in a controlled laboratory setting, two 400-Watt tungsten-halogen lamps and one 1000-Watt high-pressure sodium lamp were used as light sources for these experiments. Both lamps were used in order to observe whether the immersion effect would be similar for different wavelengths of light emitted since halogen lamps tend to emit more near-infrared light than visible light and whereas sodium lamps emit primarily visible light (Figure 25).

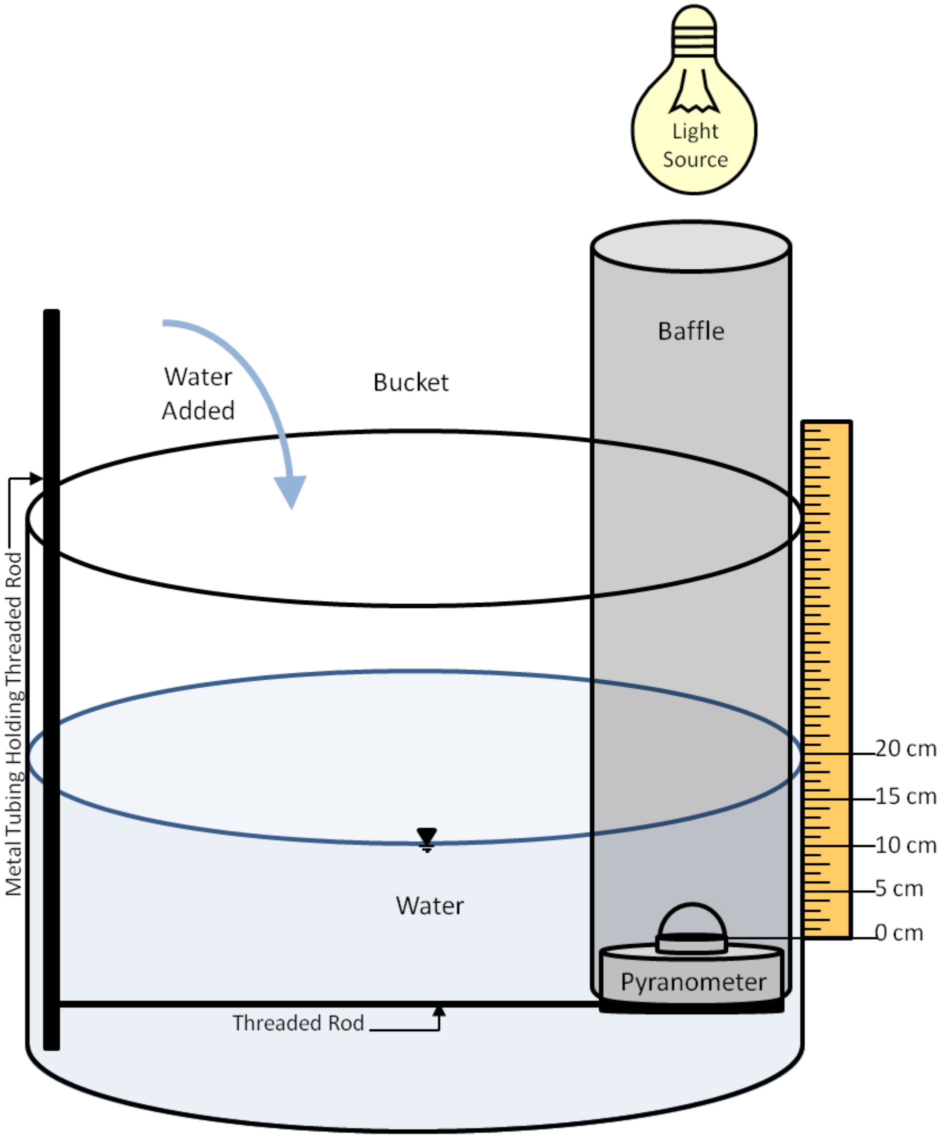

Figure 24: Diagram of the experimental set-up used for the immersion correction experiments in which a pyranometer was suspended in a bucket of water with a baffle used to reduce stray light. Water was added at from the top of the bucket by 5 centimeter increments while shortwave radiation measurements from the light source were recorded

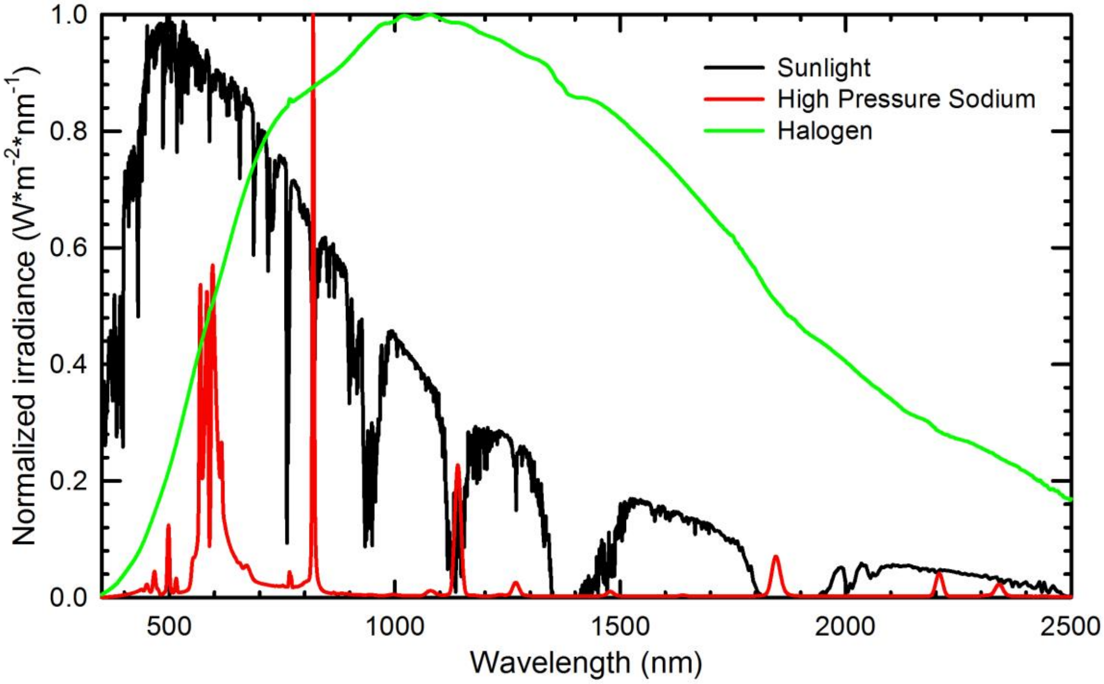

Figure 25: Spectral responses for sunlight, the high-pressure sodium lamp, and the tungsten-halogen lamp measured with a spectroradiometer (ASD Inc., Boulder, CO). The measurements are normalized to the maximum measurement for each light source.

The distance from the sensor to the light source was measured and an initial reading was taken in air prior to the addition of water to the bucket. Following the initial air reading, water was added from the top of the bucket to barely cover the glass dome above the sensor. The water level was then increased by five centimeter increments up to approximately 20 centimeters while the water depth and sensor readings were recorded. Using these measurements, the immersion coefficient could be calculated using Equation 17 [*Zibordi & Darecki*, 2006]:

Equation 17

$$I_f = \frac{J_{sn}(0^+)}{J_{sn}(0^-)} t_{wa}$$

where I_f is the immersion coefficient, $J_{sn}(0^+)$ is the radiation measurement made in air, $J_{sn}(0^-)$ is the radiation measurement made underwater, and t_{wa} is the transmittance of the air-water interface, which is computed from the Fresnel reflectance for a vertically incident light beam (assumed to be 2% based on *Roemer & Hoagland* [1976]). To determine $J_{sn}(0^-)$ while accounting for the attenuation of light with increasing water depth, a broad-spectrum shortwave radiation attenuation coefficient for the water was determined using Equation 9. Example calculations for determining the immersion coefficient are shown in Appendix I.

Cosine Response Verification

To verify the cosine response, methods adapted from those suggested by *Kaiser* (1976), *Mueller et al.* (2003), and *Zibordi* (2007) were used. The LP02 pyranometer was suspended in a bucket of water while on a platform connected to a threaded rod which allowed the instrument to rotate about the axis through the horizontal center of the sensor (Figure 26). A baffle was added to reduce stray light and the tungsten-halogen lamp was used with the distance from the lamp to the sensor measured. Again, all equipment used in the set-up of this experiment, excepting the sensor and light source, were painted a matte black to minimize the amount of reflection that could negatively affect the readings.

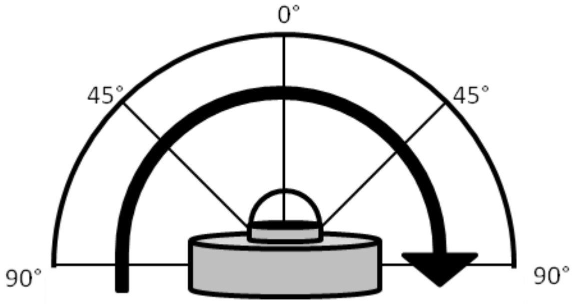

Figure 26: A diagram showing the rotation of the pyranometer used in the cosine response verification experiment

Water was added to the bucket until the water depth was approximately two centimeters above the sensor. A measurement at the 0° (incident) rotation was recorded after which the pyranometer was rotated at 5° angle increments to the left and to the right of the incident. The cosine response is calculated using Equation 18 [*Mueller et al.*, 2003]:

Equation 18

$$\frac{J_{sn}(\theta)}{J_{sn}(0°)} = \cos(\theta)$$

where $J_{sn}(0°)$ is the sensor response at 0° rotation, $J_{sn}(\theta)$ is the sensor response at θ degrees from the incident and the ratio of these values should be equal to $\cos(\theta)$. This process was later repeated in air to compare the measured cosine response to the theoretical expected cosine response. Example calculations for determining the cosine response are shown in Appendix I.

Results

Immersion Coefficient Results

The broad-spectrum shortwave radiation readings for the LP02 pyranometer under both the tungsten-halogen and high-pressure sodium lamps normalized to the initial reading taken in air are shown in Figure 27.

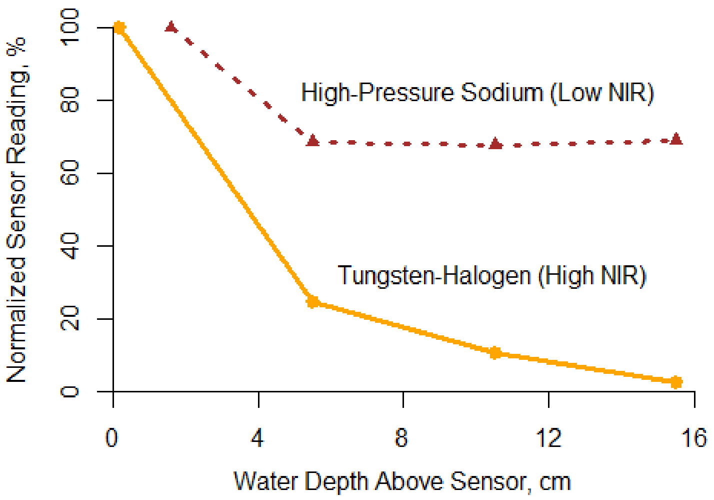

Figure 27: Shortwave radiation measurements for the LP02 pyranometer submersed in water at depths of approximately 0, 5, 10, and 15 centimeters above the sensor while using the high-pressure sodium lamp having a lower emission of near infrared wavelengths (NIR) (dotted) and tungsten- halogen lamp having a higher emission of NIR wavelengths (solid) as the light source.

Based on the shortwave radiation measurements taken beneath both lamps it is evident that the readings decreased with depth; however, the high-pressure sodium lamp appeared to decrease with depth at a faster rate. Additionally, the shortwave radiation readings for the tungsten-halogen lamp ranged between approximately 70 – 100% of air measurement and the high-pressure sodium readings ranged from 0 – 100% of the air measurement. The immersion coefficients that were calculated based on these shortwave radiation measurements beneath each lamp (Table 5) also illustrate the differences between light sources.

Table 5: Immersion factors ± the standard deviation of the data measured under both the tungsten-halogen and high-pressure sodium lamps. The standard deviation is associated with the variability between the readings taken at different water depths while accounting for attenuation of shortwave radiation through the water column.

Light Source	Immersion Coefficient
Tungsten-Halogen Lamp	3.15 ± 0.42
High-Pressure Sodium Lamp	1.53 ± 0.20

These immersion coefficients produced for the LP02 pyranometer varied significantly with the tungsten-halogen lamp having approximately double the immersion coefficient calculated for the high-pressure sodium lamp.

Cosine Response Verification Results

The results for the cosine response verification experiment (Figure 28) are shown with the theoretical or expected cosine response curve, the cosine response for measurements taken in air, and the cosine response for measurements taken in water normalized to the measurement taken from the 0° incident position.

The shortwave radiation measurements taken in air appear to generally follow the expected cosine response curve. The measurements taken in water, however, deviate significantly from and initially decrease at a faster rate than the theoretical cosine response curve as the sensor is rotated farther away from the incident. The error associated with both the air and water measurements was then compared to the theoretical cosine response curve (Figure 29).

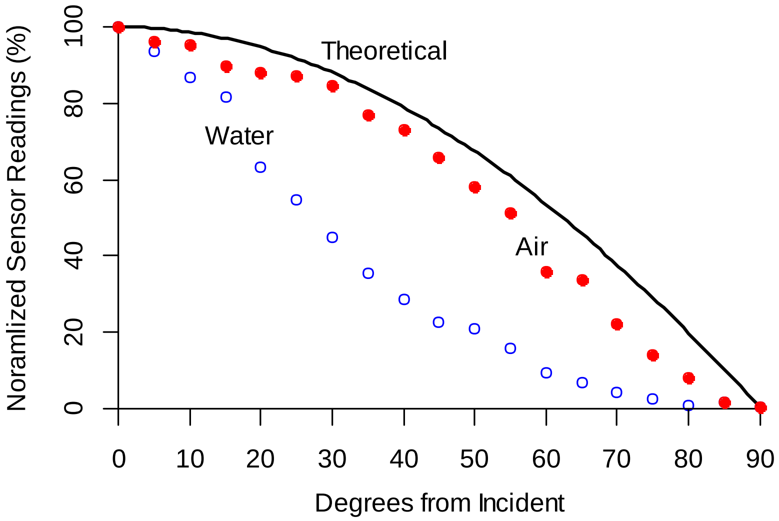

Figure 28: Shortwave radiation measurements for the LP02 pyranometer rotated around the horizontal axis at 5° increments from the incident while using a halogen lamp as the light source while in air (solid circles) and submersed in water (open circles) compared to the expected theoretical response (solid line)

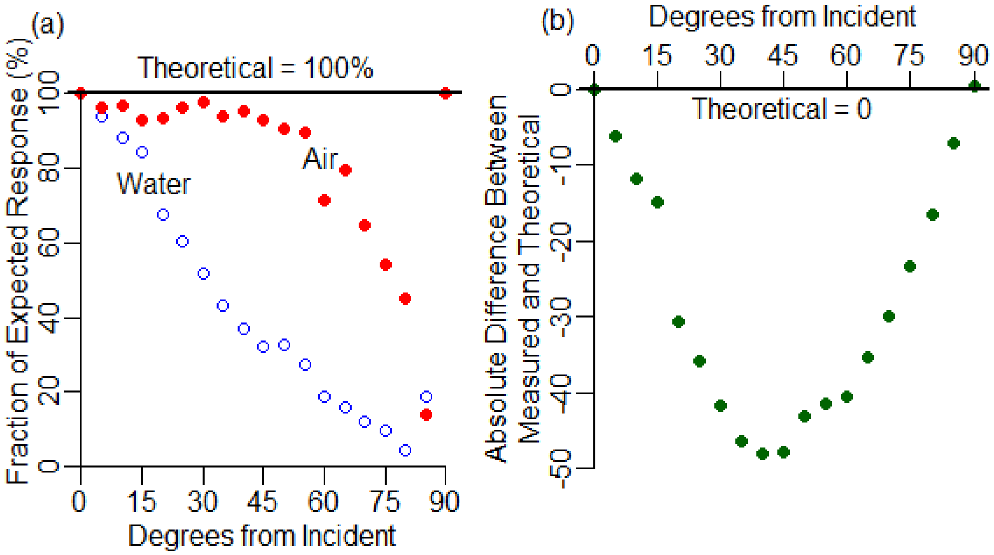

Figure 29: (a) The percent of the expected theoretical response for each sensor reading associated with the cosine response in air (solid circles) and submersed in water (open circles) compared to the theoretical response (solid line). (b) The residuals associated with the water measurements determined from subtracting observed sensor response from the expected theoretical response

The shortwave radiation measurements taken in air produce results encompassing at least 90% of the true response for angles 0 to 50°. After 50° the measurements involve much larger error capturing between 15 – 89% of the true response except the reading taken at 90° in which the sensor did not measure any shortwave radiation which was expected. The readings taken in water, however, maintained 90% of the true response for the measurements taken at 0° and 5° after which the measurements continued to deviate from the true response between 10° and 90°.

Discussion and Conclusions

There is a need to be able to collect broad-spectrum shortwave radiation data within streams in order to understand the fate of solar radiation within the water column, particularly within stratified systems [*Merck & Neilson*, 2012]. Broad-spectrum shortwave radiation attenuation coefficients are used to estimate the amount of solar radiation penetrating the water column [*Fang & Stefan*, 1999; *Jin et al.*, 2000; *Merck et al.*, 2012a], but there is currently a minimal amount of literature providing methods for obtaining and verifying these attenuation coefficients. Pyranometers having hemi-spherical glass domes and producing a flat spectral response are capable of measuring broad-spectrum shortwave radiation, but have been shown to produce large immersion errors when used underwater [*Kaiser*, 1976]. The experiments in this study confirmed the large errors in pyranometer readings due to immersion.

The sensor readings under the two different lamp types produced significantly different immersion factors for the black-body pyranometers (Table 5) which is likely due to the fact that each lamp emits light from different wavelength ranges. This is of particular concern, however, when using the LP02 pyranometer for measuring shortwave radiation in sunlight, because the immersion factor determined via imitation light sources in laboratory experiments may not apply to the pyranometer when it is measuring solar radiation. This idea challenges the notion that immersion coefficients should be determined experimentally in a laboratory [*Mueller et al.*, 2003] or suggests the need for a light source that better represents the spectral response of sunlight when the coefficients will be applied to measurements taken in natural sunlight.

When investigating the cosine response of the sensor it appeared that the cosine error increased with increasing angle consistent with what has been found in *Zibordi* [2007]. When evaluating the cosine response of the pyranometer underwater it was found that the measurements significantly underrepresented the amount of shortwave radiation that should be reaching the sensor at almost all angles. Because the angle of solar radiation varies with time of day, weather, and shading [*Westlake*, 1965], having an incorrect cosine response will impact the accuracy of the sensor reading [*Mueller et al.*, 2003] particularly when the sun is not directly incident to the sensor. Another aspect not accounted for in the experiment is the influence of the scattering of solar radiation within the water column. Since measurements in situ will generally be taken without a baffle to reduce stray light, this is another point of concern that may influence the accuracy of the sensor's cosine response.

It is evident from the immersion correction results that there is a need for an effective method to obtain immersion coefficients that can be applied to pyranometers to measure solar radiation within streams. Additionally, the cosine response of the LP02 pyranometer needs to be corrected prior to making underwater solar radiation measurements when the sun is not directly incident to the sensor. Regardless, these results provide a foundation for further investigation into better understanding the effects of immersion on shortwave radiation measurements in an effort to understand the fate of solar radiation within surface water bodies.

CHAPTER 4

CONCLUSION

A process-based temperature model was developed to address the unique characteristics of beaver ponds with the goal to gain insight into the impacts that beaver can have on stream temperature. Data were collected for a site-specific application of the model to a beaver pond located in Northern Utah which provided information regarding the characteristics of the beaver pond and enabled the testing of model scenarios. The calibrated model simulated the observed temperatures well; however, it was not always able to predict all of the streambed sediment temperatures accurately. The discrepancies suggest the need for further investigations about the processes related to shortwave radiation penetration at the sediment-water interface and how these should be incorporated into the model.

Three scenarios were applied to the calibrated model to represent the stream alterations that come as a result of beaver activity to investigate the associated effects on temperature. Each scenario showed little effect on the main channel and two smaller STS zone temperatures, notwithstanding three of the scenarios had a significant impact on the temperatures of the STS zone having a larger volume of stagnant water and limited exchange with the main channel. These results denote that in order to have a significant impact on the thermal heterogeneity in beaver ponds, larger STS zones with limited hydraulic connectivity with the flowing main channel waters must be present. Using a simplified approach to model the complex beaver pond system, we can begin to understand the spatial distribution of thermal heterogeneity and identify the key factors influencing temperatures within beaver ponds which will be particularly useful in determining the effects on temperature related to the reintroduction of beaver to streams.

The second objective of this research was to investigate methods for measuring absolute broad-spectrum shortwave radiation within streams to verify that we are accurately predicting the fate of solar radiation within stream temperature models. Underwater broad-spectrum shortwave radiation measurements were recorded using a pyranometer having a hemispherical glass dome and a flat spectral response. Two different lamps each emitting light from different wavelength ranges were also used to evaluate the use of imitation light for immersion correction determination. Each lamp produced a different immersion coefficient which introduces questions regarding the use of laboratory-determined immersion coefficients for application in streams with the sun as the light source. Furthermore, the underwater cosine response of the sensor produced large errors in readings in which the amount of shortwave radiation reaching the sensor was significantly underrepresented. Because the angle of solar radiation varies, a pyranometer having an incorrect cosine response underwater will be inaccurate for measurements taken in streams in sunlight.

Based on these results, it is apparent that there is still a need for an effective method to understand the fate of broad-spectrum shortwave radiation in surface water bodies which provide opportunities to improve our ability to characterize the processes related to solar radiation within process-based temperature models. This will improve our ability to more accurately model temperatures of streams impacted by beaver and make it possible to further evaluate the implications for stream temperature associated with using beaver as a stream restoration tool.

CHAPTER 5

ENGINEERING SIGNIFICANCE

The aforementioned research advances the field of environmental engineering twofold. First, we have developed a process-based temperature model which addresses the characteristics unique to beaver ponds to predict the spatial distribution of temperature and the mechanisms influencing the thermal heterogeneity within beaver ponds. Second, it has introduced insight regarding methods for measuring broad-spectrum shortwave radiation within the water column which is useful in verifying the fate of shortwave radiation within the water column as estimated by attenuation coefficients.

The process-based temperature model concept provides a simplified representation of the thermal regime within beaver ponds. Scenarios depicting alterations that occur to a stream as a result of beaver activity were applied to determine the associated effect on temperature. It was found that significant changes in temperature only occurred for a surface transient storage zone having a large, stagnant volume of water and limited hydraulic connectivity to the flowing main channel waters. This is important, because beaver ponds having surface transient storage zones with these characteristics will have a higher probability of experiencing significant thermal heterogeneity than streams lacking these areas. Based on this information, stream restoration efforts using beaver should focus on creating these types of areas if increased thermal heterogeneity is desired.

When investigating methods for measuring the fate of shortwave radiation in the water column it was confirmed that pyranometers having hemispherical glass domes designed for use in air must be corrected for underwater measurements [*Roemer & Hoagland*, 1976; *Zibordi*, 2007]. Immersion coefficients determined in laboratory experiments were found to vary with the spectral response of the light source meaning that immersion coefficients determined in a laboratory under imitation light may not provide accurate immersion corrections for measuring broad-spectrum shortwave radiation within streams. Additionally, the cosine correction of the pyranometer in this experiment was found to produce erroneous readings underwater therefore requiring further investigation into correcting the underwater cosine response. Therefore, future research should focus on methods to accurately measure broad-spectrum shortwave radiation underwater so as to understand shortwave radiation influences on surface water and predict thermal heterogeneity well within simplified and higher-dimensional stream temperature models.

REFERENCES

Albert, S., and T. Trimble (2000), Beavers are partners in riparian restoration on the Zuni Indian Reservation, *Ecol Restor, 18*(2), 87-92.

Arscott, D. B., K. Tockner, and J. Ward (2001), Thermal heterogeneity along a braided floodplain river (Tagliamento River, northeastern Italy), *Canadian J of Fish and Aquatic Sci*, *58*(12), 2359-2373.

Barrett, K. R. (1999), Ecological engineering in water resources: The benefits of collaborating with nature, *Water Internat*, *24*(3), 182-188.

Belmont, P., D. P. Morris, F. J. Pazzaglia, and S. C. Peters (2009), Penetration of ultraviolet radiation in streams of eastern Pennsylvania: Topographic controls and the role of suspended particulates, *Aquatic Sci*, *71*(2), 189-201.

Bencala, K. E., and R. A. Walters (1983), Simulation of Solute Transport in a Mountain Pool-and-Riffle Stream - a Transient Storage Model, *Water Resour Res*, *19*(3), 718-724.

Beschta, R. L., R. E. Bilby, G. W. Brown, L. B. Holtby, and T. D. Hofstra (1987), Stream temperature and aquatic habitat: fisheries and forestry interactions, *Streamside Manag: Forestry and Fishery Interactns, 57*, 191-232.

Billman, E. J., J. D. Kreitzer, J. C. Creighton, E. Habit, B. McMillan, and M. C. Belk (2013), Habitat enhancement and native fish conservation: can enhancement of channel complexity promote the coexistence of native and introduced fishes?, *Environ Biol of Fishes*, *96*(4), 555-566.

Briggs, M. A., L. K. Lautz, J. M. McKenzie, R. P. Gordon, and D. K. Hare (2012), Using high-resolution distributed temperature sensing to quantify spatial and temporal variability in vertical hyporheic flux, *Water Resour Res*, *48*(2).

Brown, G. W. (1969), Predicting temperatures of small streams, *Water Resour Res, 5*(1), 68-75.

Burchsted, D., M. Daniels, R. Thorson, and J. Vokoun (2010), The river discontinuum: applying beaver modifications to baseline conditions for restoration of forested headwaters, *BioScience, 60*(11), 908-922.

Caissie, D., N. El-Jabi, and M. G. Satish (2001), Modelling of maximum daily water temperatures in a small stream using air temperatures, *J of Hydrol*, *251*(1), 14-28.

Chapra, S. C. (1997), Surface water-quality modeling, *Mcgraw-hill Series In Water Resources And Environmental Engineering*, Waveland Press, Long Grove, Ill.

Ciechanowski, M., W. Kubic, A. Rynkiewicz, and A. Zwolicki (2011), Reintroduction of beavers Castor fiber may improve habitat quality for vespertilionid bats foraging in small river valleys, *Euro J of Wildlife Res, 57*(4), 737-747.

Danehy, R. J., C. G. Colson, K. B. Parrett, and S. D. Duke (2005), Patterns and sources of thermal heterogeneity in small mountain streams within a forested setting, *Forest Ecol and Manag, 208*(1), 287-302.

Diamond, S. A., P. C. Trenham, M. J. Adams, B. R. Hossack, R. A. Knapp, S. L. Stark, D. Bradford, P. S. Corn, K. Czarnowski, and P. D. Brooks (2005), Estimated ultraviolet radiation doses in wetlands in six national parks, *Ecosystems, 8*(5), 462-477.

Ebersole, J. L., W. J. Liss, and C. A. Frissell (2003), Thermal heterogeneity, stream channel morphology, and salmonid abundance in northeastern Oregon streams, *Canadian J of Fisheries and Aquatic Sci*, *60*(10), 1266-1280.

Enshayan, K. (1989), Measurement of solar radiation transmission in solar ponds, Ohio State University, Department of Food, Agricultural, and Biological Engineering.

Fang, X., and H. G. Stefan (1999), Projections of climate change effects on water temperature characteristics of small lakes in the contiguous US, *Climatic Change, 42*(2), 377-412.

Frost, P. C., J. H. Larson, L. E. Kinsman, G. A. Lamberti, and S. D. Bridgham (2005), Attenuation of ultraviolet radiation in streams of northern Michigan, *J of the N Amer Benth Society, 24*(2), 246-255.

Fuller, M. R., and B. L. Peckarsky (2011), Ecosystem engineering by beavers affects mayfly life histories, *Freshwater Bio, 56*(5), 969-979.

Gard, R. (1961), Effects of beaver on trout in Sagehen Creek, California, *The J of Wildlife Manag*, 221-242.

Jin, K.-R., J. H. Hamrick, and T. Tisdale (2000), Application of three-dimensional hydrodynamic model for Lake Okeechobee, *J of Hydraul Eng*, *126*(10), 758-771.

Jin, L., D. I. Siegel, L. K. Lautz, and M. H. Otz (2009), Transient storage and downstream solute transport in nested stream reaches affected by beaver dams, *Hydrol Processes, 23*(17), 2438-2449.

Johnson, S. L. (2004), Factors influencing stream temperatures in small streams: substrate effects and a shading experiment, *Canadian J of Fisheries and Aquatic Sci*, *61*(6), 913-923.

Kaiser, J. A. (1976), The use of pyranometers for underwater total radiant energy flux measurements, paper presented at Deep Sea Research and Oceanographic Abstracts, Elsevier.

Kirk, J. T. (1988), Solar heating of water bodies as influenced by their inherent optical properties, *J of Geophys Res: Atmos (1984–2012)*, *93*(D9), 10897-10908.

Laurion, I., M. Ventura, J. Catalan, R. Psenner, and R. Sommaruga (2000), Attenuation of ultraviolet radiation in mountain lakes: Factors controlling the among-and within-lake variability, *Limnology and Oceanography*, *45*(6), 1274-1288.

Loheide, S. P., and S. M. Gorelick (2006), Quantifying stream-aquifer interactions through the analysis of remotely sensed thermographic profiles and in situ temperature histories, *Environ Sci & Tech*, *40*(10), 3336-3341.

Margolis, B. E., R. L. Raesly, and D. L. Shumway (2001), The effects of beaver-created wetlands on the benthic macroinvertebrate assemblages of two Appalachian streams, *Wetlands*, *21*(4), 554-563.

McKinstry, M. C., P. Caffrey, and S. H. Anderson (2001), The Importance of Beaver to Wetland Habitats and Waterfowl in Wyoming, *J of the Amer Water Resour Assoc*, *37*, 1571-1577.

Meier, W., C. Bonjour, A. Wüest, and P. Reichert (2003), Modeling the effect of water diversion on the temperature of mountain streams, *J of Environ Eng*, *129*(8), 755-764.

Merck, M. F., and B. T. Neilson (2012), Modelling in-pool temperature variability in a beaded arctic stream, *Hydrol Processes*, *26*(25), 3921-3933.

Merck, M. F., B. T. Neilson, R. M. Cory, and G. W. Kling (2012a), Variability of in-stream and riparian storage in a beaded arctic stream, *Hydrol Processes*, *26*(19), 2938-2950.

Mueller, J. L., C. Pietras, S. B. Hooker, R. W. Austin, M. Miller, K. D. Knobelspiesse, R. Frouin, B. Holben, and K. Voss (2003), Ocean optics protocols for satellite ocean color sensor validation, revision 4, volume ii: Instrument specifications, characterization, and calibration, edited by N. A. a. S. Admin, pp. 26-31, Goddard Space Flight Center, Greenbelt, Md.

Naiman, R. J., J. M. Melillo, and J. E. Hobbie (1986), Ecosystem alteration of boreal forest streams by beaver (Castor canadensis), *Ecology*, *67*(5), 1254-1269.

Naiman, R. J., C. A. Johnston, and J. C. Kelley (1988), Alteration of North American streams by beaver, *BioScience*, 753-762.

Neilson, B. T. (2006), Dynamic stream temperature modeling: understanding the causes and effects of temperature impairments and uncertainty predictions, Utah State University, Department of Civil and Environmental Engineering.

Neilson, B. T., S. Chapra, D. Stevens, and C. Bandaragoda (2010a), Two-zone transient storage modeling using temperature and solute data with multiobjective calibration: 1. Temperature, *Water Resour Res*, *46*(12), W12520.

Neilson, B. T., D. Stevens, S. Chapra, and C. Bandaragoda (2010b), Two-zone transient storage modeling using temperature and solute data with multiobjective calibration: 2. Temperature and solute, *Water Resour Res*, *46*(12), W12521.

Neilson, B. T., C. E. Hatch, H. Ban, and S. W. Tyler (2010c), Solar radiative heating of fiber-optic cables used to monitor temperatures in water, *Water Resour Res*, *46*(8), W08540.

Pollock, M. M., T. J. Beechie, and C. E. Jordan (2007), Geomorphic changes upstream of beaver dams in Bridge Creek, an incised stream channel in the interior Columbia River basin, eastern Oregon, *Earth Surf Processes and Landforms*, *32*(8), 1174-1185.

Pollock, M. M., G. R. Pess, T. J. Beechie, and D. R. Montgomery (2004), The importance of beaver ponds to coho salmon production in the Stillaguamish River basin, Washington, USA, *N Amer J of Fisheries Manag*, *24*(3), 749-760.

Roemer, S. C., and K. D. Hoagland (1976), Immersion effect and cosine collecting properties of Li-cor underwater sensors, edited, pp. 1-11, School of Life Sciences, University of Nebraska, Lincoln, Neb.

Schmadel, N. M., B. T. Neilson, and D. K. Stevens (2010), Approaches to estimate uncertainty in longitudinal channel water balances, *J of Hydrol*, *394*(3), 357-369.

Schmadel, N. M., B. T. Neilson, and T. Kasahara (2013), Deducing the spatial variability of exchange within a longitudinal channel water balance, *Hydrol Processes*.

Shields, F., S. Knight, and C. Cooper (1995), Incised stream physical habitat restoration with stone weirs, *Regulated Rivers: Res & Manag*, *10*(2-4), 181-198.

Sinokrot, B. A., and H. G. Stefan (1993), Stream temperature dynamics: measurements and modeling, *Water Resour Res*, *29*(7), 2299-2312.

Snodgrass, J. W., and G. K. Meffe (1998), Influence of beavers on stream fish assemblages: effects of pond age and watershed position, *Ecology*, *79*(3), 928-942.

Stevens, M., G. Fenchel, and C. Hoag (2003), *Plant Guide: Coyote Willow*, prepared by U. S. D. o. Agriculture and N. R. C. Service, Greensboro, NC.

Torgersen, C. E., D. M. Price, H. W. Li, and B. A. McIntosh (1999), Multiscale thermal refugia and stream habitat associations of chinook salmon in northeastern Oregon, *Ecol App*, *9*(1), 301-319.

Velinsky, D. J., K. L. Bushaw-Newton, D. A. Kreeger, and T. E. Johnson (2006), Effects of small dam removal on stream chemistry in southeastern Pennsylvania, *J of the N Amer Benth Society*, *25*(3), 569-582.

Webb, B., and Y. Zhang (1997), Spatial and seasonal variability in the components of the river heat budget, *Hydrol Processes*, *11*(1), 79-101.

Webb, B., and Y. Zhang (2004), Intra-annual variability in the non-advective heat energy budget of Devon streams and rivers, *Hydrol Processes*, *18*(11), 2117-2146.

Westhoff, M., H. Savenije, W. Luxemburg, G. Stelling, N. Van de Giesen, J. Selker, L. Pfister, and S. Uhlenbrook (2007), A distributed stream temperature model using high resolution temperature observations, *Hydrol & Earth Syst Sci*, *11*(4).

Westlake, D. (1965), Some problems in the measurement of radiation under water: a review, *Photochem and Photobiol*, *4*(5), 849-868.

Williamson, C. E., R. S. Stemberger, D. P. Morris, T. M. Frost, and S. G. Paulsen (1996), Ultraviolet radiation in North American lakes: attenuation estimates from DOC measurements and implications for plankton communities, *Limnology and Oceanography*, *41*, 1024-1034.

Zibordi, G. (2007), Marine Optics: Field Radiometry, University of Southampton, School of Ocean and Earth Sciences.

Zibordi, G., and M. Darecki (2006), Immersion factors for the RAMSES series of hyper-spectral underwater radiometers, *J of Optics A: Pure and Applied Optics*, *8*(3), 252-258.

Zibordi, G., S. Hooker, J. Mueller, and G. Lazin (2004), Characterization of the immersion factor for a series of in-water optical radiometers, *J of Atmos and Oceanic Tech*, *21*(3), 501-514.

APPENDICES

APPENDIX A

Equations 5 – 7 and 11 – 15 Derivations

Assumptions:

- Each zone has a constant volume
- Each zone is a continuously stirred tank reactor
- Streambed sediments have isotropic thermal properties
- There is no mixing due to wind
- One-dimensional first-order heat exchange occurs between zones
- Area of Zone 1 Layer 1 is equal to the area of Zone 1 Layer 2
- Surface area of the sediments is equal to the surface area of the water zone above it

Variable Key

Subscripts *i* and *j* identify the various zones (i.e. M1, S1, sed, etc.).

Q_{in} = volumetric flow rate into main channel (cm^3 day^{-1})

Q_{out} = volumetric flow rate out of main channel (cm^3 day^{-1})

T_i = Temperature of the zone *i* (^{o}C)

$T_{sed,i}$ = Average temperature of the sediments beneath zone *i* (^{o}C)

$T_{sed,i,n}$ = Average temperature of layer *n* in the sediments beneath zone *i* (^{o}C)

V_i = volume of the zone *i* (cm^3)

$A_{s,i}$ = surface area of the zone *i* (cm^2)

$A_{s,sed,i}$ = surface area of the sediments under zone *i* (cm^2)

ρ_i = density of the zone *i* (g cm^{-3})

c_p = specific heat capacity of the water (cal g^{-1} ^{o}C^{-1})

$c_{p,sed}$ = specific heat capacity of the sediments (cal g^{-1} ^{o}C^{-1})

$v_{i,j}$ = vertical heat transfer coefficient between stratified layers *i* and *j* (cm day^{-1})

$\alpha_{i,j}$ = heat transfer coefficient between zones *i* and *j* (cm^2 day^{-1})

Δz_{sed} = incremental depth of sediment (cm)

$A_{cs,i,j}$ = cross sectional area between zone *i* and *j* (cm^2)

B_i = average width of zone *i* (cm)

K_{sed} = thermal conductivity of the sediment (cal cm^{-2} day^{-1} ^{o}C^{-1}).

α_{sed} = thermal diffusivity of the sediment (cm^2 day^{-1}).

r_{sed} = reflectivity of sediment

η = porosity of sediment (assumed to be 0.3)

$J_{atm,i}$ = net surface heat exchange for zone *i* (cal cm^{-2} d^{-1})

$J_{sn,i}$ = shortwave solar radiation at surface of zone *i* (cal cm^{-2} d^{-1})

$J_{sn,S12,in}$ = shortwave solar radiation reaching the surface of STS Zone 1 Layer 2 (aka S12) (cal cm^{-2} d^{-1})

$J_{sn,sed,i}$ = shortwave solar radiation reaching the sediment surface below zone *i* (cal cm^{-2} d^{-1})

λ_I = attenuation coefficient of zone *i* (cm^{-1})

z_i = depth of zone *i* (cm)

Surface Heat Exchange

$J_{sn,i}$ = shortwave solar radiation reaching depth *z* of zone *i*

$$J_{sn,i} = J_{sn} e^{-\lambda_i z_i}$$

$J_{atm,i}$ = net surface heat exchange for zone *i*

$$J_{atm,i} = J_{sn,i} + J_{an} - (J_{br,i} + J_{e,i} + J_{c,i})$$

Therefore for each zone, the following equations apply:

Main Channel (M1)

$$J_{sn,M1} = J_{sn} - \left(J_{sn} e^{-\lambda_{m1} z_{m1}}\right)$$

$$J_{atm,M1} = J_{sn,M1} + \left[J_{an} - \left(J_{br,M1} + J_{e,M1} + J_{c,M1}\right)\right]$$

Sediments below M1

$$J_{sn,sed,M1} = J_{sn} - J_{sn,M1}$$

Transient Storage Zone 1 Layer 1 (S11)

$$J_{sn,S11} = J_{sn} - \left(J_{sn} e^{-\lambda_{s11} z_{s11}}\right)$$

$$J_{atm,S11} = J_{sn,S11} + \left[J_{an} - \left(J_{br,S11} + J_{e,S11} + J_{c,S11}\right)\right]$$

Transient Storage Zone 1 Layer 2 (S12)

Solar radiation coming in to S12

$$J_{sn,S12,in} = \left(J_{sn} e^{-\lambda_{s11} z_{s11}}\right)$$

Solar radiation absorbed within S12

$$J_{sn,S12} = J_{sn,S12,in} - \left(J_{sn,S12,in} e^{-\lambda_{s12} z_{s12}}\right)$$

Sediments below S12

$$J_{sn,sed,S12} = J_{sn} - J_{sn,S11} - J_{sn,S12}$$

Transient Storage Zone 2 (S2)

$$J_{sn,S2} = J_{sn} - \left(J_{sn} e^{-\lambda_{s2} z_{s2}}\right)$$

$$J_{atm,S2} = J_{sn,S2} + \left[J_{an} - \left(J_{br,S2} + J_{e,S2} + J_{c,S2}\right)\right]$$

Sediments below S2

$$J_{sn,sed,S2} = J_{sn} - J_{sn,S2}$$

Transient Storage Zone 3 (S3)

$$J_{sn,S3} = J_{sn} - \left(J_{sn} e^{-\lambda_{s3} z_{s3}}\right)$$

$$J_{atm,S3} = J_{sn,S3} + \left[J_{an} - \left(J_{br,S3} + J_{e,S3} + J_{c,S3}\right)\right]$$

Sediments below S3

$$J_{sn,sed,S3} = J_{sn} - J_{sn,S3}$$

Sediment Heat Balance

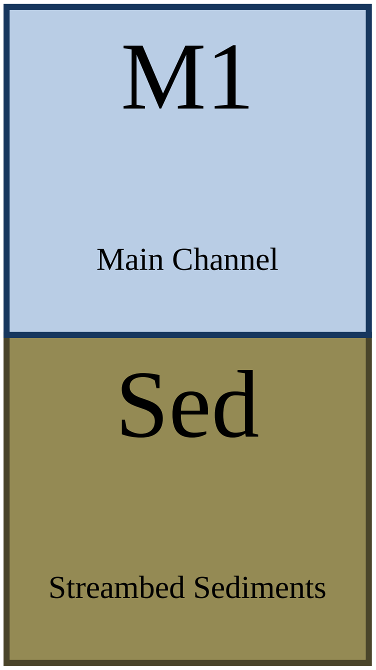

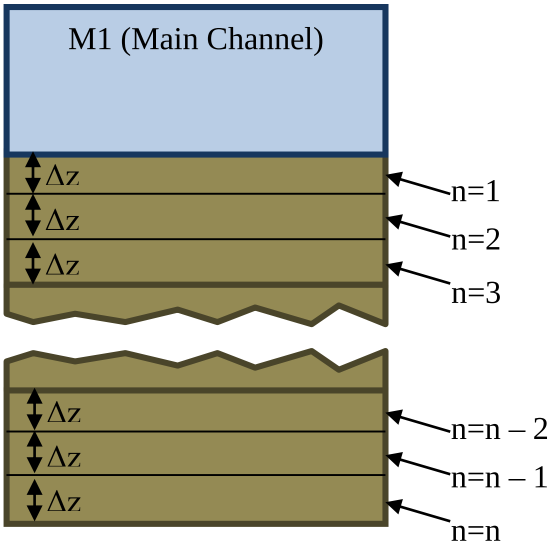

From *Chapra and Canale* [2006]

The heat conduction equation can be written as

$$q(z)\Delta y\Delta x\Delta t - q(z+\Delta z)\Delta y\Delta x\Delta t = \Delta x\Delta y\Delta z\rho c_p\Delta T$$

a.k.a.

$$Inputs - Outputs = Storage$$

$$q(z)A - q(z+\Delta z)A = \rho c_p V\frac{\Delta T}{\Delta t}$$

Where $q(z)$ is the heat flux at location z and $q(z+\Delta z)$ is the heat flux at location $z+\Delta z$

Dividing by $\Delta x\Delta y\Delta z$ (volume):

$$\frac{q(z)}{\Delta z} - \frac{q(z+\Delta z)}{\Delta z} = \rho c_p \frac{\Delta T}{\Delta t}$$

Taking the limit yields:

$$-\frac{\delta q}{\delta z} = \rho c_p \frac{\delta T}{\delta t}$$

Fourier's Law is:

$$q = -\rho c_p \alpha \frac{\delta T}{\delta z}$$

Where α = thermal diffusivity

Taking the derivative with respect to z yields:

$$\frac{\delta q}{\delta z} = -\rho c_p \alpha \frac{\delta^2 T}{\delta z^2}$$

a.k.a. (after dividing both sides by -1)

$$-\frac{\delta q}{\delta z} = \rho c_p \alpha \frac{\delta^2 T}{\delta z^2}$$

Since

$$-\frac{\delta q}{\delta z} = \rho c_p \frac{\delta T}{\delta t}$$

$$\rho c_p \frac{\delta T}{\delta t} = -\frac{\delta q}{\delta z} = \rho c_p \alpha \frac{\delta^2 T}{\delta z^2}$$

$$\rho c_p \frac{\delta T}{\delta t} = \rho c_p \alpha \frac{\delta^2 T}{\delta z^2}$$

Using the Laplace finite-divided difference equations to approximate $\frac{\delta^2 T}{\delta z^2}$

Layer n = 1, Forward Finite-Divided Difference (Upper Boundary Condition)

$$\frac{\delta^2 T_n}{\delta z^2} = \frac{2T_n - 5T_{n+1} + 4T_{n+2} - T_{n+3}}{\Delta z^2}$$

Layer n = 2 to n – 1, Centered Finite-Divided Difference

$$\frac{\delta^2 T_n}{\delta z^2} = \frac{T_{n+1} - 2T_n + T_{n-1}}{\Delta z^2}$$

Layer n = n, Backward Finite-Divided Difference (Lower Boundary Condition)

$$\frac{\delta^2 T_n}{\delta z^2} = \frac{2T_n - 5T_{n-1} + 4T_{n-2} - T_{n-3}}{\Delta z^2}$$

Therefore

Layer n = 1, Forward Finite-Divided Difference (Upper Boundary Condition)

$$\rho c_p \frac{\delta T_n}{\delta t} = \rho c_p \alpha \frac{\delta^2 T_n}{\delta z^2} = \rho c_p \alpha \frac{2T_n - 5T_{n+1} + 4T_{n+2} - T_{n+3}}{\Delta z^2}$$

Layer n = 2 to n – 1, Centered Finite-Divided Difference

$$\rho c_p \frac{\delta T_n}{\delta t} = \rho c_p \alpha \frac{\delta^2 T_n}{\delta z^2} = \rho c_p \alpha \frac{T_{n+1} - 2T_n + T_{n-1}}{\Delta z^2}$$

Layer n = n, Backward Finite-Divided Difference (Lower Boundary Condition)

$$\rho c_p \frac{\delta T_n}{\delta t} = \rho c_p \alpha \frac{\delta^2 T_n}{\delta z^2} = \rho c_p \alpha \frac{2T_n - 5T_{n-1} + 4T_{n-2} - T_{n-3}}{\Delta z^2}$$

Heat Balances

Solar radiation term affecting sediment layer n = 1:

The following terms were included from the *Boyd & Kasper* [2003] Heat Source Model 7.0

$$Solar\ Radiation\ Reflected\ off\ Sediment = r_{sed} J_{sn,sed,i}$$

$$Solar\ Radiation\ Absorbed\ in\ Sediment\ and\ Immediately$$

$$Returned\ to\ Water\ Column\ as\ Heat = J_{sn,sed,i} * 0.53 * (1 - \eta)$$

$$J_{sn,sed,n} = J_{sn,sed,i} - \left(r_{sed} J_{sn,sed,i}\right) - \left[J_{sn,sed,i} * 0.53 * (1 - \eta)\right]$$

$$\rho c_p V_n \frac{\delta T_n}{\delta t} = J_{sn,sed,n} A_{s,n}$$

Divide through by volume:

$$\rho c_p \frac{\delta T_n}{\delta t} = \frac{J_{sn,sed,n} A_{s,n}}{V_n}$$

Layer n = 1, Forward Finite-Divided Difference (Upper Boundary Condition)

including solar radiation term

$$\rho c_p \frac{\delta T_n}{\delta t} = \frac{J_{sn,sed,n} A_{s,n}}{V_n} + \rho c_p \alpha \frac{2T_n - 5T_{n+1} + 4T_{n+2} - T_{n+3}}{\Delta z^2}$$

Layer n = 2 to n – 1, Centered Finite-Divided Difference

$$\rho c_p \frac{\delta T_n}{\delta t} = \rho c_p \alpha \frac{\delta^2 T_n}{\delta z^2} = \rho c_p \alpha \frac{T_{n+1} - 2T_n + T_{n-1}}{\Delta z^2}$$

Layer n = n, Backward Finite-Divided Difference (Lower Boundary Condition)

$$\rho c_p \frac{\delta T_n}{\delta t} = \rho c_p \alpha \frac{\delta^2 T_n}{\delta z^2} = \rho c_p \alpha \frac{2T_n - 5T_{n-1} + 4T_{n-2} - T_{n-3}}{\Delta z^2}$$

Divide through ρc_p for temperature gradient of each

Layer n = 1, Forward Finite-Divided Difference (Upper Boundary Condition)

$$\frac{\delta T_n}{\delta t} = \frac{J_{sn,n} A_{s,n}}{\rho c_p V_n} + \alpha \frac{2T_n - 5T_{n+1} + 4T_{n+2} - T_{n+3}}{\Delta z^2}$$

Layer n = 2 to n – 1, Centered Finite-Divided Difference

$$\frac{\delta T_n}{\delta t} = \alpha \frac{T_{n+1} - 2T_n + T_{n-1}}{\Delta z^2}$$

Layer n = n, Backward Finite-Divided Difference (Lower Boundary Condition)

$$\frac{\delta T_n}{\delta t} = \alpha \frac{2T_n - 5T_{n-1} + 4T_{n-2} - T_{n-3}}{\Delta z^2}$$

Main Channel

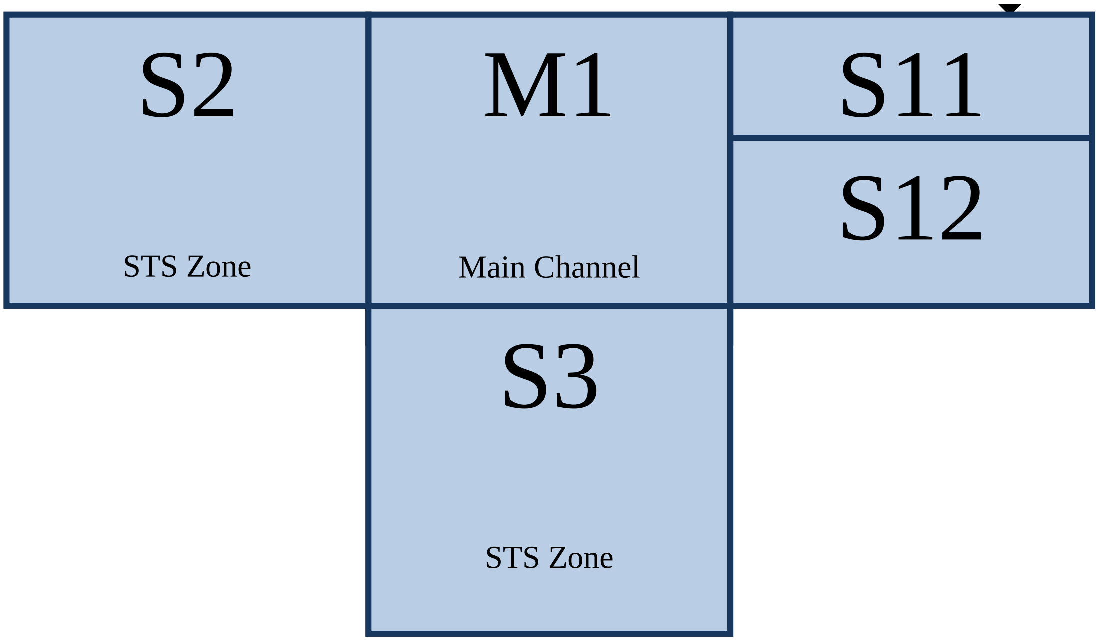

$$Accumulation = \rho_{M1} c_p V_{M1} \frac{dT_{M1}}{dt}$$

$$Inflow = Q_{in} \rho_{M1} c_p T_{in}$$

$$Outflow = Q_{out} \rho_{M1} c_p T_{M1}$$

$$Surface\ Exchange = J_{atm,M1} A_{s,M1}$$

$$Exchange\ with\ S2 = \frac{\alpha_{M1,S2} A_{cs,M1,S2}}{\mathrm{B}_{\mathrm{S2}}} \rho_{M1} c_p (T_{S2} - T_{M1})$$

$$Exchange\ with\ S3 = \frac{\alpha_{M1,S3} A_{cs,M1,S3}}{\mathrm{B}_{\mathrm{S3}}} \rho_{M1} c_p (T_{S3} - T_{M1})$$

$$Exchange\ with\ S11 = \frac{\alpha_{S11,M1} A_{cs,S11,M1}}{\mathrm{B}_{\mathrm{S11}}} \rho_{M1} c_p (T_{S11} - T_{M1})$$

$$Exchange\ with\ S12 = \frac{\alpha_{S12,M1} A_{cs,S12,M1}}{\mathrm{B}_{\mathrm{S12}}} \rho_{M1} c_p (T_{S12} - T_{M1})$$

$$Exchange\ with\ Sediments = \frac{K_{sed}A_{sed,M1}\left(T_{sed,M1} - T_{M1}\right)}{z_{sed}}$$

$$Heat\ from\ Solar\ Radiation\ Received\ from\ Sediments$$

$$+ \left(\left(r_{sed}J_{sn,sed,M1}\right) + \left[J_{sn,sed,M1} * 0.53 * (1 - \eta)\right]\right) A_{s,M1}$$

Overall Equation

$$\rho_{M1}c_pV_{M1}\frac{dT_{M1}}{dt}$$

$$= Q_{in}\rho_{M1}c_pT_{in} - Q_{out}\rho_{M1}c_pT_{M1} + J_{atm,M1}A_{s,M1}$$

$$+ \frac{\alpha_{M1,S2}A_{cs,M1,S2}}{\mathrm{B}_{\mathrm{S2}}}\rho_{M1}c_p(T_{S2} - T_{M1}) + \frac{\alpha_{M1,S3}A_{cs,M1,S3}}{\mathrm{B}_{\mathrm{S3}}}\rho_{M1}c_p(T_{S3} - T_{M1})$$

$$+ \frac{\alpha_{S11,M1}A_{cs,S11,M1}}{\mathrm{B}_{\mathrm{S11}}}\rho_{M1}c_p(T_{S11} - T_{M1})$$

$$+ \frac{\alpha_{S12,M1}A_{cs,S12,M1}}{\mathrm{B}_{\mathrm{S12}}}\rho_{M1}c_p(T_{S12} - T_{M1}) + \frac{K_{sed}A_{sed,M1}\left(T_{sed,M1} - T_{M1}\right)}{z_{sed}}$$

$$+ \left(\left(r_{sed}J_{sn,sed,M1}\right) + \left[J_{sn,sed,M1} * 0.53 * (1 - \eta)\right]\right)A_{s,M1}$$

Divide by $\rho_{M1}c_pV_{M1}$

$$\frac{\rho_{M1}c_pV_{M1}}{\rho_{M1}c_pV_{M1}}\frac{dT_{M1}}{dt}$$

$$= \frac{Q_{in}\rho_{M1}c_pT_{in}}{\rho_{M1}c_pV_{M1}} - \frac{Q_{out}\rho_{M1}c_pT_{M1}}{\rho_{M1}c_pV_{M1}} + \frac{J_{atm,M1}A_{s,M1}}{\rho_{M1}c_pV_{M1}}$$

$$+ \frac{\alpha_{M1,S2}A_{cs,M1,S2}}{\mathrm{B}_{\mathrm{S2}}\rho_{M1}c_pV_{M1}}\rho_{M1}c_p(T_{S2} - T_{M1}) + \frac{\alpha_{M1,S3}A_{cs,M1,S3}}{\mathrm{B}_{\mathrm{S3}}\rho_{M1}c_pV_{M1}}\rho_{M1}c_p(T_{S3} - T_{M1})$$

$$+ \frac{\alpha_{S11,M1}A_{cs,S11,M1}}{\mathrm{B}_{\mathrm{S11}}\rho_{M1}c_pV_{M1}}\rho_{M1}c_p(T_{S11} - T_{M1})$$

$$+ \frac{\alpha_{S12,M1}A_{cs,S12,M1}}{\mathrm{B}_{\mathrm{S12}}\rho_{M1}c_pV_{M1}}\rho_{M1}c_p(T_{S12} - T_{M1}) + \frac{K_{sed}A_{sed,M1}\left(T_{sed,M1} - T_{M1}\right)}{z_{sed}\rho_{M1}c_pV_{M1}}$$

$$+ \frac{\left(\left(r_{sed}J_{sn,sed,M1}\right) + \left[J_{sn,sed,M1} * 0.53 * (1 - \eta)\right]\right)A_{s,M1}}{\rho_{M1}c_pV_{M1}}$$

Cancelling terms

$$\frac{dT_{M1}}{dt} = \frac{Q_{in}T_{in}}{V_{M1}} - \frac{Q_{out}T_{M1}}{V_{M1}} + \frac{J_{atm,M1}A_{s,M1}}{\rho_{M1}c_pV_{M1}} + \frac{\alpha_{S11,M1}A_{cs,S11,M1}}{\mathrm{B}_{\mathrm{S11}}V_{M1}}(T_{S11} - T_{M1})$$
$$+ \frac{\alpha_{S12,M1}A_{cs,S12,M1}}{\mathrm{B}_{\mathrm{S12}}V_{M1}}(T_{S12} - T_{M1}) + \frac{\alpha_{M1,S2}A_{cs,M1,S2}}{\mathrm{B}_{\mathrm{S2}}V_{M1}}(T_{S2} - T_{M1})$$
$$+ \frac{\alpha_{M1,S3}A_{cs,M1,S3}}{\mathrm{B}_{\mathrm{S3}}V_{M1}}(T_{S3} - T_{M1}) + \frac{K_{sed}A_{sed,M1}\left(T_{sed,M1} - T_{M1}\right)}{z_{sed}\rho_{M1}c_pV_{M1}}$$
$$+ \frac{\left(\left(r_{sed}J_{sn,sed,M1}\right) + \left[J_{sn,sed,M1} * 0.53 * (1-\eta)\right]\right)A_{s,M1}}{\rho_{M1}c_pV_{M1}}$$

STS Zone 1 Stratified Layer 1 (S11)

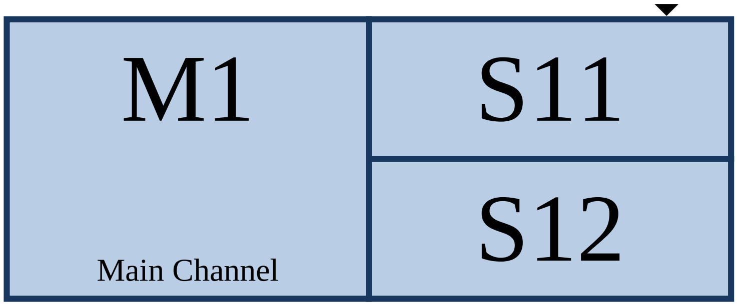

$$Accumulation = \rho_{S11} c_p V_{S11} \frac{dT_{S11}}{dt}$$

$$Surface\ Exchange = J_{atm,S11} A_{s,S11}$$

$$Exchange\ with\ M1 = \frac{\alpha_{S11,M1} A_{cs,S11,M1}}{\mathrm{B}_{\mathrm{M1}}} \rho_{S11} c_p (T_{M1} - T_{S11})$$

$$Exchange\ with\ S12 = v_{S11,12} A_{s,S12} \rho_{S11} c_p (T_{S12} - T_{S11})$$

Overall Equation

$$\rho_{S11} c_p V_{S11} \frac{dT_{S11}}{dt}$$

$$= J_{atm,S11} A_{s,S11} + \frac{\alpha_{S11,M1} A_{cs,S11,M1}}{\mathrm{B}_{\mathrm{M1}}} \rho_{S11} c_p (T_{M1} - T_{S11})$$

$$+ v_{S11,12} A_{s,S12} \rho_{S11} c_p (T_{S12} - T_{S11})$$

Divide by $\rho_{S11} c_p V_{S11}$

$$\frac{\rho_{S11} c_p V_{S11}}{\rho_{S11} c_p V_{S11}} \frac{dT_{S11}}{dt}$$

$$= \frac{J_{atm,S11} A_{s,S11}}{\rho_{S11} c_p V_{S11}} + \frac{\alpha_{S11,M1} A_{cs,S11,M1}}{\mathrm{B}_{\mathrm{M1}} \rho_{S11} c_p V_{S11}} \rho_{S11} c_p (T_{M1} - T_{S11})$$

$$+ \frac{v_{S11,12} A_{s,S12} \rho_{S11} c_p (T_{S12} - T_{S11})}{\rho_{S11} c_p V_{S11}}$$

Cancelling terms

$$\frac{dT_{S11}}{dt} = \frac{J_{atm,S11}A_{s,S11}}{\rho_{S11}c_p V_{S11}} + \frac{\alpha_{S11,M1}A_{cs,S11,M1}}{\mathrm{B}_{\mathrm{M1}}V_{S11}}(T_{M1} - T_{S11}) + \frac{v_{S11,12}A_{s,S12}(T_{S12} - T_{S11})}{V_{S11}}$$

STS Zone 1 Stratified Layer 2 (S12)

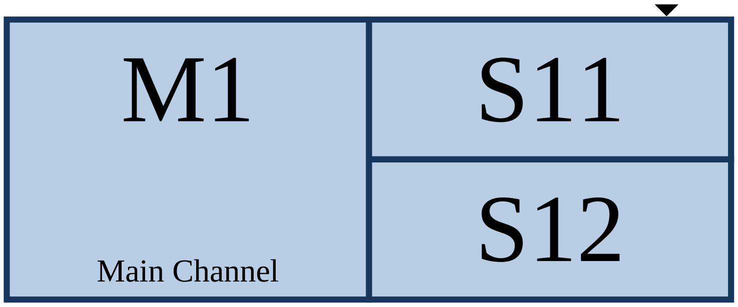

$$\mathit{Accumulation} = \rho_{S12} c_p V_{S12} \frac{dT_{S12}}{dt}$$

$$\mathit{Attenuated\ Solar\ Radiation} = J_{sn,S12} A_{s,S12}$$

$$\mathit{Exchange\ with\ S11} = v_{S11,12} A_{s,S12} \rho_{S12} c_p \left(T_{S11} - T_{S12}\right)$$

$$\mathit{Exchange\ with\ M1} = \frac{\alpha_{S12,M1} A_{cs,S12,M1}}{\mathrm{B}_{M1}} \rho_{S12} c_p \left(T_{M1} - T_{S12}\right)$$

$$\mathit{Exchange\ with\ Sediments} = \frac{K_{sed} A_{sed,S12} \left(T_{sed,S12} - T_{S12}\right)}{z_{sed}}$$

$$\mathit{Heat\ from\ Solar\ Radiation\ Received\ from\ Sediments}$$
$$= \left(\left(r_{sed} J_{sn,sed,s12}\right) + \left[J_{sn,sed,s12} * 0.53 * (1 - \eta)\right]\right) A_{s,S12}$$

Overall Equation

$$
\begin{aligned}
\rho_{S12} c_p V_{S12} \frac{dT_{S12}}{dt}
&= J_{sn,S12} A_{s,S12} + v_{S11,12} A_{s,S12} \rho_{S12} c_p (T_{S11} - T_{S12}) \\
&+ \frac{\alpha_{S12,M1} A_{cs,S12,M1}}{\mathrm{B}_{M1}} \rho_{S12} c_p (T_{M1} - T_{S12}) + \frac{K_{sed} A_{sed,S12} \left(T_{sed,S12} - T_{S12}\right)}{z_{sed}} \\
&+ \left(\left(r_{sed} J_{sn,sed,s12}\right) + \left[J_{sn,sed,s12} * 0.53 * (1 - \eta)\right] \right) A_{s,s12}
\end{aligned}
$$

Divide by $\rho_{S12} c_p V_{S12}$

$$
\begin{aligned}
\frac{\rho_{S12} c_p V_{S12}}{\rho_{S12} c_p V_{S12}} \frac{dT_{S12}}{dt}
&= \frac{J_{sn,S12} A_{s,S12}}{\rho_{S12} c_p V_{S12}} + \frac{v_{S11,12} A_{s,S12} \rho_{S12} c_p (T_{S11} - T_{S12})}{\rho_{S12} c_p V_{S12}} \\
&+ \frac{\alpha_{S12,M1} A_{cs,S12,M1}}{\mathrm{B}_{M1} \rho_{S12} c_p V_{S12}} \rho_{S12} c_p (T_{M1} - T_{S12}) + \frac{K_{sed} A_{sed,S12} \left(T_{sed,S12} - T_{S12}\right)}{\rho_{S12} c_p V_{S12} z_{sed}} \\
&+ \frac{\left(\left(r_{sed} J_{sn,sed,S12}\right) + \left[J_{sn,sed,S12} * 0.53 * (1 - \eta)\right] \right) A_{s,S12}}{\rho_{S12} c_p V_{S12}}
\end{aligned}
$$

Cancelling terms

$$
\begin{aligned}
\frac{dT_{S12}}{dt} &= \frac{J_{sn,S12} A_{s,S12}}{\rho_{S12} c_p V_{S12}} + \frac{v_{S11,12} A_{s,S12} (T_{S11} - T_{S12})}{V_{S12}} + \frac{\alpha_{S12,M1} A_{cs,S12,M1}}{\mathrm{B}_{M1} V_{S12}} (T_{M1} - T_{S12}) \\
&+ \frac{K_{sed} A_{sed,S12} \left(T_{sed,S12} - T_{S12}\right)}{\rho_{S12} c_p V_{S12} z_{sed}} \\
&+ \frac{\left(\left(r_{sed} J_{sn,sed,S12}\right) + \left[J_{sn,sed,S12} * 0.53 * (1 - \eta)\right] \right) A_{s,S12}}{\rho_{S12} c_p V_{S12}}
\end{aligned}
$$

STS Zone 2

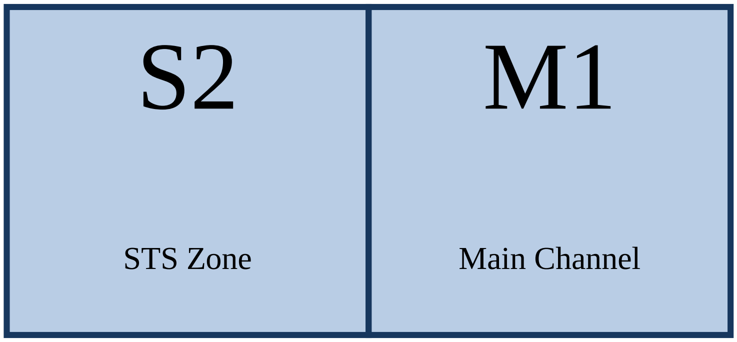

$$Accumulation = \rho_{S2}c_pV_{S2}\frac{dT_{S2}}{dt}$$

$$Surface\ Exchange = J_{atm,S2}A_{s,S2}$$

$$Exchange\ with\ M1 = \frac{\alpha_{S2,M1}A_{cs,S2,M1}}{\mathrm{B}_{M1}}\rho_{S2}c_p(T_{M1} - T_{S2})$$

$$Exchange\ with\ Sediments = \frac{K_{sed}A_{sed,S2}\left(T_{sed,S2} - T_{S2}\right)}{z_{sed}}$$

$$Heat\ from\ Solar\ Radiation\ Received\ from\ Sediments$$

$$= \left(\left(r_{sed}J_{sn,sed,s2}\right) + \left[J_{sn,sed,s2} * 0.53 * (1 - \eta)\right]\right)A_{s,S2}$$

Overall Equation

$$\rho_{S2}c_pV_{S2}\frac{dT_{S2}}{dt} = J_{atm,S2}A_{s,S2} + \frac{\alpha_{S2,M1}A_{cs,S2,M1}}{\mathrm{B}_{M1}}\rho_{S2}c_p(T_{M1} - T_{S2})$$

$$+ \frac{K_{sed}A_{sed,S2}\left(T_{sed,S2} - T_{S2}\right)}{z_{sed}}$$

$$+ \left(\left(r_{sed}J_{sn,sed,s2}\right) + \left[J_{sn,sed,s2} * 0.53 * (1 - \eta)\right]\right)A_{s,S2}$$

Divide by $\rho_{S2}c_pV_{S2}$

$$\frac{\rho_{S2}c_pV_{S2}}{\rho_{S2}c_pV_{S2}}\frac{dT_{S2}}{dt}=\frac{J_{atm,S2}A_{s,S2}}{\rho_{S2}c_pV_{S2}}+\frac{\alpha_{S2,M1}A_{cs,S2,M1}}{\mathrm{B}_{M1}\rho_{S2}c_pV_{S2}}\rho_{S2}c_p(T_{M1}-T_{S2})$$

$$+\frac{K_{sed}A_{sed,S2}\left(T_{sed,S2}-T_{S2}\right)}{\rho_{S2}c_pV_{S2}z_{sed}}$$

$$+\frac{\left(\left(r_{sed}J_{sn,sed,s2}\right)+\left[J_{sn,sed,s2}*0.53*(1-\eta)\right]\right)A_{s,S2}}{\rho_{S2}c_pV_{S2}}$$

Cancelling terms

$$\frac{dT_{S2}}{dt}=\frac{J_{atm,S2}A_{s,S2}}{\rho_{S2}c_pV_{S2}}+\frac{\alpha_{S2,M1}A_{cs,S2,M1}}{\mathrm{B}_{M1}V_{S2}}(T_{M1}-T_{S2})+\frac{K_{sed}A_{sed,S2}\left(T_{sed,S2}-T_{S2}\right)}{\rho_{S2}c_pV_{S2}z_{sed}}$$

$$+\frac{\left(\left(r_{sed}J_{sn,sed,S2}\right)+\left[J_{sn,sed,S2}*0.53*(1-\eta)\right]\right)A_{s,S2}}{\rho_{S2}c_pV_{S2}}$$

STS Zone 3

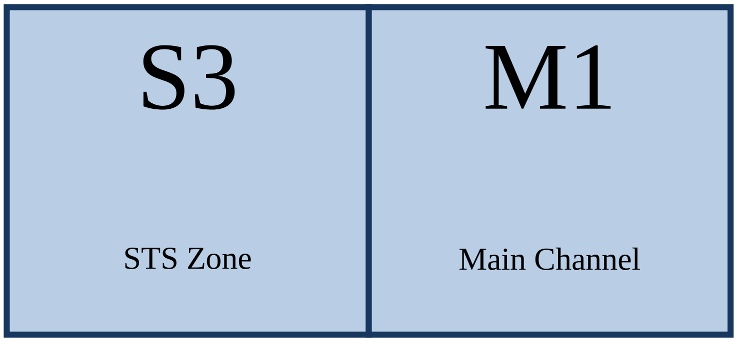

$$Accumulation = \rho_{S3} c_p V_{S3} \frac{dT_{S3}}{dt}$$

$$Surface\ Exchange = J_{atm,S3} A_{s,S3}$$

$$Exchange\ with\ M1 = \frac{\alpha_{M1,S3} A_{cs,M1,S3}}{\mathrm{B}_{\mathrm{M1}}} \rho_{S3} c_p (T_{M1} - T_{S3})$$

$$Exchange\ with\ Sediments = \frac{K_{sed} A_{sed,S3} \left(T_{sed,S3} - T_{S3}\right)}{z_{sed}}$$

$$Heat\ from\ Solar\ Radiation\ Received\ from\ Sediments$$

$$= \left(\left(r_{sed} J_{sn,sed,s3}\right) + \left[J_{sn,sed,s3} * 0.53 * (1 - \eta)\right]\right) A_{s,S3}$$

Overall Equation

$$\rho_{S3} c_p V_{S3} \frac{dT_{S3}}{dt} = J_{atm,S3} A_{s,S3} + \frac{\alpha_{M1,S3} A_{cs,M1,S3}}{\mathrm{B}_{\mathrm{M1}}} \rho_{S3} c_p (T_{M1} - T_{S3})$$

$$+ \frac{K_{sed} A_{sed,S3} \left(T_{sed,S3} - T_{S3}\right)}{z_{sed}}$$

$$+ \left(\left(r_{sed} J_{sn,sed,s3}\right) + \left[J_{sn,sed,s3} * 0.53 * (1 - \eta)\right]\right) A_{s,S3}$$

Divide by $\rho_{S4} c_p V_{S3}$

$$\frac{\rho_{S3} c_p V_{S3}}{\rho_{S3} c_p V_{S3}} \frac{dT_{S3}}{dt} = \frac{J_{atm,S3} A_{s,S3}}{\rho_{S3} c_p V_{S3}} + \frac{\alpha_{M1,S3} A_{cs,M1,S3}}{\mathrm{B}_{\mathrm{M1}} \rho_{S3} c_p V_{S3}} \rho_{S3} c_p (T_{M1} - T_{\mathrm{S3}})$$

$$+ \frac{K_{sed} A_{sed,S3} \left(T_{sed,S3} - T_{S3}\right)}{\rho_{S3} c_p V_{S3} z_{sed}}$$

$$+ \frac{\left(\left(r_{sed} J_{sn,sed,s3}\right) + \left[J_{sn,sed,s3} * 0.53 * (1 - \eta)\right]\right) A_{s,S3}}{\rho_{S3} c_p V_{S3}}$$

Cancelling Terms

$$\frac{dT_{S3}}{dt} = \frac{J_{atm,S3} A_{s,S3}}{\rho_{S3} c_p V_{S3}} + \frac{\alpha_{M1,S3} A_{cs,M1,S3}}{\mathrm{B}_{\mathrm{M1}} V_{S3}} (T_{M1} - T_{\mathrm{S3}}) + \frac{K_{sed} A_{sed,S3} \left(T_{sed,S3} - T_{S3}\right)}{\rho_{S3} c_p V_{S3} z_{sed}}$$

$$+ \frac{\left(\left(r_{sed} J_{sn,sed,S3}\right) + \left[J_{sn,sed,S3} * 0.53 * (1 - \eta)\right]\right) A_{s,S3}}{\rho_{S3} c_p V_{S3}}$$

<u>Sediment Zones</u>

Beneath Main Channel (M1)

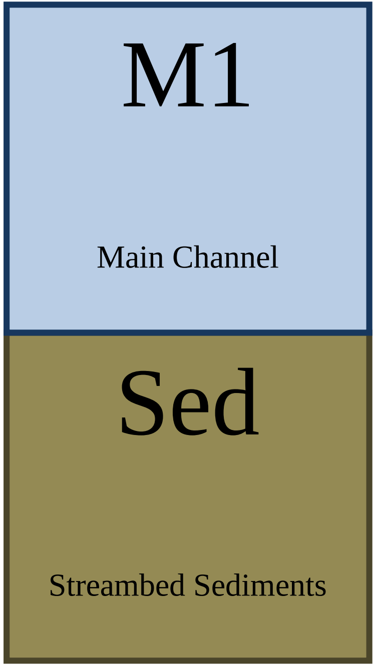

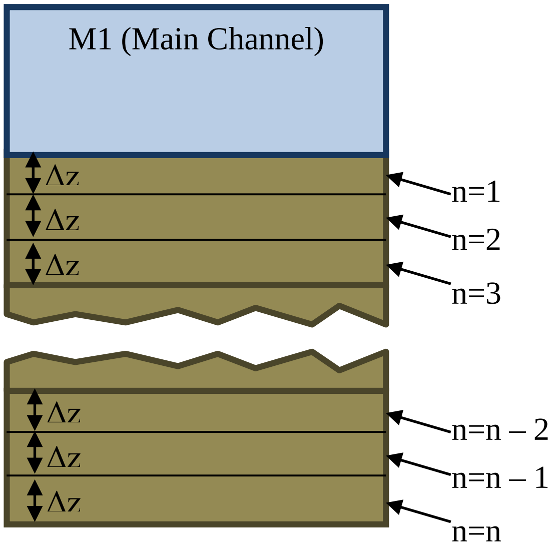

Layer n = 1, Forward Finite-Divided Difference (Upper Boundary Condition)

$$\frac{\delta T_{sed,M1,n=1}}{\delta t} = \frac{J_{sn,sed,M1} A_{s,sed,M1}}{\rho_{sed} c_{p,sed} V_{sed,M1,n=1}} + \alpha \frac{2T_{M1} - 5T_{sed,M1,n=1} + 4T_{sed,M1,n=2} - T_{sed,M1,n=3}}{\Delta z^2}$$

Layer n = 2 to n – 1, Centered Finite-Divided Difference

$$\frac{\delta T_{sed,M1,n=2\ to\ n-1}}{\delta t} = \alpha \frac{T_{sed,M1,n+1} - 2T_{sed,M1,n} + T_{sed,M1,n-1}}{\Delta z^2}$$

Layer n = n, Backward Finite-Divided Difference (Lower Boundary Condition)

$$\frac{\delta T_{sed,M1,n=n}}{\delta t} = \alpha \frac{2T_{sed,M1,n=n} - 5T_{sed,M1,n=n-1} + 4T_{sed,M1,n=n-2} - T_{sed,M1,n=n-3}}{\Delta z^2}$$

Beneath STS Zone 1 Layer 2

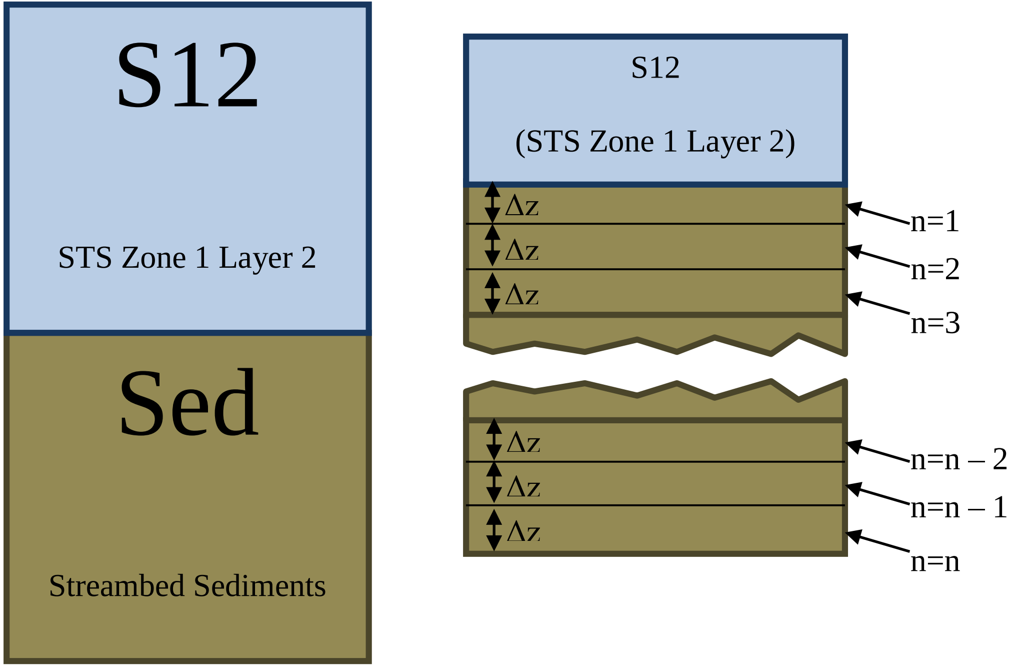

Layer n = 1, Forward Finite-Divided Difference (Upper Boundary Condition)

$$\frac{\delta T_{sed,S12,n=1}}{\delta t} = \frac{J_{sn,sed,S12} A_{s,sed,S12}}{\rho_{sed} c_{p,sed} V_{sed,S12,n=1}} + \alpha \frac{2T_{S12} - 5T_{sed,S12,n=1} + 4T_{sed,S12,n=2} - T_{sed,S12,n=3}}{\Delta z^2}$$

Layer n = 2 to n – 1, Centered Finite-Divided Difference

$$\frac{\delta T_{sed,S12,n=2\ to\ n-1}}{\delta t} = \alpha \frac{T_{sed,S12,n+1} - 2T_{sed,S12,n} + T_{sed,S12,n-1}}{\Delta z^2}$$

Layer n = n, Backward Finite-Divided Difference (Lower Boundary Condition)

$$\frac{\delta T_{sed,S12,n=n}}{\delta t} = \alpha \frac{2T_{sed,S12,n=n} - 5T_{sed,S12,n=n-1} + 4T_{sed,S12,n=n-2} - T_{sed,S12,n=n-3}}{\Delta z^2}$$

Beneath STS Zone 2

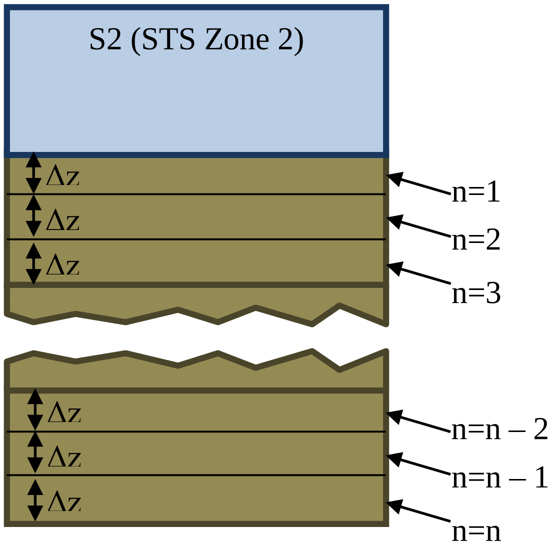

Layer n = 1, Forward Finite-Divided Difference (Upper Boundary Condition)

$$\frac{\delta T_{sed,S2,n=1}}{\delta t} = \frac{J_{sn,sed,S2} A_{s,sed,S2}}{\rho_{sed} c_{p,sed} V_{sed,S2,n=1}} + \alpha \frac{2T_{S2} - 5T_{sed,S2,n=1} + 4T_{sed,S2,n=2} - T_{sed,S2,n=3}}{\Delta z^2}$$

Layer n = 2 to n – 1, Centered Finite-Divided Difference

$$\frac{\delta T_{sed,S2,n=2\ to\ n-1}}{\delta t} = \alpha \frac{T_{sed,S2,n+1} - 2T_{sed,S2,n} + T_{sed,S2,n-1}}{\Delta z^2}$$

Layer n = n, Backward Finite-Divided Difference (Lower Boundary Condition)

$$\frac{\delta T_{sed,S2,n=n}}{\delta t} = \alpha \frac{2T_{sed,S2,n=n} - 5T_{sed,S2,n=n-1} + 4T_{sed,S2,n=n-2} - T_{sed,S2,n=n-3}}{\Delta z^2}$$

Beneath STS Zone 3

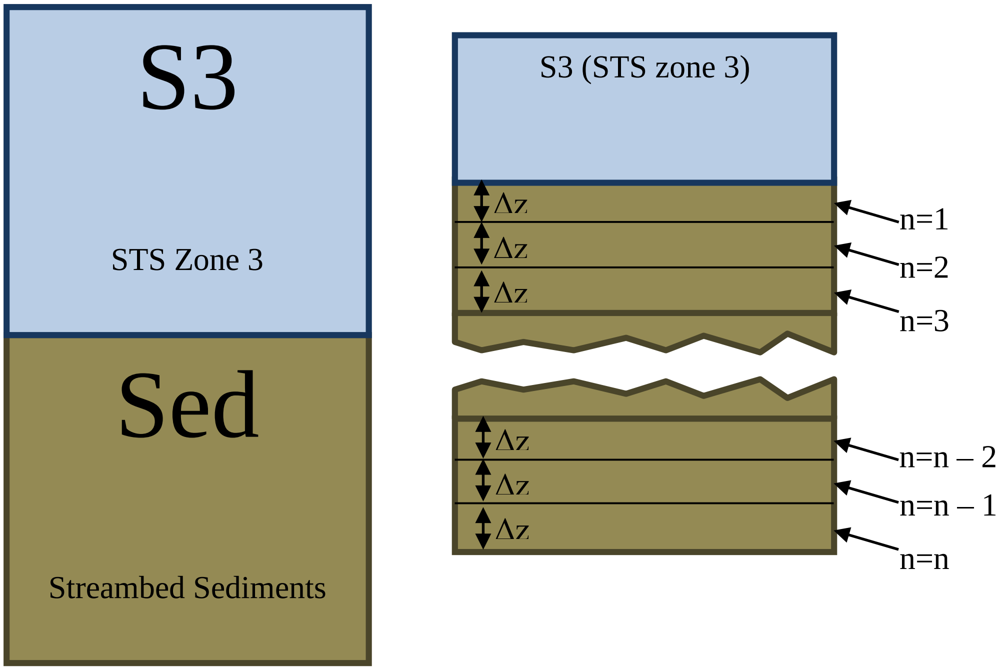

Layer n = 1, Forward Finite-Divided Difference (Upper Boundary Condition)

$$\frac{\delta T_{sed,S3,n=1}}{\delta t} = \frac{J_{sn,sed,S3} A_{s,sed,S3}}{\rho_{sed} c_{p,sed} V_{sed,S3,n=1}} + \alpha \frac{2T_{S3} - 5T_{sed,S3,n=1} + 4T_{sed,S3,n=2} - T_{sed,S3,n=3}}{\Delta z^2}$$

Layer n = 2 to n – 1, Centered Finite-Divided Difference

$$\frac{\delta T_{sed,S3,n=2\ to\ n-1}}{\delta t} = \alpha \frac{T_{sed,S3,n+1} - 2T_{sed,S3,n} + T_{sed,S3,n-1}}{\Delta z^2}$$

Layer n = n, Backward Finite-Divided Difference (Lower Boundary Condition)

$$\frac{\delta T_{sed,S3,n=n}}{\delta t} = \alpha \frac{2T_{sed,S3,n=n} - 5T_{sed,S3,n=n-1} + 4T_{sed,S3,n=n-2} - T_{sed,S3,n=n-3}}{\Delta z^2}$$

APPENDIX B

Procedure to convert between calories per centimeter squared per day (cal cm^{-2} d^{-1}) and watts per meter squared (W m^{-2}) assuming continuous light throughout a 24-hour period:

Convert from $\frac{cal}{cm^2 d}$ to $\frac{W}{m^2}$:

$$1\,\frac{cal}{cm^2 d} * \frac{4.184\,J}{cal} * \frac{10{,}000\,cm^2}{m^2} = 41{,}840\,\frac{J}{m^2 d}$$

$$41{,}840\,\frac{J}{m^2 d} * \frac{d}{24\,hr} * \frac{hr}{3600\,s} * \frac{W}{\frac{J}{s}} = 0.484\,\frac{W}{m^2}$$

Convert from $\frac{W}{m^2}$ to $\frac{cal}{cm^2 d}$:

$$1\,\frac{W}{m^2} * \frac{\frac{J}{s}}{W} * \frac{cal}{4.184J} * \frac{24\,hr}{d} * \frac{3600\,s}{hr} * \frac{m^2}{10{,}000\,cm^2} = 2.065\,\frac{cal}{cm^2 d}$$

APPENDIX C

All equations and approximate constant values presented in Appendix A are based on *Chapra* [1997].

Atmospheric Longwave Radiation:

$$J_{an} = \sigma(T_{air} + 273)^4(A + 0.031\sqrt{e_{air}})(1 - R_L)$$

Where:

J_{an} = atmospheric longwave radiation heat flux (cal cm^{-2} d^{-1})
σ = Stefan-Boltzmann constant - 11.7E-8 cal (cm^2 d K^4)$^{-1}$
T_{air} = air temperature ($°C$)
A = a coefficient (0.5 to 0.7)
e_{air} = air vapor pressure (mmHg)
R_L = reflection coefficient (generally 0.03)

Air Vapor Pressure:

$$e_{air} = (RH/100\ ) *\ e_{sat}$$

Where:

e_{air} = air vapor pressure (mmHg)
RH = relative humidity (%)
e_s = vapor pressure at water surface (mmHg)

Saturation Vapor Pressure:

$$e_{sat} = 4.596e^{\frac{17.27T_{air}}{237.3+T_{air}}}$$

Where:

e_{sat} = saturation vapor pressure (mmHg)

Water Longwave Radiation:

$$J_{br} = \epsilon\sigma(T_s + 273)^4$$

Where:

J_{br} = water longwave radiation heat flux (cal cm^{-2} d^{-1})

ϵ = emissivity of water (approximately 0.97)
T_s = water surface temperature ($°C$)

Conduction and Convection:

$$J_c = c_1 f(U_w)(T_s - T_{air})$$

Where:
J_c = conduction and convection heat flux (cal cm^{-2} d^{-1})
c_1 = Bowen's coefficient (~0.47 mmHg $°C^{-1}$)
$f(U_w)$ = coefficient for transfer of wind velocity over the water surface. The wind transfer coefficient can be calculated using the wind transfer coefficient equation

Wind Transfer Coefficient:

$$f(U_w) = 19.0 + 0.95U_w^2$$

Where:
$f(U_w)$ = wind transfer coefficient
U_w = wind speed measured seven meters above the water surface (m s^{-1})

Evaporation/Condensation:

$$J_e = f(U_w)(e_s - e_{air})$$

Where:
J_e = evaporation/condensation heat flux (cal cm^{-2} d^{-1})
e_s = vapor pressure at the water surface (mmHg).

Vapor Pressure at Water Surface:

$$e_s = 4.596e^{\frac{17.27T_s}{237.3+T_s}}$$

Where:
e_s = vapor pressure at water surface (mmHg)

APPENDIX D

Table D.1: Sediment thermal conductivity and diffusivity data collected and analyzed using a thermal properties sensor (Model KD2Pro SH-1; Decagon Devices, Pullman, WA)

Soil Core Sample	**Core Diameter**	**Depth**	**Thermal Conductivity**	**Diffusivity**
	cm	**cm**	**W/(m·K)**	**mm²/s**
A (small diameter)	1.5	0-6	0.428	0.227
A (small diameter)	1.5	0-6	0.798	0.306
A (small diameter)	1.5	0-6	0.565	0.225
B (small diameter)	1.5	0-9	0.386	0.180
B (small diameter)	1.5	0-9	0.668	0.207
B (small diameter)	1.5	0-9	0.242	0.124
C (large diameter)	5	9-19	1.181	0.221
C (large diameter)	5	9-19	0.860	0.268
C (large diameter)	5	9-19	0.938	0.298
C (large diameter)	5	0-9	0.934	0.289
C (large diameter)	5	0-9	0.803	0.310
C (large diameter)	5	0-9	0.969	0.311
D (large diameter)	5	12-16	0.907	0.351
D (large diameter)	5	12-16	1.035	0.314
D (large diameter)	5	12-16	0.981	0.311
D (large diameter)	5	5-12	0.832	0.229
D (large diameter)	5	5-12	0.881	0.252
D (large diameter)	5	0-5	0.790	0.212
D (large diameter)	5	0-5	0.789	0.216
D (large diameter)	5	0-5	0.828	0.212

Table D.2: RMSE values comparing the predicted sediment temperatures to the observed sediment temperatures beneath each zone at depths of 5, 10, 25, 50, and 75 centimeters below the sediment-water interface

Zone	***5 cm***	***10 cm***	***25 cm***	***50 cm***	***75 cm***
Main Channel	2.01	1.77	1.42	0.33	0.09
STS zone 1	0.42	0.56	0.57	0.34	0.05
STS zone 2	2.69	2.31	1.82	0.50	0.12
STS zone 3	2.76	2.36	1.85	0.51	0.12

APPENDIX E

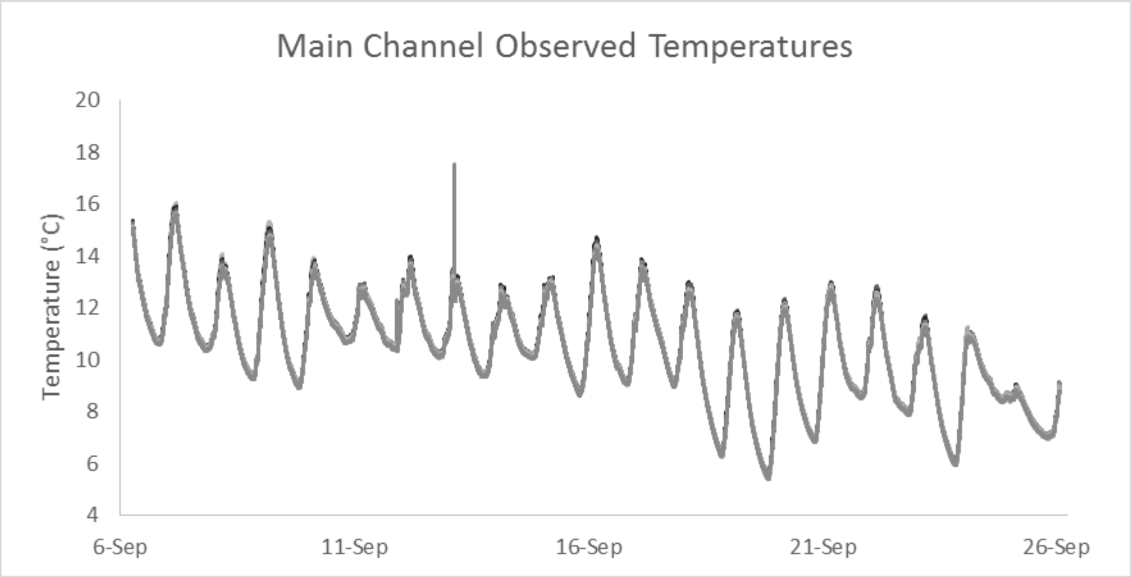

Figure E.1: Continuous water temperature data used for main channel segmentation collected in the beaver pond calibration September 6, 2013 18:00 – September 26, 2013 13:55 MST at 5-minute increments using thirty-one HOBO Pro v2 temperature sensors (Onset Computer Corporation, Cape Cod, MA)

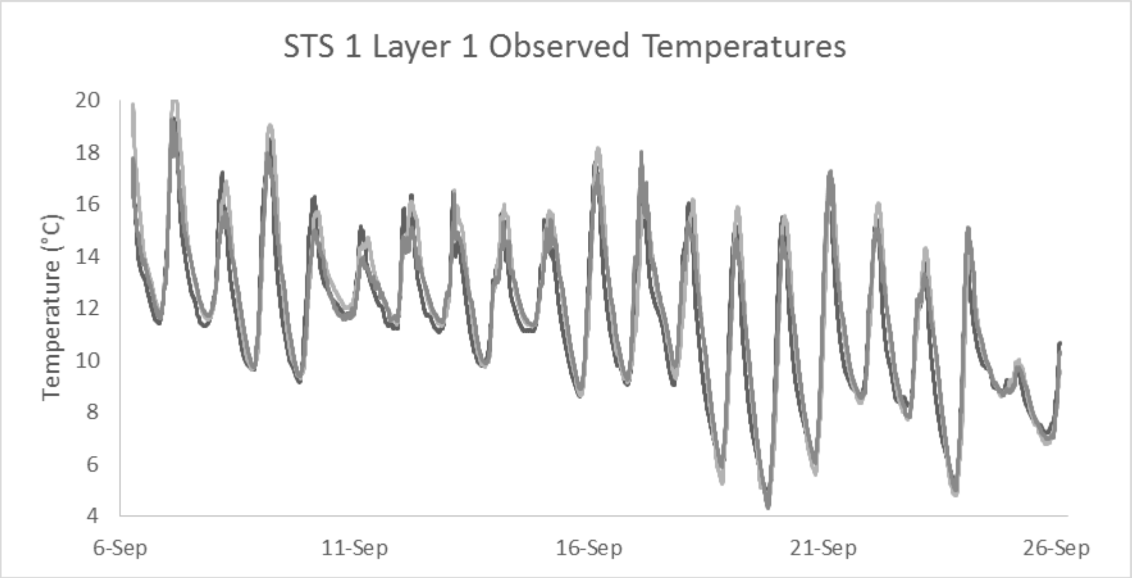

Figure E.2: Continuous water temperature data used for STS 1 Layer 1 segmentation collected in the beaver pond calibration September 6, 2013 18:00 – September 26, 2013 13:55 MST at 5-minute increments using three HOBO Pro v2 temperature sensors (Onset Computer Corporation, Cape Cod, MA)

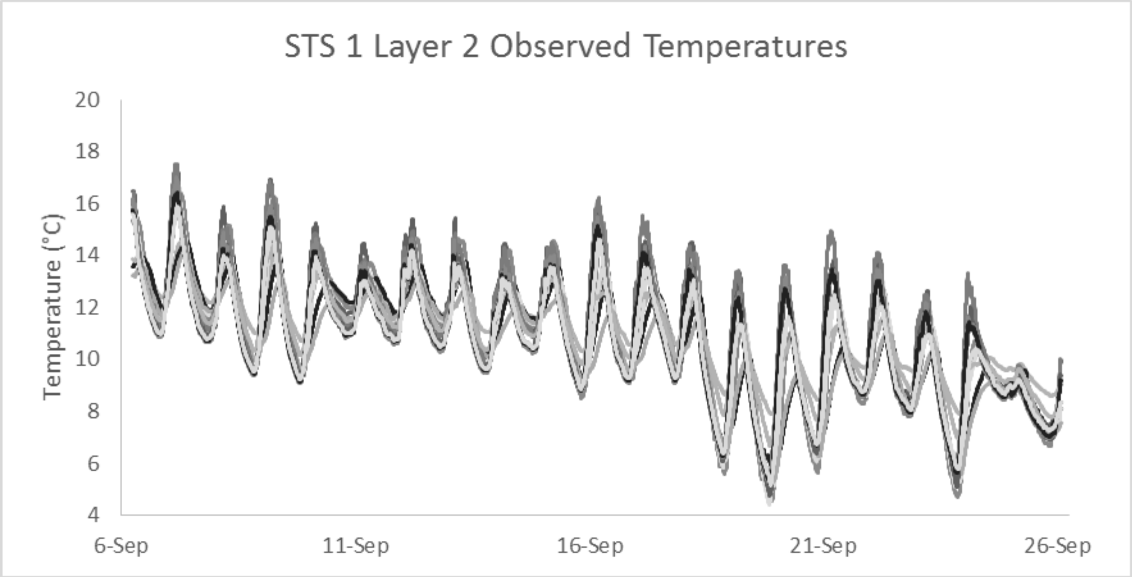

Figure E.3: Continuous water temperature data used for STS 1 Layer 2 segmentation collected in the beaver pond calibration September 6, 2013 18:00 – September 26, 2013 13:55 MST at 5-minute increments using twelve HOBO Pro v2 temperature sensors (Onset Computer Corporation, Cape Cod, MA)

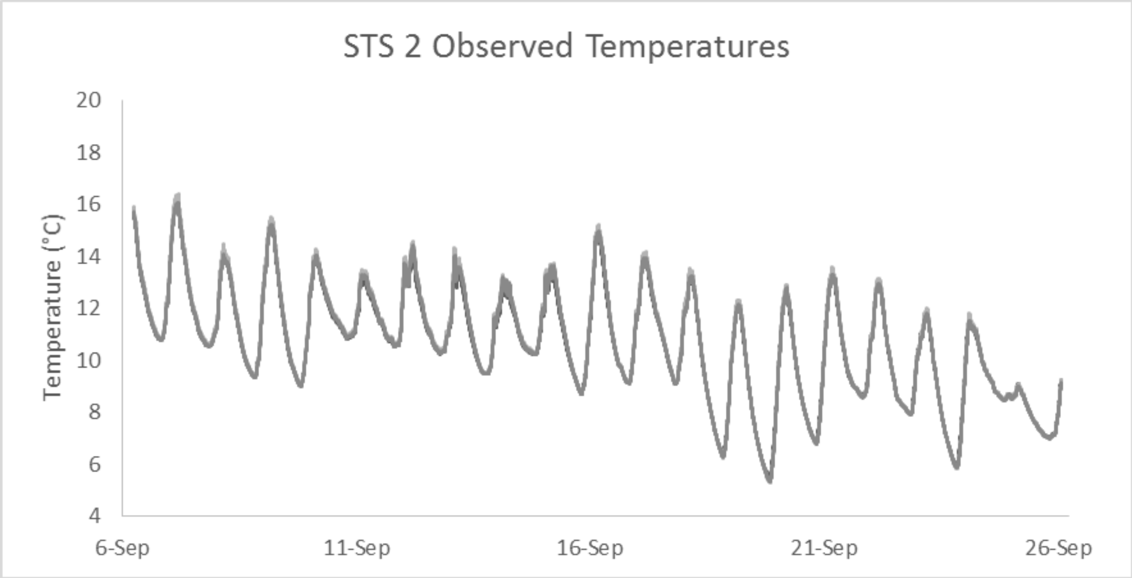

Figure E.4: Continuous water temperature data used for STS 2 segmentation collected in the beaver pond calibration September 6, 2013 18:00 – September 26, 2013 13:55 MST at 5-minute increments using three HOBO Pro v2 temperature sensors (Onset Computer Corporation, Cape Cod, MA)

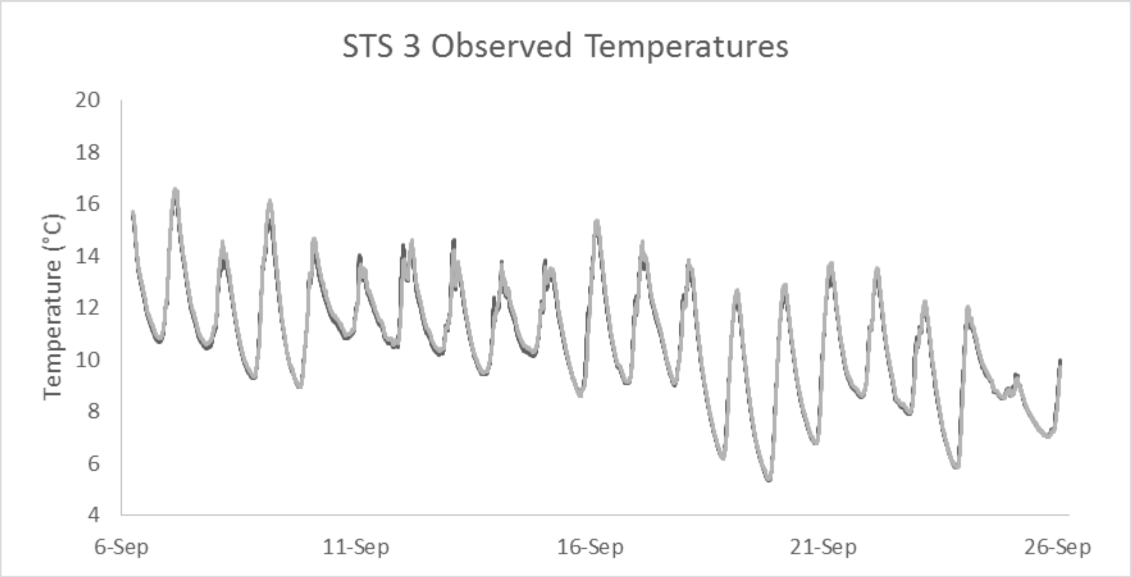

Figure E.5: Continuous water temperature data used for STS 3 segmentation collected in the beaver pond calibration September 6, 2013 18:00 – September 26, 2013 13:55 MST at 5-minute increments using two HOBO Pro v2 temperature sensors (Onset Computer Corporation, Cape Cod, MA)

APPENDIX F

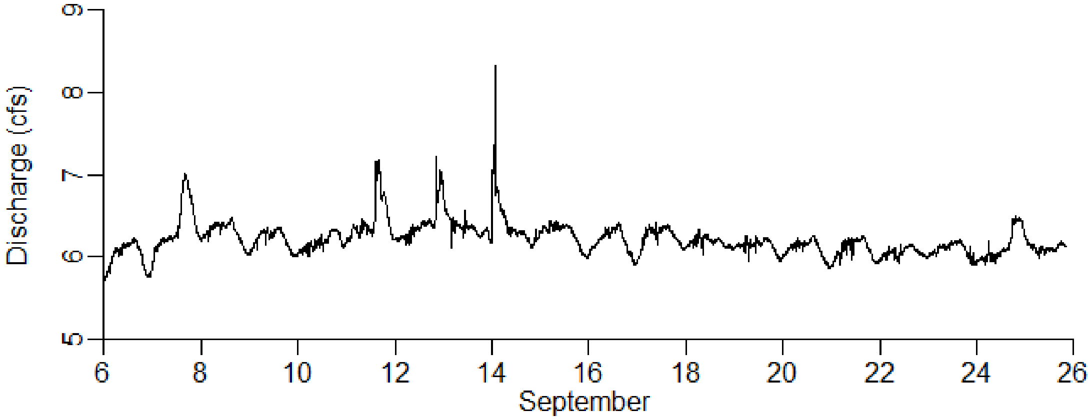

Figure F.1: Continuous discharge data used in the calibration calculated using a stage-discharge relationship based on continuous stage data collected upstream of the beaver pond September 6, 2013 18:00 – September 26, 2013 13:55 MST at 5-minute increments using SPXD 600 and 610 pressure transducers (KWK Technologies, Spokane, Washington) with vented cables

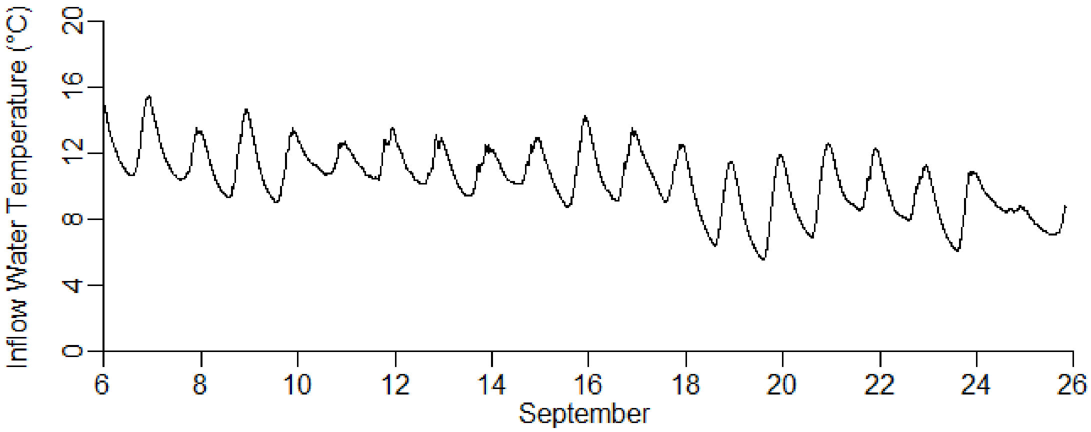

Figure F.2: Continuous water temperature data used in the calibration collected upstream of the beaver pond September 6, 2013 18:00 – September 26, 2013 13:55 MST at 5-minute increments using HOBO Pro v2 temperature sensors (Onset Computer Corporation, Cape Cod, MA) used to provide an upper boundary condition

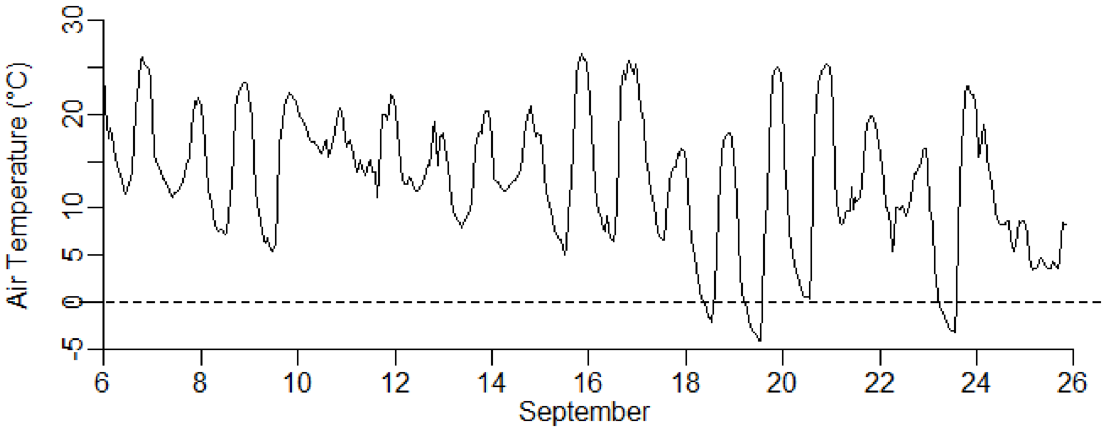

Figure F.3: Continuous air temperature data used in the calibration collected September 6, 2013 18:00 – September 26, 2013 14:00 MST at one-hour increments from an onsite weather station

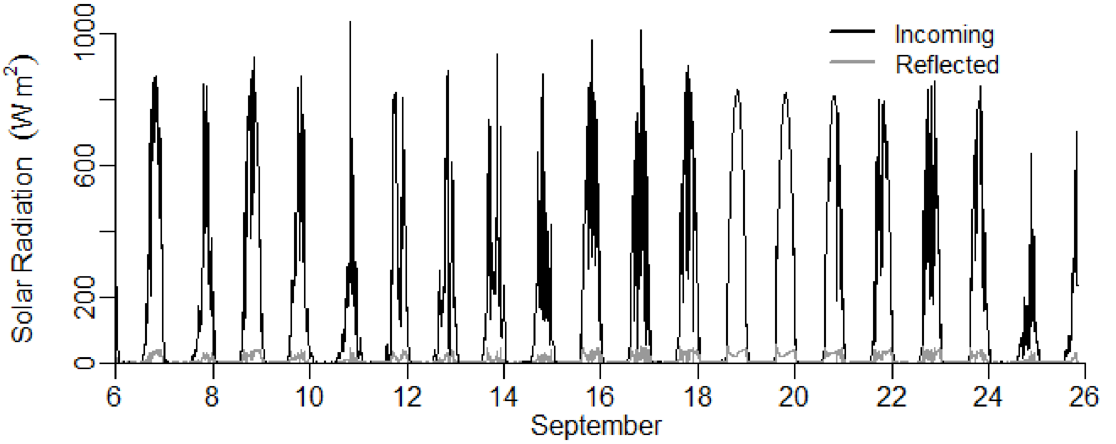

Figure F.4: Incoming and reflected solar radiation data used in the calibration collected for September 6, 2013 18:00 – September 26, 2013 13:55 MST at five-minute increments using two LP02 pyranometers (Hukseflux Thermal Sensors, Delft, Netherlands) used to determine net shortwave radiation

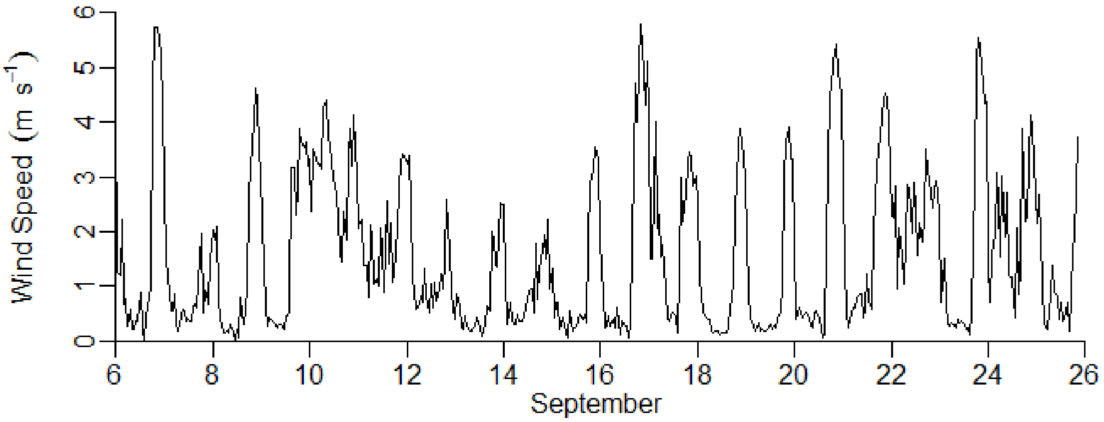

Figure F.5: Continuous wind speed data used in the calibration collected September 6, 2013 18:00 – September 26, 2013 14:00 MST at one-hour increments from an onsite weather station

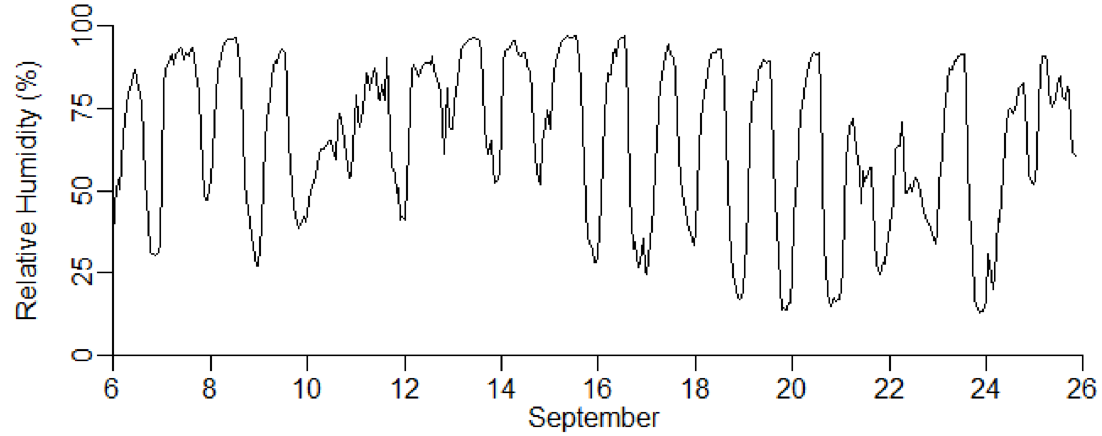

Figure F.6: Continuous relative humidity data used in the calibration collected September 6, 2013 18:00 – September 26, 2013 14:00 MST at one-hour increments from an onsite weather station

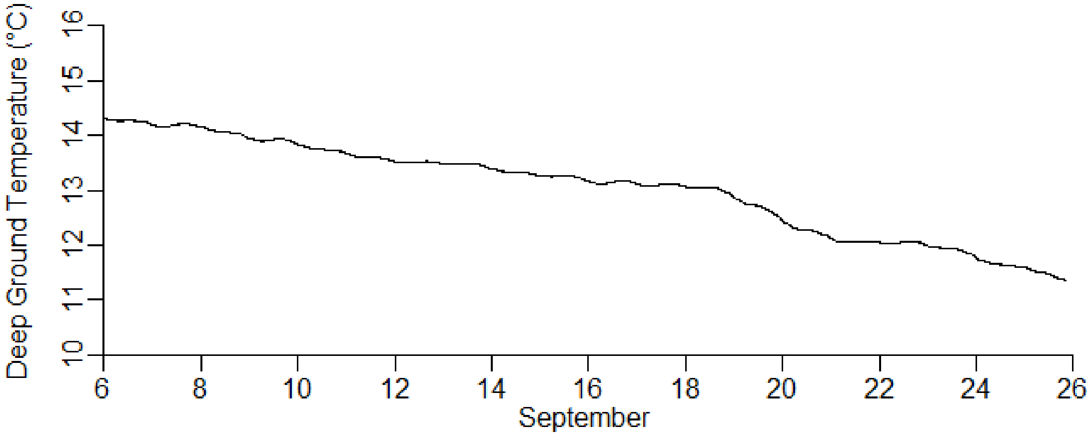

Figure F.7: Continuous sediment temperature data used in the calibration 75 centimeters below the sediment-water interface collected September 6, 2013 18:00 – September 26, 2013 13:55 MST at 5-minute increments using HOBO Pro v2 temperature sensors (Onset Computer Corporation, Cape Cod, MA)

Table F.1: Calibration water surface area, water volume, mixing lengths, and average water depth for each zone determined from survey data collected using differential rtkGPS (Trimble® R8, Global Navigation Satellite System, Dayton, Ohio) and ArcGIS 10.1

	Main Channel	STS Zone 1 Layer 1	STS Zone 1 Layer 2	STS Zone 2	STS Zone 3
Surface Area (m^2)	135.09	12.21	48.08	3.20	2.90
Volume (m^3)	292.79	124.44	124.44	19.09	20.70
Mixing Length (cm)	944.07	2318.32	2318.32	341.99	231.01
Average Water Depth (cm)	46.14	10.25	38.20	16.76	13.99

Table F.2: Calibration interfacial area between each zone estimated from the bathymetry data shown in Table F.1

	Interfacial Area (cm^2)
Main Channel and STS Zone 1 Layer 1	14111.33
Main Channel and STS Zone 1 Layer 2	52590.39
Main Channel and STS Zone 2	22844.38
Main Channel and STS Zone 3	26959.06

APPENDIX G

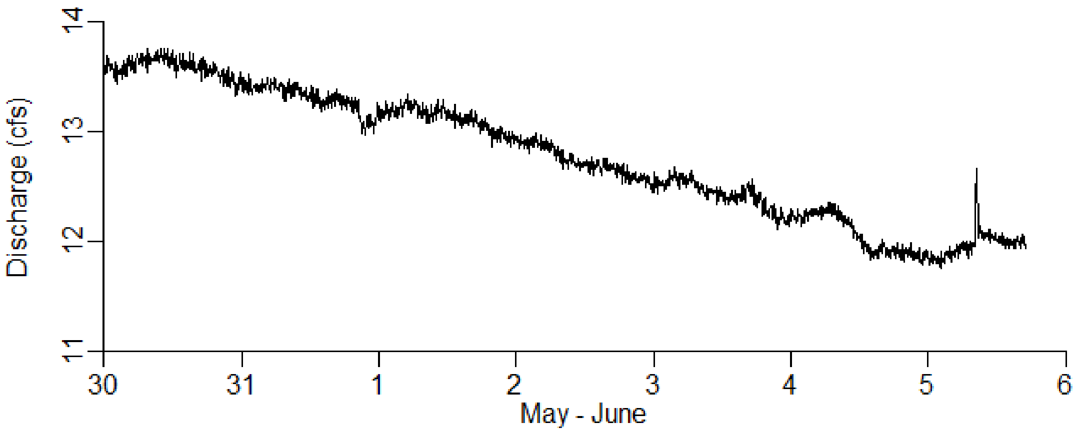

Figure G.1: Continuous discharge data used in the corroboration calculated using a stage-discharge relationship based on continuous stage data collected upstream of the beaver pond May 30, 22:00 – June 6, 2012 15:00 UTC at 5-minute increments using SPXD 600 and 610 pressure transducers (KWK Technologies, Spokane, Washington) with vented cables

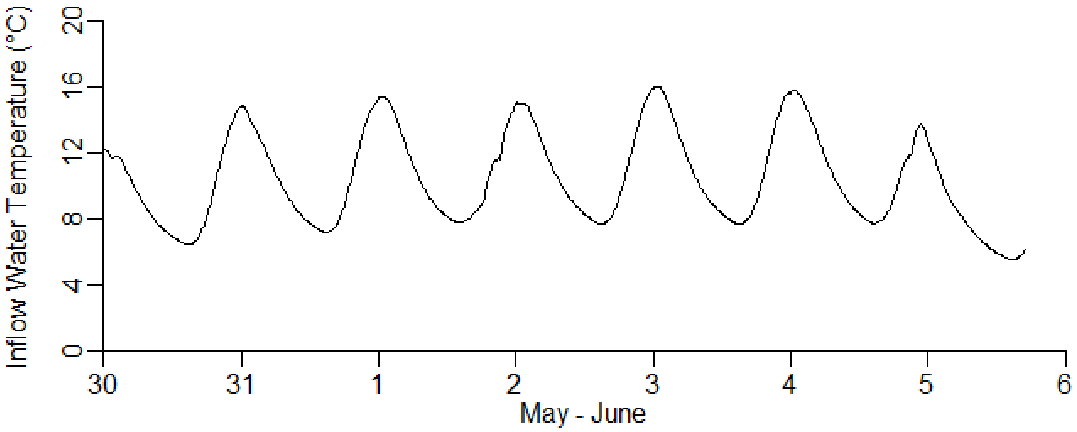

Figure G.2: Continuous water temperature used in the corroboration data collected upstream of the beaver pond May 30, 22:00 – June 6, 2012 15:00 UTC at 10-minute increments using HOBO Pro v2 temperature sensors (Onset Computer Corporation, Cape Cod, MA) used to provide an upper boundary condition

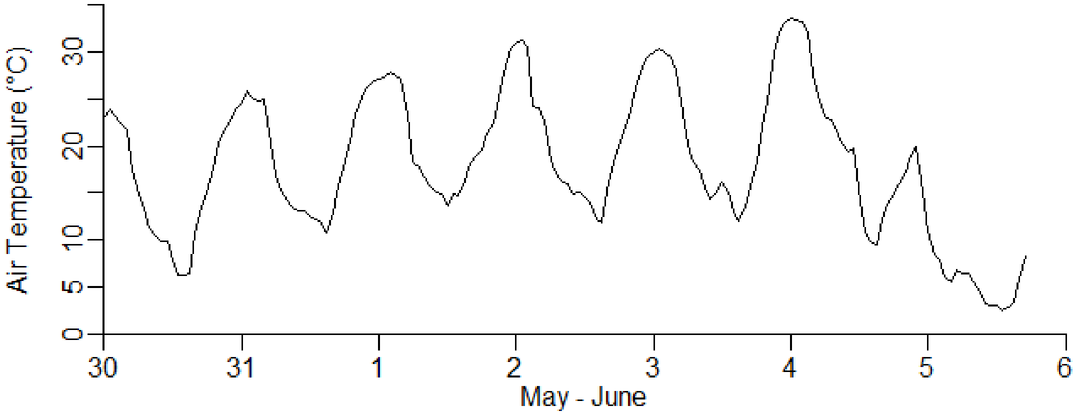

Figure G.3: Continuous air temperature data used in the corroboration collected May 30, 22:00 – June 6, 2012 15:00 UTC at one-hour increments taken from the Little Bear River WATERS Test Bed Utah State University Experimental Farm weather station near Wellsville, UT (approximately 22 miles from Curtis Creek) [*Utah Water Research Laboratory*, unpublished data, 2009]

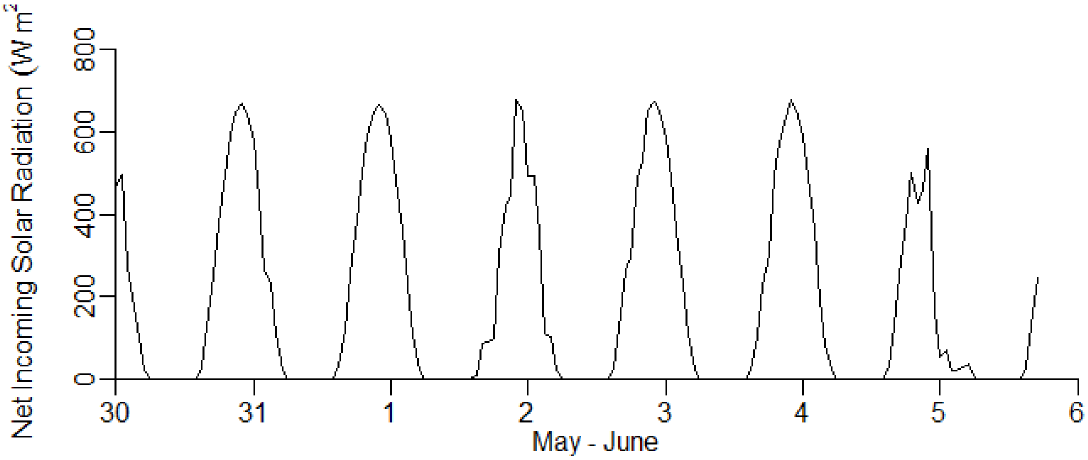

Figure G.4: Continuous solar radiation data used in the corroboration collected May 30, 22:00 – June 6, 2012 15:00 UTC at one-hour increments taken from the Little Bear River WATERS Test Bed Utah State University Experimental Farm weather station near Wellsville, UT (approximately 22 miles from Curtis Creek) [*Utah Water Research Laboratory*, unpublished data, 2009]

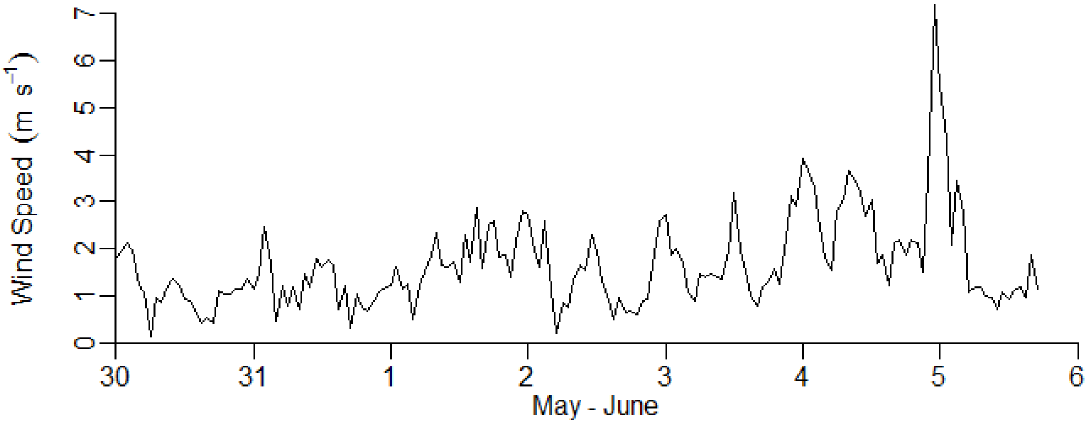

Figure G.5: Continuous wind speed data used in the corroboration collected May 30, 22:00 – June 6, 2012 15:00 UTC at one-hour increments taken from the Little Bear River WATERS Test Bed Utah State University Experimental Farm weather station near Wellsville, UT (approximately 22 miles from Curtis Creek) [*Utah Water Research Laboratory*, unpublished data, 2009]

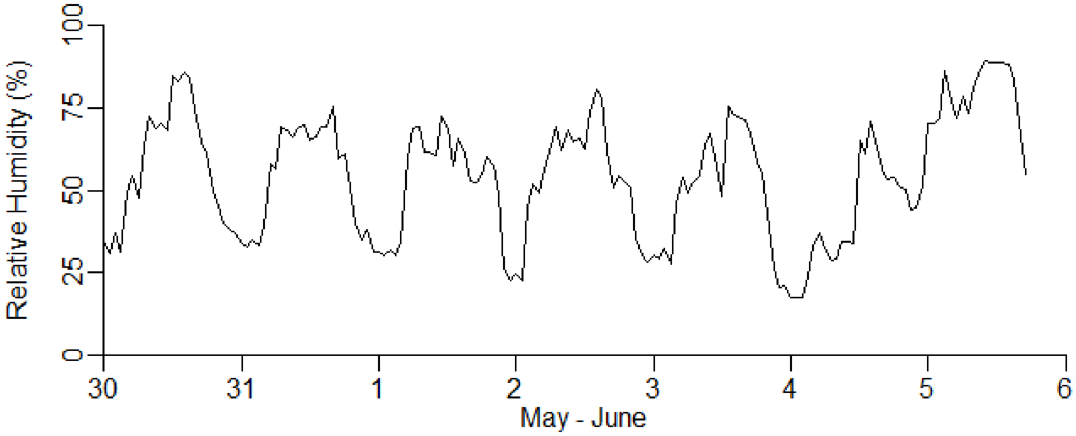

Figure G.6: Continuous relative humidity data used in the corroboration collected May 30, 22:00 – June 6, 2012 15:00 UTC at one-hour increments taken from the Little Bear River WATERS Test Bed Utah State University Experimental Farm weather station near Wellsville, UT (approximately 22 miles from Curtis Creek) [*Utah Water Research Laboratory*, unpublished data, 2009]

Table G.1: Corroboration water surface area, water volume, mixing lengths, and average water depth for each zone determined from survey data collected using differential rtkGPS (Trimble® R8, Global Navigation Satellite System, Dayton, Ohio) and ArcGIS 10.1

	Main Channel	STS Zone 1 Layer 1	STS Zone 1 Layer 2	STS Zone 2	STS Zone 3
Surface Area (m^2)	107.06	23.69	33.58	3.00	29.61
Volume (m^3)	208.20	118.46	118.46	16.98	65.00
Mixing Length (cm)	1268.97	2606.51	2606.51	209.56	778.57
Average Water Depth (cm)	50.02	20.00	28.34	17.64	45.55

Table G.2: Corroboration interfacial area between each zone estimated from the bathymetry data shown in Table G.1

	Interfacial Area (cm^2)
Main Channel and STS Zone 1 Layer 1	22375.29
Main Channel and STS Zone 1 Layer 2	31709.97
Main Channel and STS Zone 2	32720.19
Main Channel and STS Zone 3	30155.71

APPENDIX H

A comparison of the meteorological data collected at the weather stations located on Curtis Creek and at the Little Bear River WATERS Test Bed Utah State University Experimental Farm weather station near Wellsville, UT (approximately 22 miles from Curtis Creek) [*Utah Water Research Laboratory*, unpublished data, 2009] September 6, 2013 18:00 to September 26, 2013 15:00 MST.

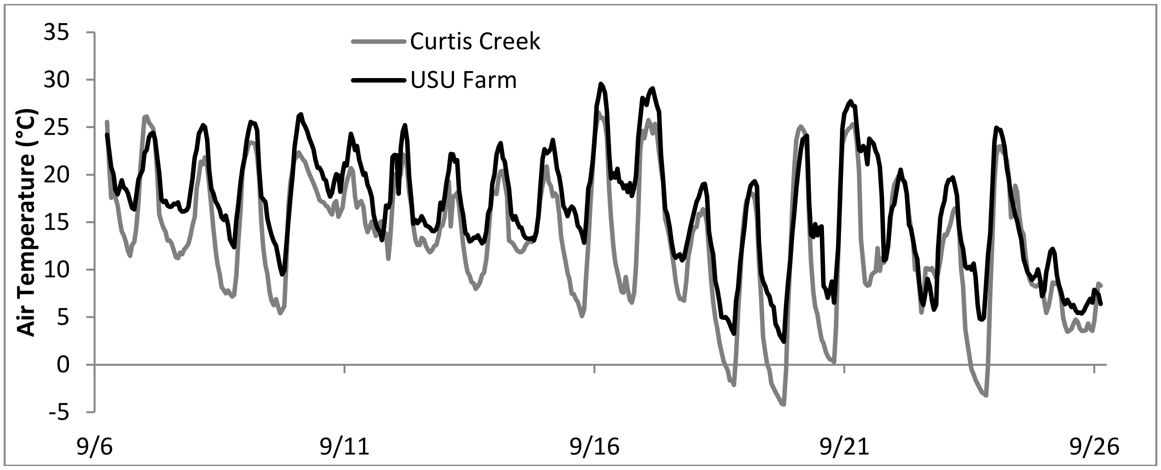

Figure H.1: Continuous air temperature data for both the Curtis Creek weather station and the Little Bear River WATERS Test Bed Utah State University Experimental Farm weather station near Wellsville, UT (approximately 22 miles from Curtis Creek) [*Utah Water Research Laboratory*, unpublished data, 2009] collected September 6, 18:00 – September 26, 2013 15:00 MST at one-hour increments

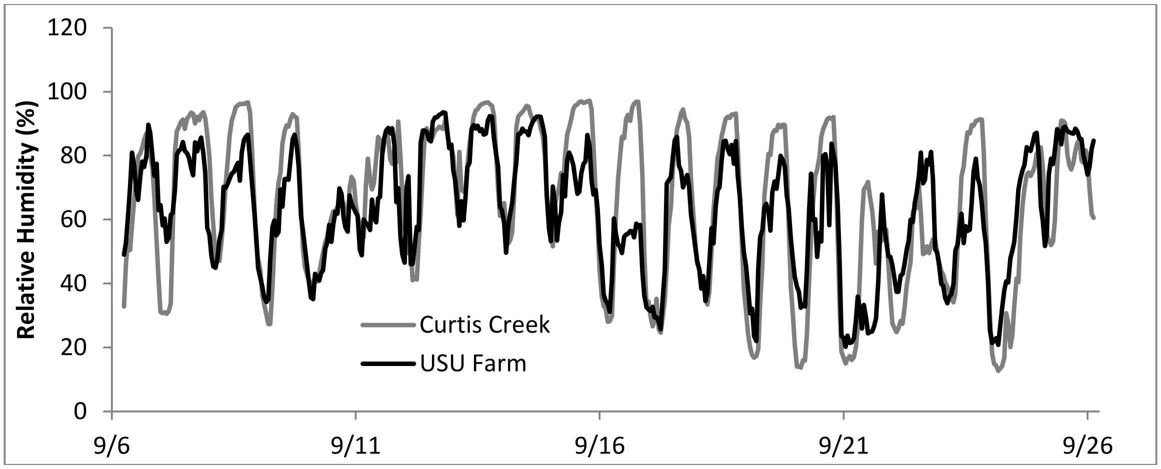

Figure H.2: Continuous relative humidity data for both the Curtis Creek weather station and the Little Bear River WATERS Test Bed Utah State University Experimental Farm weather station near Wellsville, UT (approximately 22 miles from Curtis Creek) [*Utah Water Research Laboratory*, unpublished data, 2009] collected September 6, 18:00 – September 26, 2013 15:00 MST at one-hour increments

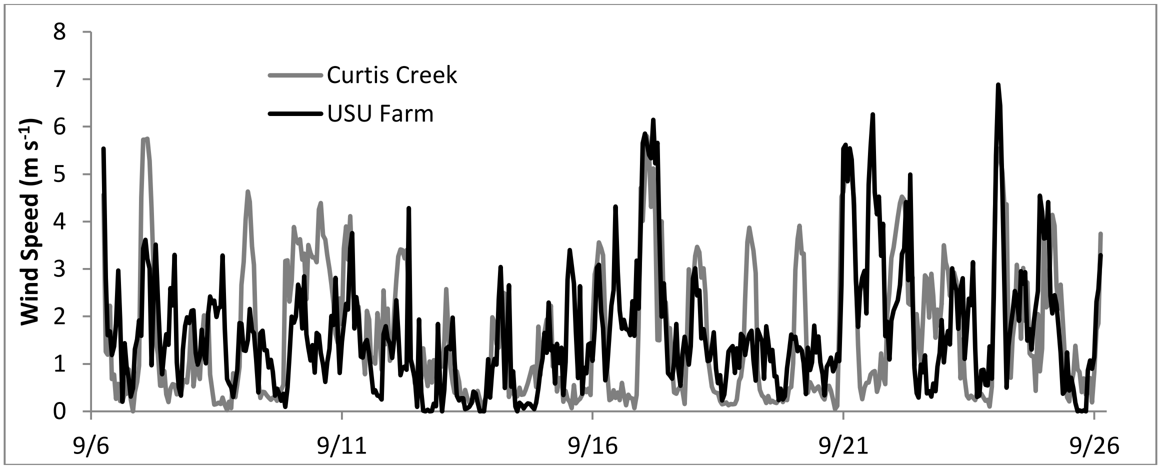

Figure H.3: Continuous wind speed data for both the Curtis Creek weather station and the Little Bear River WATERS Test Bed Utah State University Experimental Farm weather station near Wellsville, UT (approximately 22 miles from Curtis Creek) [*Utah Water Research Laboratory*, unpublished data, 2009] collected September 6, 18:00 – September 26, 2013 15:00 MST at one-hour increments

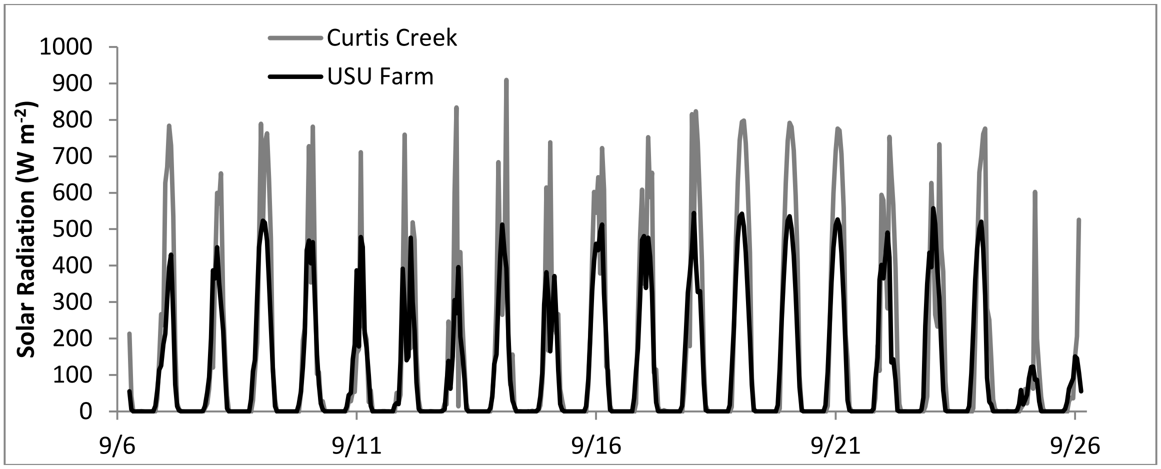

Figure H.4: Continuous solar radiation data for both the Curtis Creek weather station and the Little Bear River WATERS Test Bed Utah State University Experimental Farm weather station near Wellsville, UT (approximately 22 miles from Curtis Creek) [*Utah Water Research Laboratory*, unpublished data, 2009] collected September 6, 18:00 – September 26, 2013 15:00 MST at one-hour increments

APPENDIX I

Example calculation for obtaining an immersion coefficient:
To obtain immersion coefficients for the pyranometer (Model LP02; Hukseflux Thermal Sensors, Delft, Netherlands), Equation 16 was used and the process is demonstrated in the following steps.

$$I_f = \frac{J_{sn}(0^+)}{J_{sn}(0^-)} t_{wa} \qquad \text{Equation 16}$$

Data collected for experiment used to determine the immersion coefficient of the pyranometer under the tungsten-halogen lamp are shown in the following table. The sensor readings represent $J_{sn}(0^-)$ in Equation 16.

Depth of water to Detector (cm)	**Sensor Reading (W m^{-2})**
Measurement in Air	88.14
0.2	27.96
5.5	6.89
10.5	2.98
15.5	0.75

The first step is to estimate the actual amount of shortwave radiation reaching each water depth by determining an attenuation coefficient from the data using Equation 9:

$$J_{sn}(z) = J_{sn} e^{-\lambda z} \qquad \text{Equation 11}$$

This equation can be linearized as follows:

$$\ln[J_{sn}(z)] = -\lambda z + \ln[J_{sn}]$$

The natural log of the shortwave radiation measurements taken at depth *z*, $\ln[J_{sn}(z)]$, is plotted against depth, *z*, as follows:

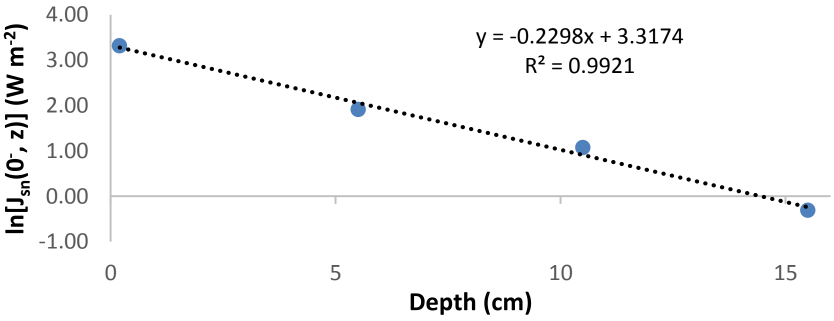

Using the linear regression as it compared to the linearized form of Equation 9, the attenuation coefficient was determined to be λ = 0.23 cm^{-1}

The actual amount of shortwave radiation reaching each depth was estimated using Equation 9 and the attenuation coefficient as follows:

$$J_{sn}(z) = 88.14 \frac{W}{m^{-2}} * e^{(-0.23\ cm^{-1} * z)}$$

This was applied to produce the results for $J_{sn}(0^+)$ as shown in the following table:

Depth of water to Detector (cm)	**Shortwave Radiation Reaching Depth (W m^{-2})**
0.2	84.18
5.5	24.91
10.5	7.90
15.5	2.50

Applying each of the values of $J_{sn}(0^-)$ and $J_{sn}(0^+)$, and applying a Fresnel reflectance t_{wa} = 2% to Equation 16, the immersion coefficient can be obtained as follows:

$$I_f = \frac{84.18 \frac{W}{m^{-2}}}{27.96 \frac{W}{m^{-2}}} (2\%) = 3.01$$

A table of the immersion coefficients determined for each depth is shown in the following table:

Depth of water to Sensor (cm)	**Immersion Coefficient**
0.2	3.01
5.5	3.62
10.5	2.65
15.5	3.34
Average	3.15
Standard Deviation	0.42

Therefore the immersion coefficient for the tungsten-halogen lamp was determined to be 3.15 ± 0.42 W m^{-2}.

Example calculation for obtaining a cosine response:

To determine the cosine response of the pyranometer (Model LP02; Hukseflux Thermal Sensors, Delft, Netherlands) Equation 17 was used:

Equation 17

$$\frac{J_{sn}(\theta)}{J_{sn}(0°)} = \cos(\theta)$$

As an example when the sensor detector is angled at 45° from 0° incident (see Figure 29):

$$J_{sn}(45°) = 6.39\frac{W}{m^{-2}}$$
$$J_{sn}(0°) = 27.96\frac{W}{m^{-2}}$$

Therefore:

$$\frac{J_{sn}(45°)}{J_{sn}(0°)} = \frac{6.39\frac{W}{m^{-2}}}{27.96\frac{W}{m^{-2}}} = 0.229$$

Applying this value back into Equation 17 we can see that the cosine response of the sensor is not the same as expected from the theoretical cosine response of

$$\cos(45°) = 0.707$$

$$0.229 \neq 0.707$$

And the fraction of the expected response as shown in Figure 32(a) is:

$$\frac{0.229}{0.707} * 100\% = 32.3\%$$

And the percent difference between these measurements as shown in Figure 32(b) is:

$$(0.229 - 0.707) * 100\% = 47.9\%$$